

Scuola di Scienze

Dipartimento di Fisica e Astronomia

Corso di Laurea Magistrale in Astrofisica e Cosmologia

# **Global instability of stellar discs in presence of dark matter halos**

Tesi di laurea

Presentata da:

**Sebastiano Cantarella**

Relatore:

**Prof. Carlo Nipoti**

Correlatori:

**Prof. Luca Ciotti**

**Prof.ssa Silvia Pellegrini**

**Dott. Pasquale Londrillo**



## Abstract

Since the 1970s, numerical studies have shown that highly flattened rotationally supported galactic discs are globally unstable: in particular, they are subject to large-scale bar-like instabilities. Ostriker and Peebles (1973) proposed a global stability criterion through the ratio  $t_{OP} = T/|W|$  between the total kinetic energy of rotation of the system  $T$  and its total gravitational energy  $W$ . However, even though  $t_{OP}$  is widely used as a global stability parameter, its applicability has been questioned from both theoretical and numerical perspectives. Efstathiou, Lake and Negroponte (1982) presented an alternative criterion based on the parameter  $t^* = T_d/[(1 + f_{ext})^2|W_D|]$ , where  $T_d$  represents the stellar kinetic energy of rotation,  $W_D$  is the contribution to the trace of the Chandrasekar potential-energy tensor  $\mathbf{W}$  related to the stars in the total disc-halo potential and  $f_{ext} = W_{dh}/W_d$  is the ratio of the gravitational energy of the stars due to the halo potential and the self-energy of the stellar disc.  $t^*$  differs from  $t_{OP}$  in two main aspects: with respect to  $W$ ,  $W_D$  depends only on the force the whole system exerts on the stellar disc; while in  $T_d$  the mean circular velocity is computed on cylinders centred at the origin of the disc, in  $T$  the streaming velocity is calculated on rings that are concentric at the same disc centre. Because of its construction,  $T_d$  is more sensitive than  $T$  to bar-like modes, since they are weakly dependent on the thickness of the disc. Both  $t_{OP}$  and  $t^*$  have been proposed as global stability indicators in case of a galactic disc inside a rigid dark matter halo.

In this master thesis we have studied the behaviour of  $t_{OP}$  and  $t^*$  and their relationship with global instability through  $N$ -body simulations with the Fortran Version of a Fast Poisson Solver (FVFPS, Londrillo et al., 2003) code. Together with  $t_{OP}$  and  $t^*$ , we also present and study a new global stability parameter  $t_W = T_d/|W_D|$  which is closely connected to the virial theorem of a disc embedded in a halo.

At the beginning of the simulations, the disc particles move around circular orbits centred at the origin of the system. After generating the stellar disc, we place it within a rigid and non-rotating dark matter halo, modelled by a Hernquist (1990) profile. Moreover, the fraction of retrograde circular orbits is regulated by a parameter  $\alpha$  and implements a tangential velocity dispersion in the circular orbits, which gives a little support to the stability of the system.

In the subsequent part of the thesis, we perform  $N$ -body simulations using the FVFPS code for the initial disc-halo systems, varying the input parameters connected to the system configuration. In a diagnostic phase, the results of the numerical simulations are analysed, including the density and velocity profiles, the angular momentum evolution of the disc and the disc's anisotropy (e.g., presence of  $m = 2$  modes).

Consistent with previous literature, discs within dominant external halos exhibit stationary scenarios, while disc-only simulations show local (e.g. Jeans, 1902; Toomre, 1964) instabilities and the loss of axisymmetry of the system. The multiple configurations of the disc and halo features have provided a better understanding of  $t_{OP}$ ,  $t^*$  and  $t_W$  as global stability parameters for the bar formation in disc-halo systems.

The main results of this work are the following: i) we have found unstable systems even though  $T_d = 0$  (i.e.  $t_{OP} = t^* = 0$ ), which are thus counterexamples of Ostriker and Peebles's and Efstathiou, Lake and Negroponte's criteria; ii) the  $t_W$  parameter has some problems too: in all the simulations it is not sensitive to the presence of the halo.



## Sommario

Sin dagli anni '70 gli studi numerici hanno mostrato che i dischi galattici sottili sostenuti dalla rotazione sono globalmente instabili: in particolare, essi sono soggetti a instabilità su grande scala di tipo barra. Ostriker e Peebles (1973) proposero un criterio di stabilità globale basato sul rapporto  $t_{OP} = T/|W|$  tra l'energia cinetica totale di rotazione del sistema  $T$  e la sua energia potenziale gravitazionale totale  $W$ . Benché  $t_{OP}$  sia vastamente usato come parametro di stabilità globale, la sua appropriatezza è stata messa in discussione sia dal punto di vista teorico che da quello numerico. Efstathiou, Lake e Negroponte (1982) presentarono un criterio alternativo basato sul parametro  $t^* = T_d/[(1 + f_{ext})^2|W_D|]$ , dove  $T_d$  è l'energia cinetica di rotazione relativa alle stelle,  $W_D$  è il contributo alla traccia del tensore energia-potenziale  $\mathbf{W}$  relativo alle stelle nel potenziale del sistema disco-alone e  $f_{ext} = W_{dh}/W_d$  è il rapporto tra l'energia gravitazionale delle stelle dovuta al potenziale dell'alone e l'energia gravitazionale propria del disco stellare.  $t^*$  si distingue da  $t_{OP}$  su due aspetti principali: rispetto a  $W$ ,  $W_D$  dipende solo dalla forza che l'intero sistema esercita sul disco stellare; mentre in  $T_d$  la velocità circolare media è calcolata su cilindri avente come centro l'origine del disco, in  $T$  la velocità di flusso è determinata su anelli con centro l'origine del disco. Per come è costruito,  $T_d$  è più sensibile di  $T$  ai modi di tipo barra, i quali dipendono debolmente dallo spessore del disco. Sia  $t_{OP}$  che  $t^*$  sono stati proposti come indicatori di stabilità globale in caso di un disco dentro un alone rigido di materia oscura.

In questa tesi magistrale abbiamo studiato il comportamento di  $t_{OP}$  e  $t^*$ , e il loro legame con l'instabilità globale, mediante simulazioni  $N$ -body con il codice Fortran Version of a Fast Poisson Solver (FVFPS, Londrillo et al., 2003). Oltre a  $t_{OP}$  e a  $t^*$ , presentiamo e studiamo anche un nuovo parametro di stabilità globale  $t_W = T_d/|W_D|$ , che è strettamente collegato al teorema del viriale di un disco all'interno di un alone.

All'inizio delle simulazioni le particelle del disco si muovono lungo orbite circolari centrate all'origine del sistema. Dopo aver generato il disco stellare, lo posizioniamo dentro un alone di materia oscura rigido e non rotante, che modelliamo con un profilo di Hernquist (1990). Inoltre, la frazione di orbite circolari retrograde è regolata da un parametro  $\alpha$ , che genera una dispersione di velocità tangenziale nelle orbite circolari, contribuendo lievemente alla stabilità del sistema.

Nella successiva parte della tesi abbiamo svolto delle simulazioni  $N$ -body mediante il codice FVFPS a partire dal sistema disco-alone generato, modificando i parametri di input relativi alla configurazione del sistema. Nella fase diagnostica, i risultati delle simulazioni numeriche sono stati analizzati mediante profili di densità e di velocità, insieme a profili di evoluzione del momento angolare del disco e le sue anisotropie (es., presenza di modi  $m = 2$ ).

In coerenza con la letteratura, i dischi dentro un alone dominante sono stabili e stazionari, mentre simulazioni con solo i dischi mostrano instabilità locali (e.g. Jeans, 1902; Toomre, 1964) e una perdita di simmetria assiale del sistema. Le molteplici configurazioni della coppia disco-alone hanno fornito maggiori informazioni su  $t_{OP}$  e  $t^*$  come indicatori di stabilità globale riguardo alla formazione di barre nel disco.

I risultati principali di questo lavoro sono i seguenti: i) abbiamo trovato sistemi instabili in simulazioni in cui  $T_d = 0$  (ossia  $t_{OP} = t^* = 0$ ), fornendo dei controesempi ai criteri riportati da Ostriker e Peebles e Efstathiou, Lake e Negroponte; ii) anche  $t_W$  presenta dei problemi: in tutte le simulazioni non è sensibile alla presenza dell'alone.



# Contents

<b>Introduction</b>	<b>5</b>
<b>1 Potential theory and the virial theorem</b>	<b>7</b>
1.1 Potential theory . . . . .	8
1.1.1 Potential theory of spherical systems . . . . .	9
1.1.2 Potential theory of galactic discs . . . . .	10
1.2 The virial theorem . . . . .	11
1.2.1 Tensor virial theorem . . . . .	11
1.2.2 Scalar virial theorem . . . . .	12
1.2.3 Scalar virial theorem for a two-component system . . . . .	12
1.2.4 Scalar virial theorem for a self-gravitating system embedded in an external gravitational potential field . . . . .	13
1.2.5 Gravitational self-energy and gravitational interaction energy . .	14
<b>2 Global stability parameters for stellar discs</b>	<b>15</b>
2.1 Ostriker-Peebles's stability criterion . . . . .	16
2.1.1 Construction of OP's global stability parameter . . . . .	16
2.1.2 General considerations on $t_{OP}$ . . . . .	17
2.1.3 Numerical simulations . . . . .	18
2.1.4 Results . . . . .	18
2.1.5 Conclusions . . . . .	19
2.2 Efstathiou, Lake and Negroponte's $t^*$ parameter . . . . .	19
2.2.1 Construction of ELN's global stability parameter . . . . .	19
2.2.2 Numerical simulations . . . . .	21
2.2.3 Results . . . . .	21
2.2.4 Conclusions . . . . .	22
2.3 Comparison between $t_{OP}$ and $t^*$ . . . . .	22
2.4 Universal validity of the $t_{OP}$ and $t^*$ parameters: a still open discussion .	24
2.5 A new experimental global stability parameter . . . . .	25
<b>3 Set up of the <math>N</math>-body simulations</b>	<b>26</b>
3.1 Galaxy models . . . . .	27
3.1.1 The Hernquist profile . . . . .	27
3.1.2 The exponential disc . . . . .	29
3.2 Initial conditions . . . . .	30
3.2.1 Input parameters . . . . .	30
3.2.2 Disc: position and velocity assignment . . . . .	30
3.3 Testing the initial conditions . . . . .	32
3.4 Set up of the $N$ -body simulations . . . . .	35

3.4.1	Set up parameters . . . . .	35
<b>4</b>	<b>Results</b>	<b>39</b>
4.1	Simulation diagnostics . . . . .	40
4.1.1	Density maps . . . . .	40
4.1.2	Surface density profiles . . . . .	41
4.1.3	Kinetic energy . . . . .	41
4.1.4	Angular momentum . . . . .	42
4.1.5	Half-mass radius $R_h$ of the disc . . . . .	43
4.1.6	$m = 2$ modes of the disc . . . . .	43
4.1.7	$t_{OP}$ , $t^*$ and $t_W$ computation . . . . .	43
4.2	Initial parameters of the $N$ -body simulations . . . . .	44
4.3	Simulations without dark halo . . . . .	46
4.3.1	Simulation $M_h 0 a_h 0 \alpha 0$ ( $M_h = 0, \alpha = 0$ ) . . . . .	46
4.3.2	Simulation $M_h 0 a_h 0 \alpha 0.5$ ( $M_h = 0, \alpha = 0.5$ ) . . . . .	51
4.4	Simulations with dark halo . . . . .	55
4.4.1	Simulation $M_h 4 a_h 5 \alpha 0$ ( $M_h/M_d = 4, a_h/R_d = 5, \alpha = 0$ ) . . . . .	55
4.4.2	Simulation $M_h 4 a_h 5 \alpha 0.5$ ( $M_h/M_d = 4, a_h/R_d = 5, \alpha = 0.5$ ) . . . . .	60
4.4.3	Simulation $M_h 10 a_h 5 \alpha 0$ ( $M_h/M_d = 10, a_h/R_d = 5, \alpha = 0$ ) . . . . .	65
4.4.4	Simulation $M_h 400 a_h 5 \alpha 0$ ( $M_h/M_d = 400, a_h/R_d = 5, \alpha = 0$ ) . . . . .	70
4.5	Results on $t_{OP}$ , $t^*$ and $t_W$ . . . . .	73
<b>5</b>	<b>Conclusions and future perspectives</b>	<b>79</b>
<b>A</b>	<b>Mixed terms <math>W_{12}</math> and <math>W_{21}</math> in a two-component system</b>	<b>82</b>
<b>B</b>	<b>Details about OP73 and ELN82</b>	<b>83</b>
B.1	OP73 . . . . .	83
B.1.1	Acceleration computation . . . . .	83
B.1.2	Initial conditions . . . . .	83
B.1.3	Energies computation . . . . .	84
B.2	ELN82 . . . . .	84
B.2.1	Numerical computation . . . . .	84
B.2.2	Galaxy models . . . . .	84
B.2.3	$m = 2$ modes, bar strength $\delta_2$ and bar length $l_b$ . . . . .	85
B.2.4	Results from other models . . . . .	86
B.2.5	Comparison with observations . . . . .	86
<b>C</b>	<b>Equations of motion in polar coordinates</b>	<b>87</b>
C.1	General motion . . . . .	87
C.2	Pure circular motion ( $v_R = 0, v_\varphi \neq 0$ ) . . . . .	88
<b>D</b>	<b><math>T</math> and <math>\Pi</math> computation in presence of retrograde orbits</b>	<b>89</b>

# Introduction

In this thesis we study the astrophysical problem of the global stability of stellar discs in presence of dark matter halos. Unstable discs can form a bar, so the question of global disc instability is relevant to observed systems, since in the local universe at least 60% of disc galaxies are strongly barred (Eskridge et al., 2000; Grosbøl et al., 2004; Menéndez-Delmestre et al., 2007; Barazza et al., 2008; Saha and Elmegreen, 2018). Since the 1960s, both theoretical (e.g., Lebovitz, 1961; Bodenheimer and Ostriker, 1973) and numerical (e.g., Hohl, 1971) studies have shown a bar pattern inside a disc is easy to form, thus spiral galaxies are easily subject to a global instability which involves the formations of a stellar bar at the centre of the system. Besides, once a bar is formed within the disc, it is hard to dissolve (Athanasoula et al., 2005). For this reason, there is an active branch of astrophysics involved in the research of both theoretical and observational properties of the disc that can be collected to build a criterion which can tell us whether a disc is globally stable or not from its configuration (e.g., Sellwood, 2016; Saha and Elmegreen, 2018; Kataria et al., 2020; Romeo et al., 2023).

The pursuit of a global stability criterion is the main topic of Ostriker and Peebles’s (1973) work, where the authors proposed, starting from the virial theorem of the whole disc-halo system, a parameter  $t_{OP} = T/|W|$ , where  $T$  is the ordered kinetic energy associated to the system and  $W$  is the total gravitational potential. However, some physical cons of  $t_{OP}$  were argued by Efstathiou, Lake and Negroponte (1982): due to its nature,  $t_{OP}$  shows stability in unstable scenarios, such as systems where the halo has small mass but is very concentrated at the centre of the disc, or it is massive but diluted, thus not contributing to the global stability of the disc. For this reason, Efstathiou, Lake and Negroponte (1982) presented a new global stability parameter  $t^* = T_d/|W_D|$ , which is now defined starting from the virial theorem of the disc component, assumed to be embedded in an external potential (Section 2.2). Here  $t^*$  is the ratio between the stellar ordered kinetic energy  $T_d$  and the gravitational potential energy of the disc due to the whole disc-halo potential. Even though this parameter has been reformulated in subsequent works (see Christodoulou et al., 1995; Mo et al., 1998; Parente et al., 2023), the universal validity of this parameter has been debated through both theoretical (Athanasoula, 2008) and observational points of view (see, e.g., Izquierdo-Villalba et al., 2022; Romeo et al., 2023; Bland-Hawthorn et al., 2023).

The main goal of this thesis is studying through  $N$ -body simulations the behaviour of the two well-known global stability parameters  $t_{OP}$  and  $t^*$  from Ostriker and Peebles (1973) and Efstathiou, Lake and Negroponte (1982), respectively, in some toy-models of disc-halo systems, where the particles of a razor-thin disc move around circular orbits and the halo is modelled as a fixed external potential.

To do so, in Chapter 1 we first review the theoretical background of the potential theory – in particular the meaning of the gravitational potential energy  $W$  – and the wide topic of the virial theorem for a system made up of one or more components.

Then, after this theoretical remark, Chapter 2 focuses on the work done by Ostriker and Peebles (1973) and Efstathiou, Lake and Negroponte (1982) and their corresponding  $t_{OP}$  and  $t^*$  parameters, analysing their theoretical construction and their main results with different disc-halo system, also talking about their positive and negative aspects. In particular, the latter suggested us a new global stability parameter, which we label with  $t_W$  (Section 2.5). These three parameters are analysed through several  $N$ -body simulations performed by the Fortran-90 code FVFPS (see Londrillo et al., 2003). Chapter 3 describes the theoretical and numerical construction of the initial conditions for our simulation suite, which are made of a razor-thin disc model and a spherically symmetric halo, where the latter is rigid and non-rotating, thus treatable as a fixed potential. For all simulations, we initially set every particle in pure circular orbits. This particular configuration gives no radial velocity dispersion to the particles, while an azimuthal velocity dispersion can be achieved by inverting the sense of rotation for a fraction of disc particles – the so-called retrograde orbits (see, e.g., Kalnajs, 1977). Chapter 4 presents a summary of our simulation suite, reporting some significant  $N$ -body runs and discussing the behaviour of  $t_{OP}$ ,  $t^*$  and  $t_W$  in different disc-halo configurations. Here we study the importance of the theoretical construction of these global stability parameters. Chapter 5 is a summary of all the work done in this thesis, also discussing future perspectives about the investigation and the pursuit of a universally accepted (if there is any) global stability parameter.

# Chapter 1

## Potential theory and the virial theorem

To build a global stability parameter for stellar discs, Ostriker and Peebles (1973) started from the virial theorem for the disc-halo system. Using the parameter  $t_{OP}$ , they presented a criterion that could formally distinguish a stable disc from an unstable one. Nine years later, following the virial theorem for the disc embedded in an external potential, Efstathiou, Lake and Negroponte (1982) proposed an alternative global stability criterion through the parameter  $t^*$ . In order to have a better understanding of the theoretical reasonings that lead the aforementioned authors to pursue a global stability criterion for stellar discs, in this Chapter we report some theoretical topics about the potential theory, its connection to discs and spherically symmetric systems, and the virial theorem for systems of one (or more) component, with a particular focus on the meaning of the gravitational potential energy  $W$ .

## 1.1 Potential theory

Consider a distribution of mass density  $\rho(\mathbf{x}')$ . According to Newton's law of gravitation, the force it exerts on a particle of mass  $m_s$  at position  $\mathbf{x}$  is

$$\mathbf{F}(\mathbf{x}) = m_s \mathbf{g}(\mathbf{x}), \quad \text{where} \quad \mathbf{g}(\mathbf{x}) = G \int d^3 \mathbf{x}' \frac{\mathbf{x}' - \mathbf{x}}{|\mathbf{x}' - \mathbf{x}|^3} \rho(\mathbf{x}') \quad (1.1)$$

is the gravitational field,  $G$  is the gravitational constant and the integral is evaluated over the entire  $\mathbb{R}^3$  space. Since the gravitational field is conservative, we can define the gravitational potential

$$\Phi(\mathbf{x}) = -G \int d^3 \mathbf{x}' \frac{\rho(\mathbf{x}')}{|\mathbf{x}' - \mathbf{x}|}, \quad (\mathbf{x}' \neq \mathbf{x}), \quad (1.2)$$

such that

$$\mathbf{g}(\mathbf{x}) = -\nabla_{\mathbf{x}} \Phi(\mathbf{x}). \quad (1.3)$$

From now on we denote  $\nabla \equiv \nabla_{\mathbf{x}}$  in order to lighten the notation.

A property of the gravitational field is

$$\nabla \cdot \mathbf{g}(\mathbf{x}) = -4\pi G \rho(\mathbf{x}). \quad (1.4)$$

Substituting Equation (1.3) into Equation (1.4), we obtain Poisson's equation

$$\Delta \Phi(\mathbf{x}) = 4\pi G \rho(\mathbf{x}), \quad (1.5)$$

which relates the potential  $\Phi$  of the mass distribution to its density  $\rho$ .

Since Equation (1.3) holds and  $\mathbf{g}$  is conservative, the potential energy  $W$  of the mass distribution can be defined as the work done against the gravitational forces in order to assemble the mass density distribution  $\rho(\mathbf{x})$ . An expression for  $W$  for a self-gravitating system is (see Binney and Tremaine, 2008)

$$W = \frac{1}{2} \int d^3 \mathbf{x} \rho(\mathbf{x}) \Phi(\mathbf{x}). \quad (1.6)$$

$W$  can also be written in a tensorial form through the Chandrasekhar potential-energy tensor  $\mathbf{W}$  (see, e.g., Binney and Tremaine, 2008; Ciotti, 2021):

$$W_{jk} = - \int d^3 \mathbf{x} \rho(\mathbf{x}) x_j \frac{\partial \Phi}{\partial x_k}, \quad (1.7)$$

whose trace is

$$W \equiv \text{tr}(\mathbf{W}) = \sum_{j=1}^3 W_{jj} = - \int d^3 \mathbf{x} \rho(\mathbf{x}) \langle \mathbf{x}, \nabla \Phi(\mathbf{x}) \rangle. \quad (1.8)$$

Equation (1.8) can be also rewritten as Equation (1.6) by substituting for  $\Phi$  (Equation 1.2):

$$\begin{aligned} W_{jk} &= G \int d^3 \mathbf{x} \rho(\mathbf{x}) x_j \frac{\partial}{\partial x_k} \int d^3 \mathbf{x}' \rho(\mathbf{x}') \frac{1}{|\mathbf{x}' - \mathbf{x}|} = \\ &= G \int d^3 \mathbf{x} \int d^3 \mathbf{x}' \rho(\mathbf{x}) \rho(\mathbf{x}') \frac{x_j (x'_k - x_k)}{|\mathbf{x}' - \mathbf{x}|^3}. \end{aligned} \quad (1.9)$$

Note that the differentiation is carried inside the integral because the integration over  $\mathbf{x}'$  does not depend on  $\mathbf{x}$ . In addition,  $\mathbf{x}$  and  $\mathbf{x}'$  are both dummy variables of integration, so we can interchange the labels and write

$$W_{jk} = G \int d^3\mathbf{x}' \int d^3\mathbf{x} \rho(\mathbf{x}')\rho(\mathbf{x}) \frac{x'_j(x_k - x'_k)}{|\mathbf{x} - \mathbf{x}'|^3}. \quad (1.10)$$

Summing Equations (1.9) and (1.10), we obtain

$$W_{jk} = -\frac{1}{2}G \int d^3\mathbf{x} \int d^3\mathbf{x}' \rho(\mathbf{x})\rho(\mathbf{x}') \frac{(x'_j - x_j)(x'_k - x_k)}{|\mathbf{x}' - \mathbf{x}|^3}. \quad (1.11)$$

The trace of both sides of Equation (1.11) gives back Equation (1.6), hence for a self-gravitating system Equations (1.6) and (1.8) are equivalent expressions for the gravitational potential energy  $W$ .

### 1.1.1 Potential theory of spherical systems

A spherically symmetric system of mass density  $\rho(r)$ , where  $r$  is the radial coordinate of the spherical framework  $(r, \theta, \varphi)$ , has two main properties:

**Newton's first theorem:** a spherical shell of mass exerts no net gravitational pull to a body which is inside the shell.

**Newton's second theorem:** the gravitational pull that spherical mass shell exerts on a body outside it is the same that would be exerted if the whole shell mass were concentrated at its centre.

An important consequence of Newton's first theorem is that the gravitational potential  $\Phi(r)$  generated by  $\rho(r)$  is constant inside the shell, namely  $\nabla\Phi(r) = -\mathbf{g}(r) = 0$ . From Newton's first and second theorems, it follows that the gravitational pull a spherical mass distribution  $\rho(r')$  exerts on a unit mass is given by the mass  $M(r)$  interior to  $r$ :

$$\mathbf{F}(r) = -\frac{GM(r)}{r^2}\hat{\mathbf{e}}_r, \quad (1.12)$$

where  $\hat{\mathbf{e}}_r$  is the unit vector in the radial direction and

$$M(r) = 4\pi \int_0^r \rho(r')r'^2 dr'. \quad (1.13)$$

The total gravitational potential at position  $r$ , which is generated by the spherically symmetric system  $\rho(r')$ , may be written as the sum of the contributions given by the mass shells with  $r' < r$  and from the ones with  $r' > r$  (e.g. Binney and Tremaine, 2008):

$$\Phi(r) = -\frac{G}{r} \int_0^r dM(r') - G \int_r^\infty \frac{dM(r')}{r'}, \quad (1.14)$$

where  $M(r')$  is given by Equation (1.13). If we compute  $\mathbf{F} = -\nabla\Phi(r)$ , from Equation (1.14) we will obtain again Equation (1.12).

The total potential gravitational energy of such system is given by taking the definition of  $W$  (1.8), substituting  $\nabla\Phi$  with Equation (1.12) and integrating over  $r \in [0, \infty[$ :

$$W = -4\pi G \int_0^\infty r\rho(r)M(r) dr. \quad (1.15)$$

A consequence of the spherical symmetry is that the potential-energy tensor  $\mathbf{W}$  is diagonal, namely  $W_{jk} = \frac{1}{3}W\delta_{jk}$ , where  $\delta_{jk}$  is the Kronecker delta. For this reason, in this case  $\mathbf{W}$  is also isotropic.

Now, consider a test particle at position  $r$  from the centre of the spherical mass distribution  $\rho(r')$ . For that object we can define the circular speed  $v_c(r)$  as the speed it has in a circular orbit at radius  $r$  in the gravitational field generated by  $\rho(r')$ . Equating  $|\mathbf{F}|$  to the centripetal acceleration  $a_c = v_c^2/r$ , we get the squared circular speed

$$v_c^2(r) = r|\mathbf{F}| = r\frac{d\Phi}{dr} = \frac{GM(r)}{r}. \quad (1.16)$$

From the conservation of the total energy, we can also define the escape speed  $v_e(r)$  (assuming  $\Phi(r) \rightarrow 0$  as  $r \rightarrow \infty$ )

$$v_e(r) = \sqrt{2|\Phi(r)|}. \quad (1.17)$$

Therefore the test particle can escape from the gravitational field  $\Phi(r)$  if its speed is greater or equal to  $v_e(r)$ .

### 1.1.2 Potential theory of galactic discs

We can see any axisymmetric disc as a very flat spheroid and start from the equations of a spheroid in order to obtain the potential of the disc (see, e.g., Binney and Tremaine, 2008, Section 2.6.1). First, consider a homogeneous spheroid of density  $\rho$ , semi-axes  $a$  and  $c$ , which give the axial ratio  $q \equiv c/a$ , mass  $M(a) = \frac{4}{3}\pi\rho qa^3$  and surface density (when projected along the symmetry axis)

$$\Sigma(a, R) = 2\rho q\sqrt{a^2 - R^2}, \quad (1.18)$$

where  $R$  is the cylindrical radius. If we differentiate Equation (1.18) with respect to  $a$ , we will have the mass  $\delta M(a)$  and the surface density  $\delta\Sigma(a, R)$  of a thin homoeoid of density  $\rho$ , semi-major axis  $a$ , thickness  $\delta a$  and axial ratio  $q$ :

$$\delta M(a) = 4\pi\rho qa^2\delta a \quad ; \quad \delta\Sigma(a, R) = \frac{2\rho qa}{\sqrt{a^2 - R^2}}\delta a. \quad (1.19)$$

If we keep  $2\rho qa \equiv \Sigma_0$  constant and let  $q \rightarrow 0$ , we obtain the mass and the surface density of a razor-thin flattened homoeoid:

$$\delta M(a) = 2\pi\Sigma_0 qa\delta a \quad ; \quad \delta\Sigma(a, R) = \frac{\Sigma_0\delta a}{\sqrt{a^2 - R^2}}. \quad (1.20)$$

Now, we can build a razor-thin disc of known surface density  $\Sigma(R)$  by finding a set of homoeoids whose combined surface density equals  $\Sigma(R) \forall R \in [0, \infty[$ . In other words, we have to find the function  $\Sigma_0(a)$  that satisfies the following Abel integral equation:

$$\Sigma(R) = \sum_{a \leq R} \delta\Sigma(a, R) = \int_R^\infty da \frac{\Sigma_0(a)}{\sqrt{a^2 - R^2}}, \quad (1.21)$$

whose solution is

$$\Sigma_0(a) = -\frac{2}{\pi} da \int_a^\infty dR \frac{R\Sigma(R)}{\sqrt{R^2 - a^2}}. \quad (1.22)$$

From this point of view, the potential of a razor-thin disc can be seen as the sum of the potentials of every thin homoeoid that forms the disc. According to Gauss's theorem, while the gravitational field is discontinuous across a plane of finite surface density, the potential remains continuous. Therefore, there is a negligible difference between the potential just above or below the disc and the potential in the equatorial plane. As a result, to find the potential in the  $z = 0$  plane, we only need to compute the potential at points that are external to all homoeoids and then take the limit  $z \rightarrow 0$ .

From Cuddeford (1993), the general expression of the potential of a razor-thin axisymmetric disc with arbitrary  $\Sigma(R)$  is

$$\Phi(R, z) = 4G \int_0^\infty da \arcsin\left(\frac{2a}{\sqrt{+} + \sqrt{-}}\right) \frac{d}{da} \int_a^\infty dR' \frac{R'\Sigma(R')}{\sqrt{R'^2 - a^2}}, \quad (1.23)$$

where  $\sqrt{\pm} = \sqrt{z^2 + (a \pm R)^2}$ . The potential at  $z = 0$  is

$$\Phi(R, 0) = 4G \int_0^\infty da \arcsin\left(\frac{2a}{(a+R) + |a-R|}\right) \frac{d}{da} \int_a^\infty dR' \frac{R'\Sigma(R')}{\sqrt{R'^2 - a^2}}. \quad (1.24)$$

Note that the argument of arcsin in Equation (1.24) is

$$\frac{2a}{(a+R) + |a-R|} = \begin{cases} 1 & R \leq a, \\ a/R & \text{otherwise.} \end{cases}$$

To obtain the circular speed in the equatorial plane  $z = 0$ , we differentiate Equation (1.24) with respect to  $R$ :

$$v_c^2(R) = R \left( \frac{d\Phi}{dR} \right)_{z=0} = -4G \int_0^R da \frac{a}{\sqrt{R^2 - a^2}} \frac{d}{da} \int_a^\infty dR' \frac{R'\Sigma(R')}{\sqrt{R'^2 - a^2}}. \quad (1.25)$$

## 1.2 The virial theorem

### 1.2.1 Tensor virial theorem

Consider a self-gravitating system described by a distribution function  $f(\mathbf{x}, \mathbf{v})$ . If it is at equilibrium, the system satisfies the second-order tensor virial theorem (see, e.g., Binney and Tremaine, 2008)

$$\frac{1}{2} \frac{d^2 I_{jk}}{dt^2} = 2K_{jk} + W_{jk}, \quad (\forall j, k = 1, 2, 3), \quad (1.26)$$

where

$$I_{jk} = \int d^3\mathbf{x} d^3\mathbf{v} f(\mathbf{x}, \mathbf{v}) x_j x_k \quad \text{and} \quad K_{jk} = \int d^3\mathbf{x} d^3\mathbf{v} f(\mathbf{x}, \mathbf{v}) \langle v_j(\mathbf{x}) v_k(\mathbf{x}) \rangle \quad (1.27)$$

are the second order mass tensor and the kinetic-energy tensor, respectively, and  $W_{jk}$  is the potential-energy tensor (Equation 1.7) with  $\rho(\mathbf{x}) = \int d^3\mathbf{v} f(\mathbf{x}, \mathbf{v})$ .

The kinetic-energy tensor  $\mathbf{K}$  can be split into contributions from ordered ( $T_{jk}$ ) and random ( $\Pi_{jk}$ ) motions:

$$K_{jk} = T_{jk} + \frac{1}{2} \Pi_{jk}, \quad (1.28)$$

where

$$T_{jk} = \frac{1}{2} \int d^3\mathbf{x} \rho(\mathbf{x}) \langle v_j(\mathbf{x}) \rangle \langle v_k(\mathbf{x}) \rangle \quad (1.29a)$$

and

$$\Pi_{jk} = \int d^3\mathbf{x} \rho(\mathbf{x}) \sigma_{jk}^2(\mathbf{x}) \quad (1.29b)$$

are the ordered and random kinetic-energy tensors, respectively. Here

$$\langle v_j(\mathbf{x}) \rangle = \frac{1}{\rho(\mathbf{x})} \int d^3\mathbf{v} v_j(\mathbf{x}) f(\mathbf{x}, \mathbf{v}) \quad (1.30)$$

is the mean velocity and

$$\begin{aligned} \sigma_{jk}^2(\mathbf{x}) &= \frac{1}{\rho(\mathbf{x})} \int d^3\mathbf{v} (v_j(\mathbf{x}) - \langle v_j(\mathbf{x}) \rangle) (v_k(\mathbf{x}) - \langle v_k(\mathbf{x}) \rangle) f(\mathbf{x}, \mathbf{v}) = \\ &= \langle v_j(\mathbf{x}) v_k(\mathbf{x}) \rangle - \langle v_j(\mathbf{x}) \rangle \langle v_k(\mathbf{x}) \rangle \end{aligned} \quad (1.31)$$

is the velocity-dispersion tensor.

In case of a steady state system, the time derivative of Equation (1.26) vanishes and the tensor virial theorem gives

$$2K_{jk} + W_{jk} = 0. \quad (1.32)$$

## 1.2.2 Scalar virial theorem

If we take the trace of Equation (1.26), we obtain the scalar version of the virial theorem

$$\frac{1}{2} \frac{d^2 I}{dt^2} = 2K + W, \quad (1.33)$$

where  $I$ ,  $K$  and  $W$  are the traces of their corresponding tensors  $\mathbf{I}$ ,  $\mathbf{K}$  and  $\mathbf{W}$ , respectively.

In a steady state system, the time derivative on the left hand side of Equation (1.33) vanishes and the scalar virial theorem gives

$$2K + W = 0. \quad (1.34)$$

## 1.2.3 Scalar virial theorem for a two-component system

Let us consider the case of a two-component self-gravitating system with mass densities  $\rho_1$  and  $\rho_2$ , respectively, with related potentials  $\Phi_1$  and  $\Phi_2$ . If the system is virialized, the scalar form (at the second order) of the virial theorem for such system is given by Equation (1.33), where now  $I = I_1 + I_2$  and  $K = K_1 + K_2$ . Focusing on the gravitational potential energy  $W$ , Equation (1.8) can be developed by setting  $\rho = \rho_1 + \rho_2$  and  $\Phi = \Phi_1 + \Phi_2$ :

$$\begin{aligned} W &= - \int d^3\mathbf{x} (\rho_1(\mathbf{x}) + \rho_2(\mathbf{x})) \langle \mathbf{x}, \nabla(\Phi_1(\mathbf{x}) + \Phi_2(\mathbf{x})) \rangle = \\ &= - \int d^3\mathbf{x} \rho_1(\mathbf{x}) \langle \mathbf{x}, \nabla\Phi_1(\mathbf{x}) \rangle - \int d^3\mathbf{x} \rho_2(\mathbf{x}) \langle \mathbf{x}, \nabla\Phi_2(\mathbf{x}) \rangle + \\ &\quad - \int d^3\mathbf{x} \rho_1(\mathbf{x}) \langle \mathbf{x}, \nabla\Phi_2(\mathbf{x}) \rangle - \int d^3\mathbf{x} \rho_2(\mathbf{x}) \langle \mathbf{x}, \nabla\Phi_1(\mathbf{x}) \rangle = \\ &= W_1 + W_2 + W_{12} + W_{21}, \end{aligned} \quad (1.35)$$

where  $W_1$  and  $W_2$  refer to the gravitational self-energies of the components 1 and 2, respectively, while  $W_{12}$  and  $W_{21}$  are the gravitational interaction energies between the two components (index ‘12’ is related to  $\rho_1$  and  $\Phi_2$ ; vice versa, the notation ‘21’ matches  $\rho_2$  to  $\Phi_1$ ). After some calculations of the last two terms on the right hand side of Equation (1.35) (see Appendix A, Equation A.6), we get

$$W_{12} + W_{21} \equiv W_{1\leftrightarrow 2} = \int d^3\mathbf{x} \rho_1(\mathbf{x})\Phi_2(\mathbf{x}) = \int d^3\mathbf{x} \rho_2(\mathbf{x})\Phi_1(\mathbf{x}). \quad (1.36)$$

Therefore, recalling the equivalence between Equations (1.6) and (1.8) for gravitational self-energies, we can also write the total gravitational potential energy as

$$\begin{aligned} W &= \frac{1}{2} \int d^3\mathbf{x} (\rho_1(\mathbf{x}) + \rho_2(\mathbf{x}))(\Phi_1(\mathbf{x}) + \Phi_2(\mathbf{x})) = \\ &= \frac{1}{2} \int d^3\mathbf{x} \rho_1(\mathbf{x})\Phi_1(\mathbf{x}) + \frac{1}{2} \int d^3\mathbf{x} \rho_2(\mathbf{x})\Phi_2(\mathbf{x}) + \int d^3\mathbf{x} \rho_1(\mathbf{x})\Phi_2(\mathbf{x}) = \\ &= W_1 + W_2 + W_{1\leftrightarrow 2}. \end{aligned} \quad (1.37)$$

The scalar virial theorem applied to the two components gives

$$\frac{1}{2} \frac{d^2 I_1}{dt^2} = 2K_1 + W_1 + W_{12}, \quad (1.38)$$

$$\frac{1}{2} \frac{d^2 I_2}{dt^2} = 2K_2 + W_2 + W_{21}. \quad (1.39)$$

In fact, the sum of Equations (1.38) and (1.39) equals Equation (1.33).

#### 1.2.4 Scalar virial theorem for a self-gravitating system embedded in an external gravitational potential field

If we consider a self-gravitating system described by the mass density distribution  $\rho(\mathbf{x}) = \int f(\mathbf{x}, \mathbf{v}) d^3\mathbf{v}$  within an external gravitational potential  $\Phi_{ext}(\mathbf{x})$ , the right hand side of Equation (1.26) gains an extra term (Binney and Tremaine, 2008):

$$\frac{1}{2} \frac{d^2 I_{jk}}{dt^2} = 2K_{jk} + W_{jk} + V_{jk}, \quad (1.40)$$

where

$$V_{jk} = -\frac{1}{2} \int d^3\mathbf{x} \rho(\mathbf{x}) \left( x_j \frac{\partial \Phi_{ext}}{\partial x_k} + x_k \frac{\partial \Phi_{ext}}{\partial x_j} \right) = -\frac{1}{2} (W_{jk}^{ext} + W_{kj}^{ext}) \quad (1.41)$$

is the potential-energy tensor  $\mathbf{V}$  related to  $\Phi_{ext}$ , whose trace is

$$\begin{aligned} V = \text{tr}(\mathbf{V}) &= \sum_{j=1}^3 V_{jj} = -\sum_{j=1}^3 \frac{1}{2} \int d^3\mathbf{x} \rho(\mathbf{x}) \left( 2x_j \frac{\partial \Phi_{ext}}{\partial x_j} \right) = \\ &= -\int d^3\mathbf{x} \rho(\mathbf{x}) \langle \mathbf{x}, \nabla \Phi_{ext}(\mathbf{x}) \rangle. \end{aligned} \quad (1.42)$$

If we look at Section 1.2.3, we see that Equation (1.42) is just the gravitational potential energy of interaction between the mass density of the self-gravitating system and the potential of another system with mass density distribution  $\rho_{ext}(\mathbf{x})$  and potential  $\Phi_{ext}(\mathbf{x})$ . Thus, the scalar virial theorem for this system

$$\frac{1}{2} \frac{d^2 I}{dt^2} = 2K + W + V \quad (1.43)$$

is equivalent to Equations (1.38) or (1.39).

### 1.2.5 Gravitational self-energy and gravitational interaction energy

It is useful to distinguish two types of  $|W|$ . In a system with density profile  $\rho(\mathbf{x})$  and potential  $\Phi(\mathbf{x})$ , both related by Poisson's equation (1.5), the total gravitational potential energy can be expressed by Equations (1.6) or (1.8), without distinction:

$$W = \frac{1}{2} \int d^3\mathbf{x} \rho(\mathbf{x}) \Phi(\mathbf{x}) = - \int d^3\mathbf{x} \rho(\mathbf{x}) \langle \mathbf{x}, \nabla \Phi(\mathbf{x}) \rangle. \quad (1.44)$$

Equation (1.44) is correct if we are referring either to the gravitational self-energy of the whole system or to the gravitational self-energies of the single components the system is made of (e.g. Binney and Tremaine, 2008; Ciotti, 2021). In other words, it is necessary that Poisson's equation (1.5) holds for  $\rho(\mathbf{x})$  and  $\Phi(\mathbf{x})$  of the system (or the single components) such that Equation (1.44) is correct, because we should remember that Equation (1.6) is obtained via Poisson's equation (1.5) (see Binney and Tremaine, 2008, p. 59).

However, if we now consider a system with density  $\rho_1(\mathbf{x})$  and we want to compute its gravitational potential energy due to the interaction with another potential  $\Phi_2(\mathbf{x})$ , Equation (1.44) does not hold anymore, as Poisson's equation (1.5) is no longer applicable. For this reason, we should use the trace of the Chandrasekhar potential-energy tensor (Equation 1.8)

$$W_{12} = - \int d^3\mathbf{x} \rho_1(\mathbf{x}) \langle \mathbf{x}, \nabla \Phi_2(\mathbf{x}) \rangle, \quad (1.45)$$

where the subscripts 1 and 2 are related to the system and the external potential, respectively. As seen in Subsection 1.2.3 (Equation 1.36) and in Appendix A (Equation A.6), we can write the gravitational potential energy of interaction between the components in a similar form of the self-energy (Equation 1.6) if we sum the mutual interaction energies to obtain  $W_{1\leftrightarrow 2}$  (Equation 1.36); otherwise, we have to use only Equation (1.45) via the Chandrasekhar notation.

The gravitational self-energy (Equation 1.44) is sometimes labelled with  $U$  (e.g. Ciotti, 2021) to distinguish it from the gravitational interaction energy between two components of a system (Equation 1.45), but for all of this work, as we did in this Chapter, we will use subscripts under  $W$  in order to distinguish the gravitational self-energy from the gravitational energy interaction between two components.

# Chapter 2

## Global stability parameters for stellar discs

After we have explored the theoretical tools which allow us to comprehend the main meaning of global equilibrium of a system, we now focus on the construction of the global stability parameters  $t_{OP}$  and  $t^*$  proposed by Ostriker and Peebles (1973) and Efstathiou, Lake and Negroponte (1982), respectively. In particular, in this Chapter we report an important discussion about the universal validity of these two parameters in many disc-halo systems. In fact, from numerical and theoretical work reviewed by Efstathiou, Lake and Negroponte (1982),  $t_{OP}$  is very sensitive to the halo mass and concentration, thus stating the stability of the disc even though, in some cases, the latter is not stable. For this reason Efstathiou, Lake and Negroponte (1982) have introduced a new global stability parameter  $t^*$ , which tries to solve the issues noticed in  $t_{OP}$ . However, as we will discuss at the end of this Chapter,  $t^*$  is not universally accepted by the literature (e.g., Athanassoula, 2008; Romeo et al., 2023) and thus the pursuit of a global stability criterion for stellar discs is still open. In this work, we present a new parameter  $t_W$  which we investigate in detail in Chapter 4.

## 2.1 Ostriker-Peebles's stability criterion

Ostriker and Peebles (1973) (hereafter OP73) presented a numerical study which investigated the stability of flattened (disc) galaxies. Some theoretical reasoning shows that a highly flattened disc (made of gas and/or stars) which is mainly supported by rotation might go through large-scale instabilities. Let us consider a galactic disc made of stars whose circular motion is dominant with respect to their random stellar motions (measured by the stellar velocity dispersion  $\sigma$ ). In other words, the condition  $v/\sigma \gg 1$  leads to a 'cold' galactic disc. The thin stellar disc of Galaxy is cold, but it does not show evidence of these large-scale instability. So OP73 raised two questions: is a rotationally supported disc stable or not? What are the conditions of stability in such systems?

To investigate the problem of stability with their simulations, OP73 introduced some useful energy-related quantities. Following the treatment of OP73, we report here the analysis that leads to the formulation of the Ostriker-Peebles's stability criterion.

### 2.1.1 Construction of OP's global stability parameter

An  $N$ -body system in equilibrium must satisfy the scalar virial theorem at the second order (1.33), which we may rewrite - following the notation of Section 1.2 - as

$$2T + \Pi + W = 0, \quad (2.1)$$

where  $T$ ,  $\Pi$  and  $W$  are the traces of the second-order tensors  $\mathbf{T}$  (1.29a),  $\mathbf{\Pi}$  (1.29b) and  $\mathbf{W}$  (1.8), respectively.

OP assumed an axisymmetric stellar disc embedded in an external spherical system - the 'halo' -, which is rigid and non-rotating. By 'rigid' we mean the halo is represented by an external potential and is unable to respond to the disc evolution (see Athanassoula, 2008). Hereafter we may use the term 'unresponsive', referring to a non-rotating rigid halo.

We may rewrite explicitly the kinetic terms<sup>1</sup> of Equation (2.1) as

$$T = \frac{1}{2} \int \langle \mathbf{v}(\mathbf{x}) \rangle^2 \rho(\mathbf{x}) d^3\mathbf{x} \quad (2.2)$$

$$\text{and } \Pi = \int (\mathbf{v}(\mathbf{x}) - \langle \mathbf{v}(\mathbf{x}) \rangle)^2 \rho(\mathbf{x}) d^3\mathbf{x}, \quad (2.3)$$

where  $\rho(\mathbf{x}) = \int f(\mathbf{x}, \mathbf{v}) d^3\mathbf{v}$  is the density distribution of the system (disc and halo) and

$$\langle \mathbf{v}(\mathbf{x}) \rangle_{OP} = \frac{1}{\rho(\mathbf{x})} \int \mathbf{v} f(\mathbf{x}, \mathbf{v}) d^3\mathbf{v} \quad (2.4)$$

is the streaming velocity of the particles at position  $\mathbf{x}$ .  $T$  and  $\Pi$  are the kinetic energy of rotation and the random kinetic energy of the system, respectively. It should be noted that if we consider a steady rotating disc,  $\langle \mathbf{v}(\mathbf{x}) \rangle$  is the steady rotational motion of the disc particles. Given that the halo is non-rotating,  $T_h = 0$ . For this reason, and also to lighten the notation, when we talk about  $T$ , we are only referring to the kinetic energy of the disc particles  $T_d$ . Conversely,  $\Pi = \Pi_d + \Pi_h$ .

---

<sup>1</sup>OP73 defined the random kinetic energy  $T_{\text{rand}}$  such that  $T_{\text{rand}} = \Pi/2$ .

In Equation (2.1) the potential term, which corresponds to the total gravitational potential of the disc-halo system, is

$$W = \frac{1}{2} \int \int \Phi(\mathbf{x}) f(\mathbf{x}, \mathbf{v}) d^3\mathbf{x} d^3\mathbf{v}, \quad (2.5)$$

where  $\Phi = \Phi_d + \Phi_h$  is the total gravitation potential of the system, which can be decomposed into two terms related to the disc and the halo, respectively. Recalling that  $\rho(\mathbf{x}) \equiv \rho_d(\mathbf{x}) + \rho_h(\mathbf{x})$  and the result carried out in Appendix A (Equation A.6), Equation (2.5) becomes

$$\begin{aligned} W &= \frac{1}{2} \int (\rho_d(\mathbf{x}) + \rho_h(\mathbf{x})) (\Phi_d(\mathbf{x}) + \Phi_h(\mathbf{x})) d^3\mathbf{x} = \\ &= \frac{1}{2} \int d^3\mathbf{x} \rho_d(\mathbf{x}) \Phi_d(\mathbf{x}) + \frac{1}{2} \int d^3\mathbf{x} \rho_h(\mathbf{x}) \Phi_h(\mathbf{x}) + \int d^3\mathbf{x} \rho_d(\mathbf{x}) \Phi_h(\mathbf{x}) = \\ &= W_d + W_h + W_{d\leftrightarrow h}, \end{aligned} \quad (2.6)$$

where the expressions for  $W_d$ ,  $W_h$  and  $W_{d\leftrightarrow h}$  are taken from Equation (1.37).

Now, if we divide Equation (2.1) by  $|W|$  and, at the same time, if we define:

$$t_{OP} = \frac{T}{|W|} \quad (2.7)$$

$$\text{and } u_{OP} = \frac{\Pi}{2|W|}, \quad (2.8)$$

then we get

$$t_{OP} + u = \frac{1}{2}; \quad 0 \leq t_{OP} \leq \frac{1}{2}. \quad (2.9)$$

Both  $t_{OP}$  and  $u_{OP}$  can be seen as parameters which regulate the rotation and the pressure supports in the system, which, combined, give equilibrium.

### 2.1.2 General considerations on $t_{OP}$

Before OP73, Miller et al. (1970) and Hohl (1971), by means of numerical simulations, found that flat cold systems ( $u/t_{OP} \ll 1$ ) are subject to large-scale instabilities.

In their work, OP73 focused on incompressible fluid systems in the hypothesis of an axisymmetric body with uniform density and rotation – the Maclaurin spheroids. For such axisymmetric systems, in 1742 Colin Maclaurin found an exact solution for the equilibrium, which is reported here as a relation between  $t_{OP}$  and the eccentricity  $e$  (Ostriker and Peebles, 1973; Bodenheimer and Ostriker, 1973; Binney and Tremaine, 2008):

$$t_{OP} = \frac{1}{2} [(3e^{-2} - 2) - 3(e^{-2} - 1)^{1/2} (\arcsin e)^{-1}]. \quad (2.10)$$

From Equation (2.10) we can express the stability properties of such systems in terms of  $t_{OP}$ .

Following OP73, in uniformly rotating systems we distinguish ordinary (or dynamical) from secular instability (Hunter, 1977). The former is related to a system whose amplitude of some mode grows exponentially in time, starting from an initially infinitesimal perturbation; the latter refers to a system which is dynamically stable but

the presence of small additional dissipative forces can let some temporally oscillating perturbations to grow. A system is also said to be secularly unstable when it is capable, at least from an energetic point of view, of deviating from the equilibrium state because of the presence of a relevant perturbation (Lebovitz, 1961).

From the analytical study of the Maclaurin spheroids (see, e.g., Lebovitz, 1961, p. 508)<sup>2</sup>, if  $t_{OP} > 0.1376$  then the system is secularly unstable, while if  $t_{OP} > 0.2738$  (which is the limit for zero-viscosity Maclaurin spheroids) then it is dynamically unstable for the bar formation. In case the axisymmetry is held during the evolution of the spheroid, then for  $t_{OP} > 0.3589$  the system is secularly unstable to ring formation and for  $t_{OP} > 0.4574$  it is dynamically unstable to ring formation. These results are exact if we consider the Maclaurin spheroids, but OP73 stated through  $N$ -body simulations that these results are also valid for fluid 'stellar' systems, which become secularly unstable when

$$t_{OP} > t_{OP,crit} = 0.137 \pm 0.002. \quad (2.11)$$

The secular instability originates because of the advantage a rapidly rotating object has in maximizing its moment of inertia (OP73). Beyond  $t_{OP,crit}$ , OP73 stated that bar-like equilibrium exists with lower total energy but same mass, central density and angular momentum.

The bar instability is characterized by the development of eccentricity in the equatorial plane and a flattening at the poles. After the instability, the motions can be characterized by a very stretched spheroid, which may be prone to fragmentation. According to OP73, the bar formation process in these spheroids seems to be large-scale and irreversible.

### 2.1.3 Numerical simulations

OP73 integrated the equations of motion of the  $N$ -body system in three dimensions. Besides, they assumed an additional spherical component – which they called 'halo' – with an assumed mass density distribution  $\Sigma(R) \propto R^{-1}$ . OP73 have built the halo such that it has the same size of the stellar disc ( $R_{h,max} = R_{d,max} \equiv R_{max}$ ).

The dynamical time used by OP73 is the orbital time  $\tau$  for the particles in the outermost part of the original disc.

Details about OP73's simulations are reported in Appendix B, Section B.1.

### 2.1.4 Results

Simulations were run for a total time of  $1\tau$ . OP73 noted that at the end of their simulations, the disc had twice the thickness with respect to its starting configuration. Besides, they tried to measure the bar-like modes using the Fourier analysis of the  $m = 2$  mode, but they found out that this mode increased at first, but at the end they behaved in a "complicated way", as OP73 stated, because the bar disc was not maintained straightly during the whole simulation.

OP73 analysed the results of their simulations for a disc-only system, noting that a large-scale bar develops after a short period of adjustment to initial conditions: the radial motions increase in the disc plane, at  $t = 0.2\tau$  the bar is forming and at  $t = 0.6\tau$

---

<sup>2</sup>In the paper, inequalities are reported as functions of  $e$ .

the bar is prominent. Meanwhile, the velocity distributions are more isotropic in the disc plane  $(v_\varphi, v_R)$ . At  $t = 1\tau$  the system is approaching a stationary state, also returning to an axisymmetric configuration, and critical value of the stability parameter  $t_{OP} \simeq 0.1 \div 0.2$  (OP73, Figure 2). OP73 noticed that these results are insensitive to the choice of the time step  $\Delta t$ , even though  $\Delta t$  has to be chosen so that the numerical method is stable during the whole integration of the  $N$ -body system.

In case of a disc-halo system, the halo is assumed to be steady and gives a contribution to the particle velocities through its potential. The introduction of the halo increases  $|W|$  and the kinetic energy of rotation  $T$ , but the final result is that  $t_{OP}$  is lower than in the disc-only system – assuming the same disc configuration. While in the disc-only simulations there is a bar formation, in the disc-halo case the disc does not show violent instability and  $t_{OP}$  is unchanged through the time. When the halo-to-disc mass ratio  $M_h/M_d \geq 1$ ,  $t_{OP} \leq 0.15$ .

### 2.1.5 Conclusions

OP73 discussed about the reality of the instability shown in their simulations, comparing with other contemporary numerical studies: Miller et al. (1970), Hohl (1971) and Miller (1971), who used about  $10^5$  particles, gave a critical value of  $t_{OP,crit}$  similar to Condition (2.11). In particular, Hohl (1971) noticed that at the end of the simulation the velocity dispersion of the particles is ”much larger than that given by Toomre’s criterion”.

OP73 concluded that Condition (2.11) represents approximately the maximum rotational energy that an axisymmetric stellar system can contain in order to remain stable to the formation of a bar.

There is also an interesting conclusion about the (spherical) halo around the galactic disc: OP73 showed that the stability of the stellar disc is given by an external halo, whose mass lowers the value of  $t_{OP}$  and prevents the formation of a bar. Nowadays, the fact that galaxies have surrounding dark matter halos has become the standard interpretation of their kinematics (see, e.g., Cimatti et al., 2019).

## 2.2 Efstathiou, Lake and Negroponte’s $t^*$ parameter

Much work has been done to test the Ostriker and Peebles’s criterion (2.11) e.g., Hohl, 1976; Zang and Hohl, 1978 and some possible counter-examples have been discussed (see, e.g., Zang, 1976; Miller, 1978; Berman and Mark, 1979). Efstathiou, Lake and Negroponte 1982 (hereafter ELN82) proposed a revised study of the global stability of discs, proposing an alternative parameter  $t^*$  similar to  $t_{OP}$  (OP73). We report here the theoretical aspects that lead to the formulation of the Efstathiou, Lake and Negroponte’s stability criterion.

### 2.2.1 Construction of ELN’s global stability parameter

ELN82 started from the virial theorem satisfied by an  $N$ -body system in equilibrium (2.1), with the same Definitions (2.2), (2.3) and (2.5). Differently from OP73, now assuming cylindrical coordinates  $(R, \varphi, z)$ , in ELN82’s work the mean circular velocity

$\langle v(R) \rangle$  is computed not within a flat ring, but in a 3D cylindrical shell at a distance  $R$  from the axis of symmetry:

$$\langle v_\varphi(R) \rangle_{ELN} = \frac{\int f(\mathbf{x}, \mathbf{v}) v_\varphi dz d^3\mathbf{v}}{\int \rho(R, \varphi, z) dz}, \quad (2.12)$$

where  $f(\mathbf{x}, \mathbf{v}) \equiv f(R, \varphi, z, v_R, v_\varphi, v_z)$  is the distribution function of the system in cylindrical coordinates,  $v_\varphi = v_\varphi(R, z)$  is the circular velocity about the axis of symmetry taken, which is assumed to be the  $z$ -axis. When there are motions in the meridional plane  $(R, z)$ , Equation (2.12) differs from the definitions of OP73, who used the local streaming velocity (Equation 2.4).

Assuming an axisymmetric disc embedded in another system – a halo (on which we focus here) or another disc – and recalling Equations (1.38) and (1.39), the virial theorem for the disc can be formulated as

$$2T_d + \Pi_d + (1 + f_{\text{ext}})W_d = 0, \quad (2.13)$$

where the subscript  $d$  refers to the disc,  $W_d$  is the self-gravitational potential energy of the disc (see Equation 1.6) and  $f_{\text{ext}}$  is the fraction of the force acting on the disc that is due to the external halo potential:

$$1 + f_{\text{ext}} = \frac{\int \rho_d(\mathbf{x}) \langle \mathbf{x}, \mathbf{F}_{\text{tot}} \rangle d^3\mathbf{x}}{\int \rho_d(\mathbf{x}) \langle \mathbf{x}, \mathbf{F}_d \rangle d^3\mathbf{x}}, \quad (2.14)$$

where  $\mathbf{F}_{\text{tot}}$  and  $\mathbf{F}_d$  are the total force and the force due to the disc mass, respectively. Equation (2.14) can be related to the gravitational potential energies  $W_{\text{dh}}$  and  $W_d$ :

$$1 + f_{\text{ext}} = \frac{\int \rho_d(\mathbf{x}) \langle \mathbf{x}, \nabla \Phi_{\text{tot}} \rangle d^3\mathbf{x}}{\int \rho_d(\mathbf{x}) \langle \mathbf{x}, \nabla \Phi_d \rangle d^3\mathbf{x}} = \frac{\int \rho_d(\mathbf{x}) \langle \mathbf{x}, \nabla (\Phi_d + \Phi_h) \rangle d^3\mathbf{x}}{\int \rho_d(\mathbf{x}) \langle \mathbf{x}, \nabla \Phi_d \rangle d^3\mathbf{x}} = 1 + \frac{W_{\text{dh}}}{W_d}. \quad (2.15)$$

Thus  $f_{\text{ext}} = W_{\text{dh}}/W_d$  is the ratio between the gravitational potential energy of the disc particles due to the halo potential and the gravitational self-energy of the disc. For this reason, Equation (2.13) can also be rewritten in a similar form of Equations (1.38) and (1.39):

$$2T_d + \Pi_d + W_d + W_{\text{dh}} = 0. \quad (2.16)$$

Starting from these definitions, ELN82 defined

$$t^* = \frac{T_d}{(1 + f_{\text{ext}})^2 |W_d|} \quad (2.17)$$

$$\text{and } u^* = \frac{\Pi_d}{2(1 + f_{\text{ext}})^2 |W_d|}, \quad (2.18)$$

such that

$$t^* + u^* = \frac{1}{2}(1 + f_{\text{ext}}). \quad (2.19)$$

In case the densities of the disc  $\rho_d(\mathbf{x})$  and the total system  $\rho_{\text{tot}}(\mathbf{x})$  are related by  $\rho_d = \xi \rho_{\text{tot}}$ , we have

$$\rho_d(\mathbf{x}) = \frac{\rho_{\text{tot}}(\mathbf{x})}{1 + f_{\text{ext}}} \quad (2.20)$$

and  $t^* = t_{OP}$  (ELN82). Of course, we also have  $t^* = t_{OP}$  when we consider a disc-only system, namely  $\mathbf{F}_{\text{tot}} = \mathbf{F}_d$ .

ELN82 argued that  $t^*$  has some advantages with respect to  $t_{OP}$ . The stabilizing influence of any rigid component (e.g. the halo) should depend only on the force it exerts on the disc. For example, a small point mass with a divergent gravitational energy or a massive spherical shell enclosing the whole subsystem lowers  $t_{OP}$ , but it is expected to have little or no effect on the stability of the subsystem. In  $t^*$  computation, averaging the mean velocity over cylinders rather than flat rings is justified by the weak  $z$ -dependence of the bar-like mode. This latter difference is not important for the two-dimensional systems ELN82 considered in their paper, but is relevant to three-dimensional systems.

## 2.2.2 Numerical simulations

ELN82 focused on the stability of galactic discs with exponential surface density profile:

$$\Sigma_d(R) = \left( \frac{\alpha_d^2 M_d}{2\pi} \right) \exp(-\alpha_d R), \quad (2.21)$$

where  $R$  is the cylindrical radius,  $M_d$  is the total disc mass and  $\alpha_d$  is the scale length of the exponential disc. Considering a disc-halo system with a rigid halo component, the resulting rotation curve of the disc particles is:

$$v_d(R) = v_{max} \left( \frac{R^2}{R^2 + R_{max}^2} \right)^{1/2} \left[ 1 - \gamma \ln \left( \frac{R^2}{R^2 + R_{max}^2} \right) \right]^{1/2}, \quad (2.22)$$

where  $v_{max}$  is the maximum rotational velocity of the disc,  $R_{max}$  is the disc size and  $\gamma = (\alpha_d R_{max}/2)^2 (\alpha_d M_d G / v_{max}^2)$ . These models form a two-parameter family in the dimensionless parameters  $\hat{R}_{max} \equiv \alpha_d R_{max}$  and  $\hat{v}_{max} \equiv v_{max} / (\alpha_d M_d G)^{1/2}$  and were proposed by (Fall and Efstathiou, 1980) as relatively simple first-order approximations to the mass distribution in real disc galaxies, especially late types (LTG). The halo properties are determined by  $\hat{R}_{max}$  and  $\hat{v}_{max}$ , which measure the halo concentration and the halo-to-disc mass ratio within a certain radius  $R$ , respectively. Since the parameter  $\hat{R}_{max}$  is related to the concentration of the halo component, models with small  $\hat{R}_{max}$  possess a ‘bulge’, and not an extended halo.

ELN82 deepened the study of bar instability in stellar discs using different models and some tools of diagnostics like the bar strength, the bar length and  $m = 2$  modes. More details of their related results, in addition to ELN82’s comparison of the numerical work with the observational data, are available in Appendix B.

## 2.2.3 Results

The evolution of ELN82’s models differs in detail. Models with  $\hat{v}_{max} \leq 0.8$  have a fast development of large  $m = 2$  modes, which tend to decay to a constant amplitude. This behaviour is related to the growth of a multi-armed spiral pattern. The initial rise of the  $A_2/A_0$  ratio is given by the interference of these spiral patterns which rapidly decay, leaving a strong bar inside a roughly axisymmetric distribution of particles.

In ELN82’s simulations the disc typically evolves until the Toomre (1964) parameter  $Q \simeq 1.5 \div 2$  in its inner regions ( $\alpha_d R \leq 3$ ) and  $Q \simeq 3 \div 4$  in the outer parts, even if it is stable to bar formation. Furthermore, the authors concluded that the initial Gaussian velocity distribution remains roughly Gaussian after several dynamical times

$\tau$ , where  $\tau$  is the orbital period of a particle at the half-mass radius of the disc (see Section B.2.1).

ELN82 showed that stable models to bar formation keep their exponential distribution through the evolution, even though there is an increase of the density in the central zone of the disc. (Hohl, 1970) and (Zang and Hohl, 1978) have noticed that the surface density profiles of bar unstable models have final density profiles which can be approximated by the sum of two exponential models.

The formation of a bar passes through many stages: at first, a bar forms with length proportional to the turnover radius of the rotation curve. Then the bar grows by transferring angular momentum to the outer parts of the disc. The final bar length may be only dependent on the initial rotation curve, in particular in highly concentrated models. ELN82 reported that a complication in studying the formation and the evolution of the bar is that at the beginning of the simulation the bar-like modes are superposed with the spiral pattern.

The evolution in surface density is significant when the models are bar unstable and the final density profiles are not exponential, because a significant redistribution of angular momentum can occur due to torques from high order instabilities.

## 2.2.4 Conclusions

Through several numerical simulations of different stellar disc models embedded in fixed potentials – the halo –, ELN82 have focused their work on a family of models characterized by two parameters  $\hat{R}_{max}$  and  $\hat{v}_{max}$ , which are related to the halo mass concentration and to the halo-to-disc mass ratio  $M_h/M_d$ , respectively. In particular, those families of galaxies that satisfy Toomre’s (1964) criterion ( $Q > 1$ ) with

$$\hat{v}_{max} \leq 1.1 \quad \text{for} \quad 0.1 \leq \hat{R}_{max} \leq 1.3 \quad \Rightarrow \quad t^* \geq 0.2 \quad (2.23)$$

are stable to axisymmetric instabilities but unstable to bar formation. ELN82 stressed that this result is insensitive both to of the initial surface density of the model and to the shape of the rotation curve. In addition, for the previous configurations, stability properties do not seem to depend to the increase of the velocity dispersion content in the central parts of the disc, even though random motions generally contribute to stability (see, e.g., Athanassoula and Sellwood, 1986).

Since  $t^*$  is strictly related to the parameters  $\hat{v}_{max}$  and  $\hat{R}_{max}$ , not only ELN82’s criterion (2.23) is usually reported in terms of  $\hat{v}_{max}$  without the range in  $\hat{R}_{max}$  (e.g. Athanassoula, 2008; Romeo et al., 2023), but this result has been extended by Christodoulou et al. (1995) for purely gaseous disc and sometimes cited as Mo et al.’s (1998) criterion, because the latter proposed a revised version of ELN82’s criterion in their work. Nevertheless, in order to make a comparison with OP73’s criterion, we use the parameter  $t^*$  as it was originally formulated (Equation 2.17).

## 2.3 Comparison between $t_{OP}$ and $t^*$

The pursuit of a new global stability parameter has been going on since OP73 and ELN82’s works. The main difference between  $t_{OP}$  and  $t^*$  is given by the different contribution of the gravitational energy which is considered in the  $t_{OP}$  and  $t^*$  ratios (Equations 2.7 and 2.17). Both  $t_{OP}$  and  $t^*$ , even though in different forms, used the gravitational energy related to the disc-halo system.

Now, while OP73 considered a two-component system, given by the stellar disc and a non-rotating halo, ELN82 assumed the stellar disc inside an external fixed potential - namely, the halo. Though these two assumptions seem barely different, they are actually the same thing. In fact, recalling Poisson's equation (1.5), the external potential can be seen as a second component with potential  $\Phi_{\text{ext}}(\mathbf{x})$  and density  $\rho_{\text{ext}}(\mathbf{x})$ . For this reason, even in ELN82 we may write the virial theorem for the whole disc-halo system as in OP73's Equation (2.1). We should note that not only ELN82's virial theorem of the total system has the same form of Equation (2.1), but also it *is* Equation (2.1).

It should be stressed the different nature of the  $t_{OP}$  and  $t^*$  parameters: the former is related to the virial theorem of the *whole* system (disc *and* halo), the latter to the virial theorem of the disc *subsystem*. For this reason, while in OP73 the self-gravity of the halo is considered (see Equation 2.5), in ELN82 it is not included in the computation of  $t^*$ . Given that ELN82 considered only the virial theorem of the disc component (see Equation 2.13), we consider  $\int f(\mathbf{x}, \mathbf{v}) d^3\mathbf{v} = \rho(\mathbf{x}) \equiv \rho_d(\mathbf{x})$  even though we are actually considering a two-components system (disc-halo).

Not only  $t_{OP}$  and  $t^*$  do differ because of the gravitational energy content: the ordered kinetic energy  $T$  is computed differently in OP73 and ELN82. However, if we consider a 2D steady rotating axisymmetric disc whose particles have  $z = 0$ ,  $v_R = 0$ ,  $v_z = 0$  and surface density  $\Sigma(R) \equiv \int \rho(R, z) dz$ , from Equation (2.12) we have

$$\begin{aligned} \langle v_\varphi(R) \rangle_{ELN} &= \frac{\int f(R, v_\varphi) v_\varphi dv_\varphi}{\int f(R, v_\varphi) dv_\varphi} = \\ &= \frac{1}{\Sigma(R)} \int f(R, v_\varphi) v_\varphi dv_\varphi = \langle v_\varphi(R) \rangle_{OP}. \end{aligned} \quad (2.24)$$

Thus  $T \equiv T_d$  has exactly the same expression in both OP73 and ELN82's formulations (Equations 2.1 and 2.13), namely

$$T = \frac{1}{2} \int \langle v_\varphi(R) \rangle^2 \Sigma(R) dR, \quad (2.25)$$

and the global stability parameters differ only from the contribution of the gravitational potential energy.

For the case of a rotating razor-thin disc, recalling Equation (2.15) and  $f_{\text{ext}} = W_{dh}/W_d$ , it is useful reformulate  $t^*$  (see Equation 2.14) as

$$t^* = \frac{T_d}{(1 + f_{\text{ext}})^2 |W_d|} = \frac{T_d W_d^2}{(W_d + W_{dh})^2 |W_d|} = \frac{T_d}{|W_D|} \frac{|W_d|}{|W_D|}, \quad (2.26)$$

where  $W_D = W_d + W_{dh}$  is the sum of the gravitational self-energy of the disc and the interaction energy with the external halo potential. From Equation (2.26) we can interpret  $t^*$  as the ratio between the kinetic energy of rotation of disc particles  $T_d$  and the total disc gravitational energy  $W_D$  times the fraction  $1/(1 + f_{\text{ext}})$  of the energy of the disc due to its self-potential. At this point, since  $T_d$  is common in both  $t_{OP}$  and  $t^*$ , we can relate the two parameters:

$$t^* = t_{OP} \frac{|W|}{|W_D|} \frac{|W_d|}{|W_D|} \quad (2.27)$$

Note that in case of a two-dimensional steady rotating disc with no external halo (namely, a one-component system), we also have  $W_d \equiv W_D$  and  $t_{OP} = t^*$ .

## 2.4 Universal validity of the $t_{OP}$ and $t^*$ parameters: a still open discussion

As we have already seen in Section 2.2, ELN82 argued that using  $t_{OP}$  as a global stability parameter has some disadvantages because of its construction. In fact,  $t_{OP}$  does not consider that the bar-like modes also depends weakly on the thickness of the disc. For this reason, ELN82 revised the definition of streaming velocity  $\langle \mathbf{v}(R) \rangle$  (Equation 2.12), including the integration of the velocity along the  $z$ -axis. Taking apart this second-order note, a main issue of  $t_{OP}$  is linked to the presence of  $W_h$  in the  $t_{OP}$  ratio (Equation 2.7): in fact, if the halo mass is dominant with respect to the disc mass,  $W_h \gg W_d$  and thus  $t_{OP}$  lowers because of the strong value of  $W_h$ . Although it seems correct, because from both analytical (OP73) and numerical (Hohl, 1971; Bodenheimer and Ostriker, 1973) perspectives the presence of a massive halo stabilize the disc globally, there are some cases in which the presence of  $W_h$  lowers the  $t_{OP}$  ratio but does not prevent global instability. This issue was argued by ELN82, who have found that  $t_{OP}$  states stability in disc-halo system where the halo has small mass and is very concentrated at the centre of the disc or it is massive but diluted in space, giving no practical support to prevent bar formation in the stellar disc. The former counterexample is also explored in Chapter 4, and we anticipate that the results are in agreement with ELN82's sentence.

Nevertheless, choosing  $t^*$  as global stability parameter has some disadvantages too.  $t^*$  is not sensitive enough to distinguish a bar pattern from spirals: this is why ELN82 introduced the bar length measurement  $L_b$ . Besides, the  $t^*$  ratio does not consider the velocity dispersion content of the disc particles in the inner regions of the disc, which can stabilize the disc (Athanasoula and Sellwood, 1986; Athanasoula, 2008). Linear stability work from Toomre (1981) and Evans and Read (1998), and numerical simulations from Sellwood (1989); Sellwood and Moore (1999) showed that a bar instability in stellar discs can be avoided not only with a massive external dark matter halo, but also with a minimal halo with a steep inner rise of the rotation curve of the disc particles.

The Efstathiou, Lake and Negroponte's (1982) criterion was extended by subsequent works of Christodoulou et al. (1995) for gaseous discs and rearranged by Mo et al. (1998) in a criterion which involves the halo spin parameter  $\lambda$ , the disc-to-halo specific angular momentum ratio  $j_d/j_h$  and the disc-to-halo mass ratio  $M_d/M_h$ :

$$\mathcal{E} = \lambda \frac{j_d/j_h}{M_d/M_h} \lesssim 1. \quad (2.28)$$

Although Equation (2.28) seems different from the original definition of  $t^*$  (Equation 2.17), in literature the two criteria behave similarly (e.g., Romeo et al., 2023). In any way, the correctness of ELN82's parameter is still debated. Recently, Izquierdo-Villalba et al. (2022) test the performance of  $t^*$  on the IllustrisTNG cosmological simulations (Rosas-Guevara et al., 2020, 2022) and stated that  $t^*$  can strongly predict the stability of many disc galaxies. On the other hand, Ghosh et al. (2023) found that in thick disc models  $t_{OP}$  predicts the bar instability better than  $t^*$ . From an observational point of view, Romeo et al. (2023) made a test of  $t^*$  and found out that the ELN82's criterion fails to distinguish barred from non-barred galaxies for about 55% of the cases.

The conundrum around  $t_{OP}$  and  $t^*$  is still open and vivid. From our perspective, we study the behaviour of  $t_{OP}$  and  $t^*$  in some idealized disc-halo scenarios, which we

discuss deeply in Chapters 3 and 4.

## 2.5 A new experimental global stability parameter

From both theoretical and numerical points of view, we have seen that both  $t_{OP}$  and  $t^*$  are not recognised universally valid as global stability parameters (e.g., Ghosh et al., 2023; Romeo et al., 2023). For this reason, the pursuit of a complete global stability parameter is still ongoing (see, e.g., Kataria et al., 2020).

Together with  $t_{OP}$  and  $t^*$  (Equations 2.7 and 2.17), in this work we present and study a global stability parameter which is slightly different from  $t^*$ . We start from the virial theorem of a disc embedded in an external potential (Equation 2.13), as ELN82 do in their work. We define:

$$\begin{aligned} t_W &= \frac{T_d}{\left| \int \rho_d(\mathbf{x}) \langle \mathbf{x}, \nabla(\Phi_d(\mathbf{x}) + \Phi_h(\mathbf{x})) \rangle d^3\mathbf{x} \right|} = \\ &= \frac{T_d}{|W_d + W_{dh}|} = \frac{T_d}{|W_D|} \end{aligned} \quad (2.29)$$

and

$$u_W = \frac{\Pi_d}{2|W_D|}, \quad (2.30)$$

where  $T_d$  and  $\Pi_d$  are computed following the definition of ELN82's mean circular velocity  $\langle v_\varphi(R) \rangle_{ELN}$  in Equation (2.12).  $t_W$  is strictly connected to  $t^*$ : in fact, if we write  $W_D = (1 + f_{ext})W_d$ , we have

$$t^* = \frac{t_W}{1 + f_{ext}}. \quad (2.31)$$

The close link between these two parameters will be investigated in Section 4.5.

We can rewrite the virial theorem of the disc (Equation 2.13) as function of  $t_W$  and  $u_W$ , such that

$$t_W + u_W = \frac{1}{2} \quad \Rightarrow \quad 0 \leq t_W \leq \frac{1}{2}. \quad (2.32)$$

One straightforward property of  $t_W$  from Equation (2.32) is that if the disc has no random motions, namely  $\Pi_d = 0$ , we always have  $t_W = 1/2$ , independently of the structure of  $T_d$  or  $W_D$ . The same result can be applied to  $u_W$  in case there are no ordered motions ( $T_d = 0$ ), namely  $u_W = 1/2$  always, with no other assumptions on the velocity distribution of the disc particles.

The main focus of  $t_W$  is on the gravitational energy content of the disc  $W_D$ , which is strictly related to the work done on disc particles by the self-gravity of the disc and the external halo potential. In case of a razor-thin steady rotating disc,  $T_d$  is the same for both  $t_{OP}$  and  $t^*$  – see Section 2.3, Equation (2.24) – thus  $t_W$  can be also connected with  $t_{OP}$  and  $t^*$  as

$$t_W = t^* \frac{|W_D|}{|W_d|} = t_{OP} \frac{|W|}{|W_D|}. \quad (2.33)$$

Since  $|W_D| \geq |W_d|$  and  $|W| \geq |W_D|$ , from Equation (2.33), in this specific case it is possible to obtain a hierarchy related to these three parameters:

$$t^* \leq t_W, \quad (2.34)$$

$$\text{and } t_{OP} \leq t_W. \quad (2.35)$$

In a razor-thin disc-only system,  $t^* = t_{OP} = t_W$  because  $W = W_D = W_d$ .

# Chapter 3

## Set up of the $N$ -body simulations

After having understood the motivations that led Ostriker and Peebles (1973) and Efstathiou, Lake, and Negroponte (1982) to introduce the parameters  $t_{OP}$  and  $t^*$ , respectively, we investigate their functioning through a set of  $N$ -body simulations. In this Chapter, we first set the initial conditions of the system, which consist of a stellar disc and a dark matter halo. In our simulation suite, we use an exponential razor-thin disc, described in Section 3.1.2, and a Hernquist (1990) profile, reported in Section 3.1.1, to represent the dark matter halo. The latter is treated as an external potential in our simulations, thus the dark matter halo is not capable of evolving at subsequent times, unlike the stellar disc. In this Chapter, we also present a test of the initial conditions for the disc-halo system, to verify the correctness of the initial conditions before running the  $N$ -body simulations, and the settings of the input parameters for the  $N$ -body code (FVFPS Londrillo et al., 2003).

### 3.1 Galaxy models

To investigate the behaviour of the  $t_{OP}$ ,  $t^*$  and  $t_W$  parameters in disc-halo systems (Equations 2.7, 2.17 and 2.29), we set the initial conditions through some simple analytical models. The halo, which we assume to be rigid and non-rotating, is modelled by a Hernquist profile (see Section 3.1.1) and acts on the disc component as a spherically symmetric external potential. We put an axisymmetric razor-thin disc within the halo potential, which we initialize via an exponential surface density profile (see Section 3.1.2), which is a good fit for the observed galactic disc profiles (see, e.g., Cimatti et al., 2019). Since our goal in the initial conditions is making all the disc particles rotating in circular orbits with corresponding circular speed  $v_c(R)$  (Equation 1.16), in the following Subsections there is a particular focus on the circular speed  $v_c(R)$  of the disc particles, given by the disc itself and – if present – the halo. Furthermore, choosing analytical models allows us to compute in a semi-analytical way the aforementioned global stability parameters  $t_{OP}$  and  $t^*$ .

#### 3.1.1 The Hernquist profile

The Hernquist (1990) profile is a family of density profiles that is frequently adopted to model the stellar component in galaxy bulges and in early-type galaxies, but it is also used to characterize the dark matter profiles together with the NFW (Navarro et al., 1997) models (see van de Ven et al., 2009).

The Hernquist (1990) is a spherically symmetric system with density profile

$$\rho(r) = \frac{M a}{2\pi r} \frac{1}{(r+a)^3}, \quad (3.1)$$

where  $r$  is the spherical radius,  $M$  is the total mass and  $a$  is a scale length. The integration of Equation (3.1) in spherical symmetry gives the cumulative mass distribution:

$$M(r) = M \frac{r^2}{(r+a)^2}. \quad (3.2)$$

By definition, independently of the mass distribution, the half-mass radius  $r_h$  satisfies

$$M(r_h) = \frac{M}{2}, \quad (3.3)$$

which, for the Hernquist (1990) model, implies

$$\frac{M}{2} = M \frac{r_h^2}{(r_h+a)^2} \quad \Rightarrow \quad r_h = (1 + \sqrt{2})a. \quad (3.4)$$

The Hernquist (1990) potential  $\Phi(r)$  that satisfies Poisson's equation (1.5), with  $\rho(r)$  given by Equation (3.1), is

$$\Phi(r) = -\frac{GM}{r+a}. \quad (3.5)$$

If we take into account a non-rotating spherical system, the radial velocity dispersion  $\sigma_r^2(r)$  is given by the Jeans equation

$$\frac{1}{\rho} \frac{d(\rho\sigma_r^2)}{dr} + 2\beta \frac{\sigma_r^2}{r} = -\frac{d\Phi}{dr}, \quad (3.6)$$

where  $\beta(r) = 1 - \sigma_\theta^2/\sigma_r^2$ ,  $\sigma_r^2$  is the radial velocity dispersion and  $\sigma_\theta^2 = \sigma_\varphi^2$  are the angular velocity dispersions. In an isotropic system we have

$$\sigma_r^2 = \sigma_\varphi^2 = \sigma_\theta^2. \quad (3.7)$$

Thus  $\beta(r) = 0$  and in Equation (3.6) the second term with  $\beta$  vanishes. The integration of Equation (3.6) with vanishing  $\beta(r)$ , density and potential profiles described by Equations (3.1) and (3.5), respectively, gives

$$\sigma_r^2(r) = \frac{GM}{12a} \left\{ \frac{12r(r+a)^3}{a^4} \ln\left(\frac{r+a}{r}\right) - \frac{r}{r+a} \left[ 25 - 52\frac{r}{a} + 42\left(\frac{r}{a}\right)^2 + 12\left(\frac{r}{a}\right)^3 \right] \right\}. \quad (3.8)$$

Note that  $\sigma_r^2$  is nowhere divergent and vanishes as  $r/a \rightarrow 0$  and  $\sigma_r^2 \sim GM/5r$  as  $r \gg a$ . If all the particles of the Hernquist (1990) sphere are moving in circular orbits,  $\sigma_r^2 = 0$ ,  $2\sigma_\theta^2 = r \, d\Phi/dr$  and  $\sigma_\theta^2 + \sigma_\varphi^2 = v_c^2$ , where  $v_c$  is the circular velocity (Equation 1.16). Instead, for pure radial orbits we have  $\sigma_\theta^2 = \sigma_\varphi^2 = 0$ . In a spherical isotropic model, the kinetic energy is

$$K(r) = 6\pi \int_0^r \rho(r) \sigma_r^2(r) r^2 \, dr. \quad (3.9)$$

Substituting Equations (3.1) and (3.8), we get

$$K(r) = \frac{GM^2}{4a} \left[ 4\left(\frac{r}{a}\right)^3 \ln\left(\frac{r+a}{r}\right) - 4\left(\frac{r}{a}\right)^2 + 2\frac{r}{a} - 1 + \frac{(r/a)^2 + r/a + 1}{(1+r/a)^3} \right]. \quad (3.10)$$

As  $r/a \rightarrow 0$ , we have

$$K(r) \sim \frac{GM^2}{a} \left(\frac{r}{a}\right) \ln\left(\frac{a}{r}\right), \quad (3.11)$$

and the total kinetic energy, which is obtained in the limit  $r \rightarrow \infty$  is

$$K_{\text{tot}} = \frac{GM^2}{12a}. \quad (3.12)$$

By the definition of total gravitational energy

$$W_{\text{tot}} = 2\pi \int_0^\infty \rho(r) \Phi(r) r^2 \, dr \quad (3.13)$$

we can achieve the related expression for the Hernquist (1990) profile, namely

$$W = -\frac{GM^2}{6a}. \quad (3.14)$$

Note that Equations (3.12) and (3.14) satisfy the scalar virial theorem  $2K + W = 0$ .

The local escape velocity  $v_e(r)$  and the circular speed  $v_c(r)$  are given by Equations (1.17) and (1.16), respectively. For the Hernquist (1990) profile, we have

$$v_e(r) = \sqrt{\frac{2GM}{r+a}} \quad (3.15)$$

and

$$v_c(r) = \frac{\sqrt{GM}r}{r+a}. \quad (3.16)$$

Note that as  $r/a \rightarrow +\infty$ ,  $v_c \sim r^{-1/2}$ , so the circular speed curve is asymptotically Keplerian.

### 3.1.2 The exponential disc

Both the surface brightness and the surface mass density distribution of many galactic discs, seen face on, can be approximately modelled in an exponential form (de Vaucouleurs, 1959; Freeman, 1970; Smith et al., 2015). In the assumption of a razor-thin (i.e. zero-thickness) axisymmetric disc, whose particles are all lying on a plane (say  $z = 0$  in cylindrical coordinates  $R, \varphi, z$ ), the radial surface brightness  $I(R)$  and the surface density profile  $\Sigma(R)$  are

$$I(R) = I_0 \exp\left(-\frac{R}{R_d}\right) \quad (3.17)$$

$$\text{and } \Sigma(R) = \Sigma_0 \exp(-R/R_d), \quad \text{respectively,} \quad (3.18)$$

where  $I_0$  and  $\Sigma_0$  are the central ( $R = 0$ ) values of  $I(R)$  and  $\Sigma(R)$ , and  $R_d$  is the disc scale length.

Using the razor-thin disc decomposition into homoeoids (see Section 1.1.2), we can find the family of homeoids such that the combination of their surface mass densities equals (3.18) at every  $R$ . For the razor-thin exponential disc case, the potential in the equatorial plane  $z = 0$ , obtained by substituting its surface mass density (3.18) into Equation (1.24), is

$$\Phi(R, 0) = -4G\Sigma_0 \int_0^R da \frac{aK_1(a/R_d)}{\sqrt{R^2 - a^2}} = -\pi G\Sigma_0 R [I_0(y)K_1(y) - I_1(y)K_0(y)], \quad (3.19)$$

where  $I_n$  and  $K_n$  are modified Bessel functions (see Binney and Tremaine, 2008, Appendix C.7) and  $y = R/(2R_d)$ .

Freeman (1970) has found the expression for the circular speed of an exponential disc by differentiating Equation (3.19) with respect to  $R$ :

$$v_c^2(R) = R \left( \frac{\partial \Phi}{\partial R} \right)_{z=0} = 4\pi G\Sigma_0 R_d y^2 [I_0(y)K_0(y) - I_1(y)K_1(y)], \quad (3.20)$$

whose peak is at  $R_{\text{peak}} \approx 2.15R_d$  (see Cimatti et al., 2019; Bovy, 2023).

The integration of the surface mass density of the exponential disc in cylindrical coordinates gives its mass interior to  $R$ :

$$\begin{aligned} M(R) &= 2\pi \int_0^R dR' R' \Sigma_0 \exp(-R'/R_d) \\ &= 2\pi \Sigma_0 R_d^2 \left[ 1 - \exp(-R/R_d) \left( 1 + \frac{R}{R_d} \right) \right]. \end{aligned} \quad (3.21)$$

For  $R \rightarrow \infty$  we obtain the total mass

$$M = 2\pi \Sigma_0 R_d^2. \quad (3.22)$$

Using the definition of the half-mass radius (Equation 3.4) with the exponential mass profile (Equation 3.21), for this model we have  $R_h = 1.68R_d$  (e.g. Cimatti et al., 2019).

If we divide Equation (3.21) by the total mass (Equation 3.22), we get the normalized mass profile for the razor-thin exponential disc:

$$F(R) = 1 - \exp(-R/R_d) \left( 1 + \frac{R}{R_d} \right). \quad (3.23)$$

## 3.2 Initial conditions

We now describe the method we adopt to generate the initial conditions of our simulations. The main goal is to sample an axisymmetric razor-thin disc of total mass  $M_d$  through a set of  $N$  particles, all with the same mass  $m = M_d/N$ . The velocity of all the disc particles is set such that the azimuthal speed is equal to the circular speed (Equation 1.16) at every radius  $R$  ( $v_\varphi(R) = v_c(R) \equiv R \partial\Phi_d/\partial R$ ) and the radial speed  $v_R(R) = 0$ . In other words, every particle initially moves in circular motion with speed in balance with the potential of the whole disc. The azimuthal velocities are first assigned so that the direction of the angular momentum is the same for all particles.

Furthermore, the initial conditions might also include a dark matter halo, which we model here as an external fixed potential. Treating the dark matter halo as a fixed potential is, of course, an approximation: by doing that, we assume the halo is 'dead' (or 'unresponsive'), which means that the halo particles do not change their properties in the phase space due to the disc potential (or, similarly, the disc potential has negligible impact in the distribution function of the halo) and respond only to their gravitational field. On the other hand, the disc particles might gravitate within an external potential, which means that not only they respond to their own potential, but also to the external halo potential. This means, considering that in our initial conditions the initial velocity is related to the circular speed, that the initial velocity of each particle will also change due to the possible presence of the halo.

As a final step about generating the initial conditions, a fraction  $\alpha$  (with  $0 \leq \alpha \leq 1/2$ ) of the disc particles is randomly selected such that the sign of their azimuthal velocity is reversed. By inverting the direction of a fraction  $\alpha$  of initial velocity, we are able to introduce an azimuthal velocity dispersion without affecting (or summoning) the radial component.

### 3.2.1 Input parameters

For our simulations, the stellar disc is modelled with an exponential surface density profile (see Section 3.1.2). The dark matter halo is represented by the Hernquist (1990) model (see Section 3.1.1).

To generate a certain dataset which samples the disc model we want to adopt, we need to quantify some parameters at the beginning of the generation code: the total number of disc particles  $N$ , the disc model, the total disc mass  $M_d$ , the disc scale length  $R_d$ , the disc size (or truncation radius)  $R_{d,max}$ , the halo-to-disc mass ratio  $M_h/M_d$ , the halo-to-disc scale length ratio  $a_h/R_d$ .

All these parameters allow us to compute uniquely:

- for the disc: the cumulative mass distribution of the disc  $F(R)$  (Equation 3.23), the surface density profile of the disc (Equation 3.18), the potential  $\Phi_d(R, 0)$  of the disc particles (Equation 3.19) and their circular speed  $v_c(R)$  (Equation 3.20);
- for the halo: the gravitational potential of the halo  $\Phi_h(r)$  (Equation 3.5) and the circular speed  $v_c(R)$  related to the potential itself (Equation 3.16).

### 3.2.2 Disc: position and velocity assignment

Once we set the input parameters, we can sample the disc model through  $N$  particles, all with mass  $m = M_d/N$ . For the initial conditions, we need to assign a position

$\mathbf{x}$  and a velocity  $\mathbf{v}$  to each particle. Positions are given by the normalized disc mass distribution  $F(R)$ , while the velocity assignment, for our purpose, is given by the potential of the whole system

$$\Phi(R, z) = \Phi_d(R, z) + \Phi_h(R, z) \quad \forall(R, z), \quad (3.24)$$

where the subscripts  $d$  and  $h$  refer to the disc and the external halo, respectively. Thus the circular speed of each particle at position  $R$  is

$$v_c^2(R) = R \left( \frac{\partial \Phi}{\partial R} \right)_{z=0} = R \left( \frac{\partial \Phi_d}{\partial R} \right)_{z=0} + R \left( \frac{\partial \Phi_h}{\partial R} \right)_{z=0} = v_{c,d}^2(R) + v_{c,h}^2(R). \quad (3.25)$$

We report here a scheme of the main steps implemented in the generation of the initial conditions for the disc-halo system:

1. Choose a random value of  $\tilde{F}(R)$  from a uniform distribution  $[0, 1]$ ;
2. Find the related  $R$  using the inverse function of  $\tilde{F}(R)$ , such that  $0 \leq R \leq R_{d,max}$ ;
3. Compute the potentials  $\Phi_d(R)$  and  $\Phi_h(R)$  and the circular speed  $v_c(R)$  (Equation 3.25) at a given  $R$ ;
4. Choose a random value of the phase  $\varphi$  from a uniform distribution  $[0, 1]$  and multiply it by  $2\pi$ ;
5. Decompose the position  $R$  and the circular speed  $v_c(R)$  along the  $x$  and  $y$  directions using Equations (C.1) and (C.8) from Appendix C, respectively. Because we impose the motion on the  $(x, y)$  plane,  $z = 0$  and  $v_z = 0$  for all the particles.

The aforementioned steps are done cyclically for  $N$  times, in order to set the IC for all the particles of the system.

It should be noted that Step 2 cannot always be solved analytically, thus a numerical approach is needed. Since there is no analytical expression of the inverse function of Equation (3.27) (or, equivalently, Equation 3.23),  $R$  is solved at a given  $\tilde{F}(R)$  using a root-finding algorithm, such as the bisection method (see, e.g., Hoffman and Frankel, 2018), within the interval  $[0, R_{d,max}]$ .

Furthermore, Steps 3 and 5 ensure that all the particles have only initial tangential motion, namely  $v_R(R) = 0$  and  $v_\phi(R) = v_c(R)$  at every  $R$  – see Section 3.3 for further details.

These steps are also valid in the case of a disc-only system, namely  $\Phi(R) \equiv \Phi_d(R)$  and thus  $\Phi_h(R) = 0$ .

### Effects of the truncation radius $R_{d,max}$ on disc equations

Section 3.1.2 describes a razor-thin disc whose mass distribution is radially extended over all the interval  $[0, \infty)$ . In  $N$ -body implementations, such as ours or in other works (e.g., Smith et al., 2015), stellar discs models are imposed to be truncated, thus we need to set a truncation radius  $R_{d,max}$ .

The presence of  $R_{d,max}$  sets a finite region for the mass density distribution of the disc, thus changing the respective mathematical forms of the mass distribution. Now,

focusing on this effect for the case of a razor-thin exponential disc (Section 3.1.2), we impose that the total mass of a finite disc with size  $R_{d,max}$  is

$$\begin{aligned}\tilde{M}_d &= 2\pi \int_0^{R_{d,max}} dR' R' \Sigma_0 \exp(-R'/R_d) = \\ &= 2\pi \Sigma_0 R_d^2 \left[ 1 - \exp(-R_{d,max}/R_d) \left( 1 + \frac{R_{d,max}}{R_d} \right) \right].\end{aligned}\quad (3.26)$$

Now, if we normalize Equation (3.21) with  $\tilde{M}(R)$ , we obtain

$$\tilde{F}(R) = \frac{M(R)}{\tilde{M}_d} = \frac{1 - \exp(-R/R_d) \left( 1 + \frac{R}{R_d} \right)}{1 - \exp(-R_{d,max}/R_d) \left( 1 + \frac{R_{d,max}}{R_d} \right)} = qF(R) \quad \forall R \in [0, R_{d,max}].\quad (3.27)$$

Note that  $\tilde{F}(R)$  and  $F(R)$  are related through the normalization factor  $q$ , thus the functional dependences are the same as in Equation (3.23) and  $0 \leq \tilde{F}(R) \leq 1$  for  $0 \leq R \leq R_{d,max}$ . We can quantify the difference between  $\tilde{F}(R)$  and  $F(R)$  using the relative error

$$\frac{|\tilde{F}(R) - F(R)|}{F(R)} = q - 1 \quad \forall R \in [0, R_{d,max}].\quad (3.28)$$

Assuming  $R_d$  and  $R_{d,max}$  are fixed, the relative error is constant at every  $R$  and propagates over all the equations of Section 3.1.2 because of the changed value of  $\Sigma_0$ . Nevertheless, by setting  $R_{d,max}/R_d = 10$ , the relative error  $q - 1 \simeq 0.05\%$ , which tells us that the finite size  $R_{d,max}/R_d = 10$  affects the value of  $\Sigma_0$  for a factor of 0.05%, which we consider negligible for the scope of our work. This means we can use all the equations of Section 3.1.2, even though they are exact only for an untruncated disc, neglecting the difference between  $\tilde{F}(R)$  and  $F(R)$ .

### 3.3 Testing the initial conditions

Before starting the simulations, we need to verify whether the initial conditions are properly set.

First of all, we check the initial conditions for the disc. All the input parameters related to the disc are fixed for every simulation run – see Table 3.1 for more details.

$N$	Model	$M_d/M_u$	$R_d/l_u$	$R_{d,max}/R_d$
102400	Exp.	1	1	10

Table 3.1: Input parameters related to the disc, which are adopted for every simulation run. For the code units  $M_u$  and  $l_u$ , see Section 3.4.1, ”Code units”.

If we plot the spatial distribution of the disc particles on the  $(x, y)$ ,  $(x, z)$  and  $(y, z)$  planes (Figure 3.1), we can see all particles lying in the  $z = 0$  plane. We stress that Figure 3.1 is valid not only for disc-only  $N$ -body simulations, but also for disc-halo system. In fact, the initial mass distribution of the disc is not linked to the halo properties.

For the same reason, the initial plot of the surface density (Figure 3.2) of the disc is valid for the conditions expressed in Table 3.1, independently of the presence of

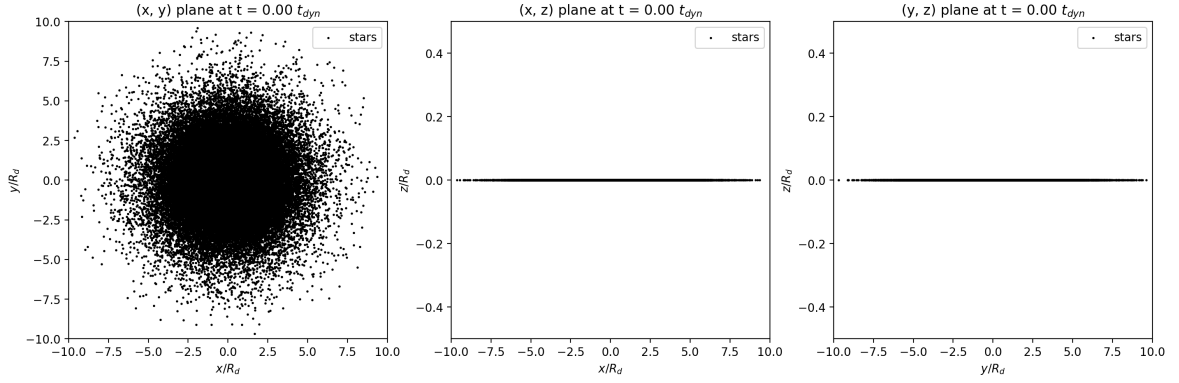


Figure 3.1: Initial spatial distribution of the disc particles on the  $(x, y)$ ,  $(x, z)$  and  $(y, z)$  planes for the case of a razor-thin exponential disc with the conditions expressed in Table 3.1.  $x$ ,  $y$  and  $z$  are normalized to  $R_d$ .

the halo. Comparing the numerical the surface density of the disc (black line) to the analytical one for an untruncated disc (red line), we can see that the numerical sample represents well the analytical profile, as expected.

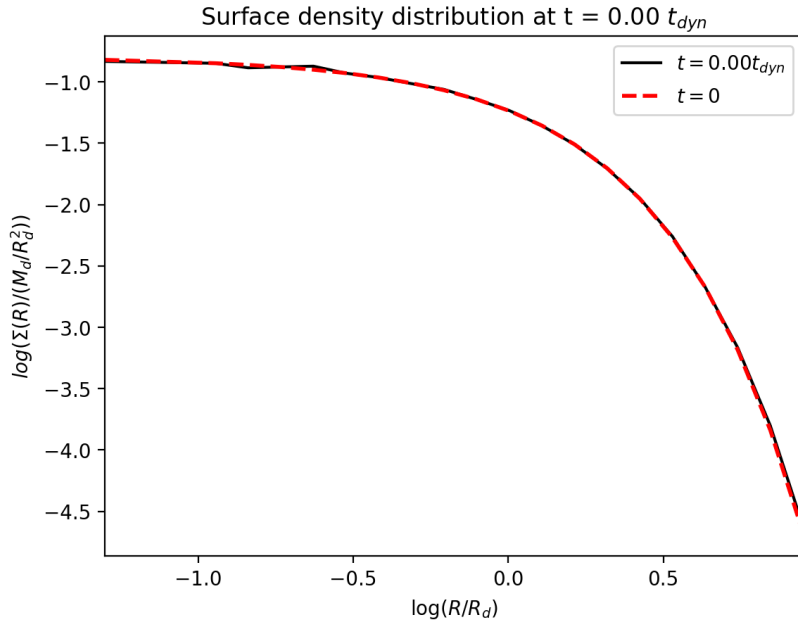


Figure 3.2: At  $t = 0$ , surface density profile distribution of the disc for the case of a razor-thin exponential disc with the conditions expressed in Table 3.1 (black line), compared to the analytical profile in Equation (3.18) (red line).  $R$  and  $\Sigma(R)$  are normalized to  $R_d$  and  $M_d/R_d^2$ , respectively.

Furthermore, we can put in the same plot the normalized mass profile of an untruncated disc (Equation 3.23) and the  $\tilde{F}(R)$  given by the truncated disc with the input parameters described in Table 3.1. The results we see in Figure 3.3 is the two profiles are superposed. This fact allows us to say that the disc implementation of the mass distribution is done properly.

Figure 3.4 displays the potential profile of the disc particles.

We now look at the velocity components  $v_R$  and  $v_\varphi$  generated numerically for each

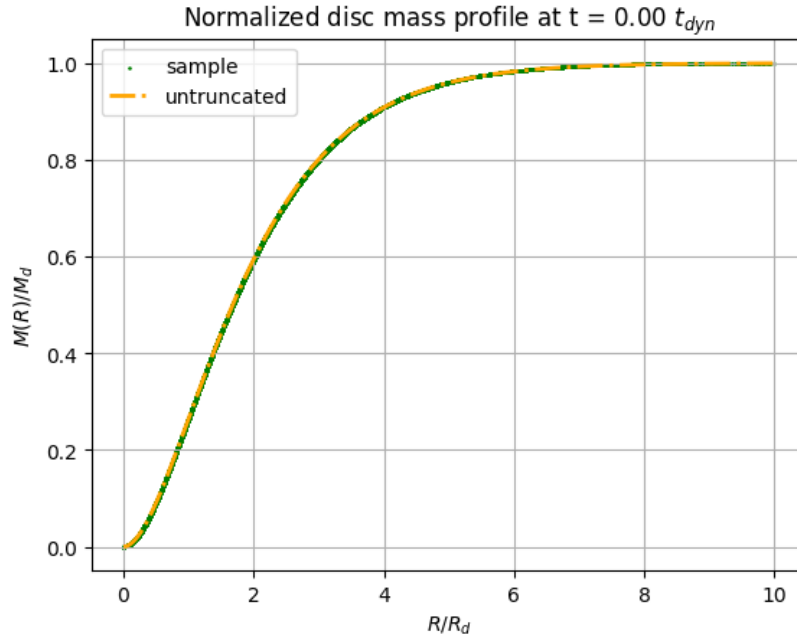


Figure 3.3: At  $t = 0$ , normalized mass profile of the disc with the conditions expressed in Table 3.1 (solid green line), compared to the analytical profile in Equation (3.23) for an untruncated disc (dashed orange line).  $R$  and  $M(R)$  are normalized to  $R_d$  and  $M_d$ , respectively.

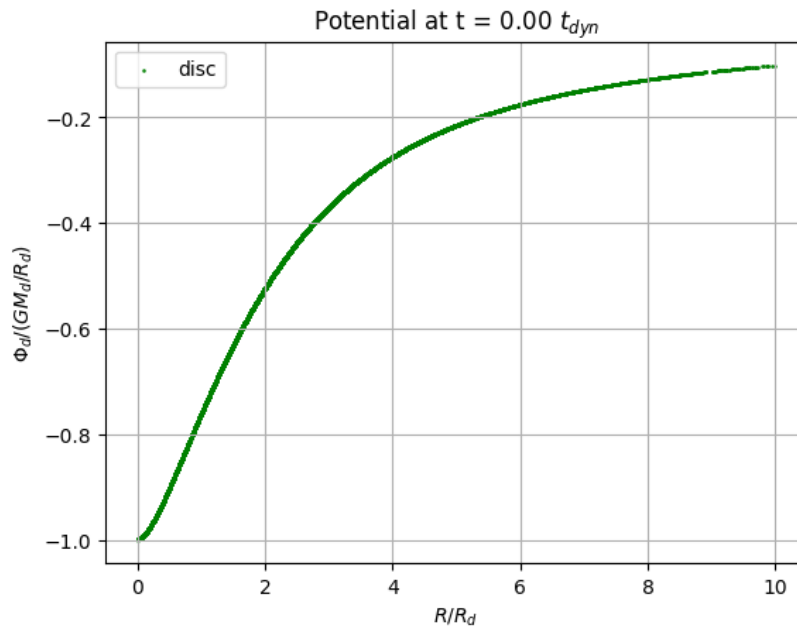


Figure 3.4: At  $t = 0$ , potential of the disc particles with the conditions expressed in Table 3.1.  $R$  and  $\Phi_d(R)$  are normalized to  $R_d$  and  $GM_d/R_d$ , respectively.

particle. Now, because in our implementation all the particles move in circular orbits such that  $|v_\varphi(R)| = v_c(R) \equiv R \partial\Phi/\partial R$  for  $R \in [0, R_{d,max}]$ ,  $v_\varphi$  is function to the *total* potential of the system, which means the speed curve will vary as the halo potential does. For this reason, we report here in Figure 3.5 an example of speed curve of the disc particles in a disc-halo system, compared to the curve of a disc-only system. As

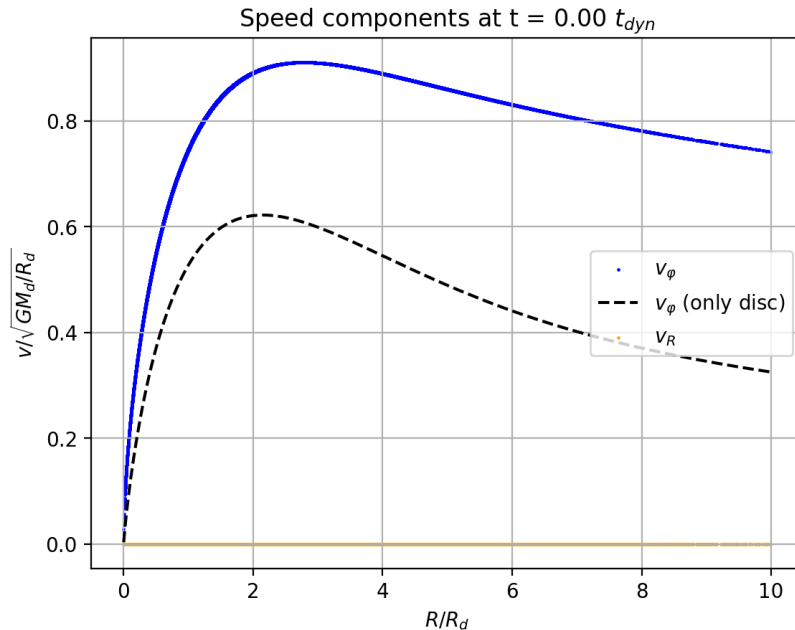


Figure 3.5: At  $t = 0$ , azimuthal speed curve of the disc for the case of a razor-thin exponential disc with the conditions expressed in Table 3.1 (dashed line), compared to the initial azimuthal (blue) and radial (orange) speed curve of the same disc within a halo potential with  $M_h/M_d = 10$  and  $a_h/R_d = 5$ .  $R$  and the  $\mathbf{v}$ -components are normalized to  $R_d$  and  $(GM_d/R_d^2)^{1/2}$ , respectively.

we expect, in Figure 3.5 all the disc particles have non-zero azimuthal velocity (blue line), while the radial velocity (orange line) is null. If the halo is not present in the simulation run (namely  $M_h/M_d = 0$ ), then the azimuthal velocity curve is given by Equation (3.20), which is represented by a dashed black line in Figure 3.5.

## 3.4 Set up of the $N$ -body simulations

Once generated the initial conditions for the disc-halo system, we need to import them in the  $N$ -body code FVFPS, a Fortran Version of a Fast Poisson Solver, which is a momentum-preserving fast Poisson solver for  $N$ -body systems that was developed by Dehnen (2002) in the C++ code falCON, Force Algorithm with Complexity  $O(N)$ , and then implemented by Londrillo et al. 2003 in a Fortran-90 code. In order to run the  $N$ -body simulations, we need to specify some input parameters for the  $N$ -body code runs. In Section 3.4.1 we report the most important ones related to the functioning of the FVFPS code.

### 3.4.1 Set up parameters

**Dynamical time  $t_{dyn}$ , initial time step  $\Delta t_{in}$  and end time  $t_{max}$**

Following the convention used by ELN82 (see Section 2.2.3), we take as reference dynamical time  $t_{dyn}$  for a disc (with or without dark matter halo) the orbital period of

a particle at the stellar half-mass radius  $R_h$  (Equation 3.4) which is given by:

$$t_{dyn} = \frac{2\pi R_h}{v_c(R_h)}, \quad (3.29)$$

where  $v_c(R_h)$  is the circular speed (Equation 3.25) at  $R_h$ . Note the dynamical time is influenced by the potentials of the disc *and* the halo at  $R_h$ , thus for a fixed disc potential  $\Phi_d$  – as in our case – we have that  $v_c(R_h)$  varies only if  $\Phi_h$  does.

The FVFPS code (Londrillo et al., 2003) adopts a leap-frog time integration scheme (see, e.g., Hockney and Eastwood, 1988; Bodenheimer, 2007) and uses an initial time step  $\Delta t_{in} = C t_{dyn}$ , where  $C$  is a user-provided parameter. The time step  $\Delta t$  is the same for all the particles and is adaptive, namely the code updates its value every  $n$  steps using

$$\Delta t = \min(\Delta t_{crit} \equiv 1/\sqrt{4\pi G \rho_{max}}, \Delta t_{in}), \quad (3.30)$$

where  $\rho_{max}$  is the maximum local density of the system. Equation (3.30) ensures the stability of the time integration method. Typically, Londrillo et al. (2003) suggest  $C \simeq 10^{-2}$  in numerical simulations such as galaxy mergers. In our case, also because of the choice of the reference dynamical time at the half-mass radius of the disc, we always set  $C = 10^{-3}$ , such that the starting time step is  $\Delta t_{in} = 10^{-3} t_{dyn}$ ; then we let the code update the time-step adaptively every 10 time integration cycles in case Condition (3.30) holds.

### Gravitational softening $\epsilon$

The FVFPS code (Londrillo et al., 2003) computes the gravitational acceleration of particles assuming they are not point masses, but have some size given by the softening length  $\epsilon$ . Considering that the force a  $N$ -body system exerts on a point mass  $m_j$  at position  $\mathbf{x}_j$  is

$$\mathbf{F}(\mathbf{x}_j) = m_j \sum_{i=1, i \neq j}^N G m_i \frac{\mathbf{x}_i - \mathbf{x}_j}{|\mathbf{x}_i - \mathbf{x}_j|^3}. \quad (3.31)$$

If we define  $r_{ij} \equiv |\mathbf{x}_i - \mathbf{x}_j|^3$  and introduce the softening length  $\epsilon$  in Equation (3.31), we have

$$\mathbf{F}(\mathbf{x}_j) = m_j \sum_{i=1, i \neq j}^N G m_i \frac{\mathbf{x}_i - \mathbf{x}_j}{(r_{ij}^2 + \epsilon^2)^{3/2}}. \quad (3.32)$$

Equation (3.32) ensures the computation of the gravitational force does not diverge when  $r_{ij} \rightarrow 0$ , which means we assign a finite size  $\epsilon$  to each particle.

The choice of  $\epsilon$  depends on the number of particles  $N$  involved in the simulation and on the density distribution – in our case,  $\Sigma_d(\mathbf{x})$  set by Equation (3.18). We can simply assume  $\epsilon \simeq \lambda$ , where  $\lambda$  is the mean interparticle distance. We can define  $\lambda$  in both spherical and disc systems by using the volume and the area within the half-mass radius, respectively, namely

$$\begin{aligned} V_{half} &= \frac{4}{3}\pi r_h^3 \quad \text{for a spherical system} \\ \text{and } A_{half} &= \pi R_h^2 \quad \text{for a disc,} \end{aligned} \quad (3.33)$$

where  $r_h$  and  $R_h$  are the spherical and cylindrical half-mass radius, respectively. If we build a system with  $N$  particles of the same mass, we have that the number of particles

within the half-mass radius is always  $N/2$ . Thus

$$\lambda = \begin{cases} \left(\frac{V_{half}}{N/2}\right)^{1/3} & \text{for a spherical system,} \\ \left(\frac{A_{half}}{N/2}\right)^{1/2} & \text{for a disc.} \end{cases} \quad (3.34)$$

Now, given a system with  $N$  particles and a half-mass radius  $r_h$  (for spheres) or  $R_h$  (for discs), by equating  $\epsilon \simeq \lambda$ , where  $\lambda$  is defined in Equation (3.34), we have

$$\epsilon = \begin{cases} \left(\frac{V_{half}}{N/2}\right)^{1/3} = \left(\frac{\frac{4}{3}\pi r_{half}^3}{N/2}\right)^{1/3} = \left(\frac{8}{3}\pi\right)^{1/3} \frac{r_{half}}{N^{1/3}} & \text{for a spherical system,} \\ \left(\frac{A_{half}}{N/2}\right)^{1/2} = \left(\frac{\pi R_{half}^2}{N/2}\right)^{1/2} = \sqrt{2\pi} \frac{R_{half}}{N^{1/2}} & \text{for a disc.} \end{cases} \quad (3.35)$$

In our case, the disc system is always sampled by  $N = 102400$  particles and has the properties reported in Table 3.1, with  $R_h = 1.68R_d$  (e.g. Cimatti et al., 2019). Thus the softening  $\epsilon$  has always the same value in our simulations:

$$\epsilon \simeq 0.013R_d. \quad (3.36)$$

### Opening angle $\theta_{min}$

Since the FVFPS (Londrillo et al., 2003) scheme is partially based on tree algorithms, originally proposed by Barnes and Hut (1986), we need to preassign an opening parameter  $\theta_{min}$  in order to set the opening criterium

$$\frac{s}{d} \leq \theta_{min}, \quad (3.37)$$

where  $s$  is the width of the region represented by the considered node and  $d$  is the distance between center-of-mass of the node and the particle with mass  $m_j$  on which we are computing the gravitational force. As in Dehnen's (2002) scheme implementation, FVFPS's opening parameter  $\theta$  is mass dependent, where the implicit form of the function  $\theta(M)$  is (Londrillo et al., 2003)

$$\frac{\theta^5}{(1-\theta)^2} = \frac{\theta_{min}^5}{(1-\theta_{min})^2} \left(\frac{M}{M_{tot}}\right)^{-1/3}, \quad (3.38)$$

where  $M$  is the mass enclosed in a cell. The mass dependence ensures the code has a fast performance and a more uniform error distribution (see Londrillo et al., 2003, Figure 1).

Common values of  $\theta_{min}$  are  $\theta_{min} = 0.4 \div 0.7$  (see, e.g., Aarseth, 2003; Springel, 2005). In our simulations, because of the geometry of the problem, we always set

$$\theta_{min} = 0.4. \quad (3.39)$$

### Code units

The FVFPS code (Londrillo et al., 2003) works with dimensionless quantities ( $m_i$ ,  $\mathbf{x}_i$ ,  $\mathbf{v}_i$ , which are related to the  $i$ -th particle, and  $t$  for the simulation run time) and assumes  $G = 1$ . For this reason, we need to write the initial conditions in dimensionless units, which means

$$m_i \rightarrow \frac{m_i}{M_u}; \quad \mathbf{x}_i \rightarrow \frac{\mathbf{x}_i}{l_u}; \quad \mathbf{v}_i \rightarrow \frac{\mathbf{v}_i}{v_u}; \quad t \rightarrow \frac{t}{t_u}, \quad (3.40)$$

where  $M_u$ ,  $l_u$ ,  $v_u$  and  $t_u$  are the code mass, length, speed and time units. In particular,  $v_u$  and  $t_u$  are functions of  $M_u$  and  $l_u$ , namely

$$v_u = \left( \frac{GM_u}{l_u} \right)^{1/2} \simeq 207.4 \left( \frac{M_u}{10^{10} M_\odot} \right)^{1/2} \left( \frac{l_u}{\text{kpc}} \right)^{-1/2} \text{ km/s} \quad (3.41)$$

$$\text{and } t_u = \frac{l_u}{v_u} \simeq 4.7 \times 10^6 \left( \frac{l_u}{\text{kpc}} \right)^{3/2} \left( \frac{M_u}{10^{10} M_\odot} \right)^{-1/2} \text{ yr.} \quad (3.42)$$

After the simulation run, we can rescale the quantities  $(m_i, \mathbf{x}_i, \mathbf{v}_i, t)$  as

$$m_i \rightarrow m_i M_u; \quad \mathbf{x}_i \rightarrow \mathbf{x}_i l_u; \quad \mathbf{v}_i \rightarrow \mathbf{v}_i v_u; \quad t \rightarrow t t_u. \quad (3.43)$$

For instance, choosing  $M_u = 10^{10} M_\odot$  and  $l_u = 1 \text{ kpc}$ , the total disc mass is  $M_d = 10^{10} M_\odot$  and the disc scale radius is  $R_d = 1 \text{ kpc}$ .

### Fraction of retrograde orbits $\alpha$

Before the simulation runs, we modify the initial conditions to account for the the fraction of retrograde orbits inside the disc, namely the fraction of particles which are orbiting in the opposite sense of the most part of the stars (see, e.g., Kalnajs, 1977; Pawlowski et al., 2011). We adopt the letter  $\alpha$  to describe this fraction, with the condition that

$$0 \leq \alpha \leq \frac{1}{2}, \quad (3.44)$$

because if  $\alpha > 1/2$ , the fraction of the retrograde stars represents the bulk motion of the stars in the disc, thus the fraction of prograde orbits can be seen as the fraction of counter-orbiting stars and we would just go back to the case expressed in Equation (3.44).

We choose randomly a fraction  $\alpha$  of orbits from the generated ones and invert the direction of the initial velocity, which in our case means

$$\begin{aligned} \mathbf{v}(R) &\equiv v_\varphi(R) \rightarrow -\mathbf{v}(R) \equiv -v_\varphi(R) \\ \Rightarrow v_x(R) &\rightarrow -v_x(R); \quad v_y(R) \rightarrow -v_y(R). \end{aligned} \quad (3.45)$$

The introduction of  $\alpha$  in our simulations changes the evaluation of the kinetic energy components  $T$  and  $\Pi$  (Equations 1.29a and 1.29b), thus the global stability parameters  $t_{OP}$ ,  $t^*$  and  $t_W$  (Equations 2.7, 2.17 and 2.29). We describe this connection in Chapter 4 and in Appendix D.

# Chapter 4

## Results

Given a set of different initial conditions for our  $N$ -body simulations, which are described in Chapter 3, our first goal is to analyse their results after running them through the FVFPS code (Londrillo et al., 2003). The main focus is on checking the global stability of the disc and the resulting behaviour of  $t_{OP}$ ,  $t^*$  and  $t_W$  with various choices of the input parameters described in Sections 3.2.1 and 3.4.1. To do that, we have implemented some useful diagnostic tools which keep control on the configurations of the stellar disc with the advance of time.

In this Chapter we also discuss about some simulations as examples of what our results consist of, analysing the time variations (if any) of the stellar density maps, the surface density profile, the kinetic energy curve and angular momentum curves, the  $m = 2$  modes and the half-mass radius  $R_h$  (Equation 3.4).

In conclusion, an analysis of  $t_{OP}$ ,  $t^*$  and  $t_W$  is based on the results obtained from the simulation suite. A comparison of these three parameters will give more details about the physical informations they carry from both the kinetic and the potential energy content.

## 4.1 Simulation diagnostics

In order to analyse the snapshots of our simulation runs, a part of our work was focused on building a diagnostic tool which can give us more information about the simulations from both local and global points of view. Hereafter we present our numerical implementation of the diagnostics, which can help us to state whether a disc is stable or not. For our purposed, we talk about "stable" systems when the physical quantities related to the system are not changing with time – except for the numerical noise; see, e.g., simulation  $M_h400a_h5\alpha0$  (Section 4.4.4).

### 4.1.1 Density maps

Plots like Figure 3.1 show less information than density maps in presence of a large amount of particles (i.e.  $N \gtrsim 10^4$ ), because the superposition of the particles saturates the view in the plot and may hide the spatial features that are forming in the most crowded regions of the disc. For this reason, we have built the density maps as follows:

- We take a region with size  $15 \times 15 R_{d,max}^2/R_d^2$  centred at  $R = 0$  and divide it uniformly into  $150 \times 150$  cells;
- For each cell, the diagnostic code counts the number of particle within the cell;
- The code computes the mean surface density of each cell as

$$\Sigma_{\text{cell}} = \frac{\text{particles inside cell}}{\text{cell area}}. \quad (4.1)$$

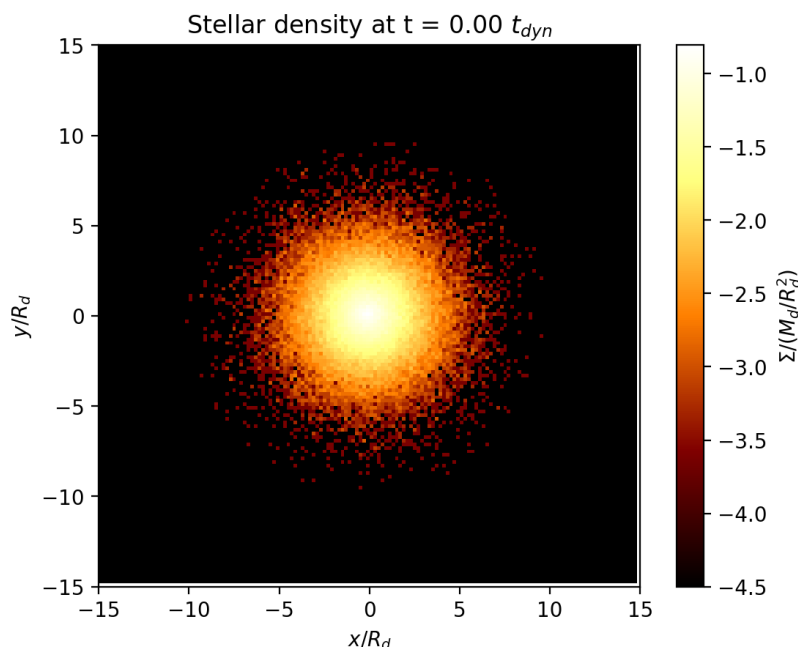


Figure 4.1: At  $t = 0$ , disc density map of the  $(x, y)$  plane.  $x$  and  $y$  axes are normalized to  $R_d$ , while the stellar density  $\Sigma$  (colour bar) is normalized to  $M_d/R_d^2$ .

The different values of  $\Sigma_{\text{cell}}$  are visualised through a colour range: each cell has a colour which corresponds with the the value of  $\Sigma_{\text{cell}}$  inside it. Figure 4.1 shows the

initial surface density map of the exponential disc, which is valid for every simulation we have run.

### 4.1.2 Surface density profiles

To compute the radial surface density of the disc. We first build a grid with ring-like profile cells. The procedure we have followed is very similar to the density maps computation steps (Section 4.1.1), but in Step 1, instead of a two-dimensional grid, we build a radial grid for  $R \in [0, R_{d,max}]$  with  $N_r = 20$  rings. The division in rings is uniform in a logarithmic scale, namely

$$\frac{R_i}{R_d} = 10^j, \quad \text{where } j = j_{min} + (i - 1) \frac{(j_{max} - j_{min})}{(N_r - 1)} \quad \forall i = 1, \dots, N_r. \quad (4.2)$$

Equation (4.2) ensures the radial grid is equally spaced from a logarithmic perspective, which means the exponents  $j$  are equally spaced in the real range  $[j_{min}, j_{max}]$ . For our purposes, we always set  $j_{min} = -1$  and  $j_{max} = 1$ , such that our grid has minimum radius  $R_1 = 0.1R_d$  and maximum radius  $R_{20} = 10R_d$ . The mean surface density inside the ring cell is computed using Equation (4.1) and then the value of  $\Sigma_{cell}$  is normalized to  $M_d/R_d^2$ .

An example of the result from this algorithm is displayed in Figure 3.2, which shows the radial surface density distribution of the initially generated disc.

### 4.1.3 Kinetic energy

We are interested in analysing the behaviour of the total kinetic energy components  $T_d$  and  $\Pi_d$  of the disc (Equations 1.29a and 1.29b) in cylindrical coordinates  $(R, \varphi, z)$  as functions of time  $t$ . Since we assume that the halo behaves as a fixed potential for all the simulation runs, thus not changing its spherically symmetric properties described in Section 3.1.1, we will focus only on the kinetic energy components of the disc. To lighten the notation, we now adopt  $K \equiv K_d$ , where  $K_d$  is the total kinetic energy of the disc,  $T \equiv T_d$  and  $\Pi \equiv \Pi_d$ . For the numerical computation, we discretize the trace of Equations (1.27) (left), (1.29a) and (1.29b) as (see, e.g., Saha and Elmegreen, 2018)

$$K = \frac{1}{2} \sum_{i=1}^N m_i v_i^2, \quad (4.3)$$

$$T = \frac{1}{2} \sum_{i=1}^N m_i v_{i,\varphi}^2 \quad (4.4)$$

$$\text{and } \frac{1}{2}\Pi = K - T, \quad (4.5)$$

where  $m_i$  is the mass of the  $i$ -th particle,  $v_i$  is the magnitude of the total velocity of the  $i$ -th disc particle and  $v_{i,\varphi}$  is the magnitude of its azimuthal component.  $m_i$  can be seen as the discretization of the infinitesimal mass  $\delta m = \Sigma(R) dR$  in Equation (2.25).

Since the FVFPS code works with Cartesian coordinated and we are adopting cylindrical coordinates, we need to compute  $v_R$  and  $v_\varphi$  for each disc particle using System (C.6) and Equations (C.2) from Appendix C. As we want also to study the

radial profiles of  $K$ ,  $T$  and  $\Pi$ , we build a radial grid as we did in Section 4.1.2, but now with  $N_r = 100$  rings and uniform in a linear scale, namely

$$R_i = R_{min} + (i - 1) \frac{(R_{max} - R_{min})}{(N_r - 1)} \quad \forall i = 1, \dots, N_r, \quad (4.6)$$

such that  $R_1 = R_{min} = 0.1R_d$  and  $R_{100} = R_{max} = 10R_d$ .

Inside each  $j$ -th ring cell, following the treatment of Saha and Elmegreen (2018), we numerically compute

$$\langle v_k \rangle_j = \frac{1}{N_j} \sum_i^{N_j} (v_k)_i \quad \text{for } k = R, \varphi, z, \quad (4.7)$$

$$(K_k)_j = \frac{1}{2} \sum_i^{N_j} m_i (v_k)_i^2 \quad \text{for } k = R, \varphi, z, \quad (4.8)$$

$$(T_k)_j = \frac{1}{2} \left( \sum_i^{N_j} m_i \right) \langle v_k \rangle_j^2 \quad \text{for } k = R, \varphi, z, \quad (4.9)$$

$$\text{and } \frac{1}{2} (\Pi_k)_j = (K_k)_j - (T_k)_j \quad \text{for } k = R, \varphi, z, \quad (4.10)$$

where  $N_j$  is the number of particles inside the  $j$ -th ring. Every kinetic energy component is then normalized to  $GM_d^2/R_d$ .

#### 4.1.4 Angular momentum

We study the evolution of the angular momentum  $\mathbf{L}$  of the disc along the  $x$ ,  $y$  and  $z$  directions. To do so, we use the same radial grid as in Section 4.1.2 and we use the definition  $\mathbf{L} = \mathbf{x} \wedge m\mathbf{v}$  and compute  $L_x$ ,  $L_y$  and  $L_z$  inside each  $j$ -th ring cell (see, e.g., Saha and Elmegreen, 2018) as

$$L_x(j) = \sum_i^{N_j} m_i \times (y_i v_{z,i} - z_i v_{y,i}), \quad (4.11)$$

$$L_y(j) = \sum_i^{N_j} m_i \times (z_i v_{x,i} - x_i v_{z,i}), \quad (4.12)$$

$$\text{and } L_z(j) = \sum_i^{N_j} m_i \times (x_i v_{y,i} - y_i v_{x,i}), \quad (4.13)$$

$$(4.14)$$

where  $N_j$  refers to the particles inside the  $j$ -th ring cell. We also computed the total angular momentum components of the disc as

$$L_{x,tot} = \sum_j L_x(j), \quad L_{y,tot} = \sum_j L_y(j), \quad L_{z,tot} = \sum_j L_z(j), \quad (4.15)$$

thus summing all the contribution of  $L_x$ ,  $L_y$  and  $L_z$  from each  $j$ -th ring.

Every angular momentum component is then normalized to  $(GM_d^3 R_d)^{1/2}$ .

### 4.1.5 Half-mass radius $R_h$ of the disc

At any time  $t$  in the simulation, we compute  $R_h$  as the radius lying in the equatorial plane of the circle (centred in the origin) that contains half of the particles.

Since this algorithm can be applied for every snapshot of the simulation runs, we can study the evolution (if any) of  $R_h$  as function of time  $t$ . To do so, we take the initial value of the half-mass radius  $R_{h,0}$  and compare to  $R_h$  at subsequent times and compute the relative variation with respect to  $R_{h,0}$ , which is

$$\frac{R_h - R_{h,0}}{R_{h,0}}. \quad (4.16)$$

### 4.1.6 $m = 2$ modes of the disc

Following the treatment of Sellwood (2016), we measure the departure of the surface density distribution of the disc from axial symmetry using Fourier mode amplitudes  $A_m$  at time  $t$

$$A_m(t) = \left| \sum_j \mu_j e^{im\varphi_j} \right|, \quad (4.17)$$

where<sup>1</sup>  $\mu_j$  and  $\varphi_j$  are the mass and the polar angle of the  $j$ -th disc particle, respectively. In particular, for  $m = 0$  we obtain the total disc mass  $M_d$

$$A_0 = \sum_j \mu_j = M_d, \quad (4.18)$$

whose value remains constant for all the simulation run. Our focus will be on the bar amplitude inside the disc, which can be defined through the  $m = 2$  modes (e.g., Collier et al., 2019), namely

$$\frac{A_2}{A_0} = \frac{1}{A_0} \left| \sum_j \mu_j e^{2i\varphi_j} \right|, \quad (4.19)$$

where we normalize the  $m = 2$  to the monopole  $A_0 \equiv M_d$ .

In the following we will show the evolution of the  $A_2/A_0$  ratio as function of time  $t$  in a log-linear plot. The presence of a straight line in this plot would be the signature of an exponential growth of the bar amplitude (Sellwood, 2016). Differently from Collier et al. (2019), the  $A_2/A_0$  ratio is computed using all the particles, with no restriction to the radial region.

### 4.1.7 $t_{OP}$ , $t^*$ and $t_W$ computation

Given a disc-halo system with a Hernquist DM halo and a razor-thin exponential disc which is initially steady rotating, we always compute the parameters  $t_{OP}$ ,  $t^*$  and  $t_W$  (Equations 2.7, 2.17 and 2.29) at the beginning of the simulation. Given the aforementioned initial configuration (particles are moving on circular orbits with  $v_\phi(R) = v_c(R)$ ; see Section 3.2.2), the computation of  $T$  from the total kinetic energy

---

<sup>1</sup>In this subsection we use  $\mu$  instead of  $m$  to indicate the particle mass, to avoid confusion with the Fourier mode  $m$ .

$K$  is the same for  $t_{OP}$ ,  $t^*$  and  $t_W$  (see Section 2.3 and Equation (2.24)). Numerically, at  $t = 0$  we compute  $K$  as in have

$$K = \frac{1}{2} \sum_{j=1}^N m_j v_j^2, \quad (4.20)$$

$$T = (1 - 2\alpha)^2 K, \quad (4.21)$$

$$\text{and } \Pi = 8\alpha(1 - \alpha)K, \quad (4.22)$$

where  $\alpha$  is the fraction of retrograde stars and the  $j$  index refers to the  $j$ -th particle ( $j = 1, \dots, N$ ). (See Appendix D for the analytical computation of Equations D.20 and D.21.)

The gravitational potential energy components of  $W$  are computed both analytically and numerically. The total gravitational energy of the system  $W$  is computed using Equation (2.5), while in the evaluation of  $W_{dh}$  we use the trace of the Chandrasekhar potential-energy tensor (Equation 1.8). Given  $N$  particles, the discrete computation of  $W_d$  and  $W_{d\leftrightarrow h}$  is:

$$W_d = \frac{1}{2} \sum_{j=1}^N m_j \Phi_d(R_j, 0) \quad (4.23)$$

$$W_{d\leftrightarrow h} = \sum_{j=1}^N m_j \Phi_h(R_j) \quad (4.24)$$

The calculation of  $W_h$  is purely analytical and its expression is given in Equation (3.14).

As far as we can see,  $W_{dh}$  cannot be computed analytically using elementary functions. For this reason, once written

$$\begin{aligned} W_{dh} &= \int d^3\mathbf{x} \rho_d(\mathbf{x}) \langle \mathbf{x}, \nabla \Phi_h(\mathbf{x}) \rangle = \\ &= - \int_0^R \int_0^{2\pi} \int_0^z \Sigma_d(R) \delta(z=0) \frac{GM_h}{(R^2 + z^2)^{1/2} + a} R dR d\varphi dz = \\ &= -2\pi GM_h \Sigma_0 \int_0^R e^{-R/R_d} \frac{R}{R+a} dR, \end{aligned} \quad (4.25)$$

from now on, the integral in the last line of Equation (4.25) is evaluated numerically.

Given the initial values of  $T$  and of all the  $W$ -components, the computation of the  $t_{OP}$ ,  $t^*$  and  $t_W$  parameters at  $t = 0$  is straightforward.

## 4.2 Initial parameters of the $N$ -body simulations

Table 4.1 give an outline of all the simulations performed in this work. Some of them are presented in Sections 4.3 and 4.4 to illustrate the main results we have found from our simulations.

Name	§	$\frac{M_h}{M_d}$	$\frac{a_h}{R_d}$	$t_{dyn}/t_u$	$\alpha$	$t_{OP}$	$t^*$	$t_W$	stable
$M_h0a_h0\alpha0$	4.3.1	0	0	17.27	0	0.5	0.5	0.5	No
$M_h0a_h0\alpha0$	4.3.2	0	0	17.27	1/2	0	0	0	No
$M_h2a_h0.01\alpha0$	/	2	0.01	9.7	0	0.014	0.059	0.433	No
$M_h2a_h0.1\alpha0$	/	2	0.1	10.23	0	0.079	0.073	0.411	No
$M_h400a_h0.1\alpha0$	/	400	0.1	0.72	0	0.0005	0.0006	0.5	Yes
$M_h1.5a_h1\alpha0.5$	/	1.5	1	12.393	0	0.239	0.241	0.5	No
$M_h2a_h1\alpha0$	/	2	1	11.5	0	0.202	0.205	0.5	No
$M_h4a_h1\alpha0$	/	4	1	9.22	0	0.124	0.129	0.5	No
$M_h10a_h1\alpha0$	/	10	1	6.4	0	0.057	0.061	0.5	No
$M_h20a_h1\alpha0$	/	20	1	4.69	0	0.03	0.033	0.5	No
$M_h50a_h1\alpha0$	/	50	1	3.03	0	0.012	0.014	0.5	Yes
$M_h100a_h1\alpha0$	/	100	1	2.16	0	0.006	0.007	0.5	Yes
$M_h200a_h1\alpha0$	/	200	1	1.54	0	0.003	0.003	0.5	Yes
$M_h400a_h1\alpha0$	/	400	1	1.09	0	0.0016	0.0017	0.5	Yes
$M_h2/3a_h2\alpha0$	/	2/3	2	15.6	0	0.356	0.401	0.5	No
$M_h1.5a_h2\alpha0$	/	1.5	2	14.1	0	0.255	0.321	0.5	No
$M_h2a_h2\alpha0$	/	2	2	13.38	0	0.217	0.287	0.5	No
$M_h4a_h2\alpha0$	/	4	2	11.31	0	0.134	0.201	0.5	No
$M_h10a_h2\alpha0$	/	10	2	8.3	0	0.061	0.106	0.5	No
$M_h20a_h2\alpha0$	/	20	2	6.24	0	0.032	0.0594	0.5	No
$M_h50a_h2\alpha0$	/	50	2	4.1	0	0.013	0.0256	0.5	Yes
$M_h100a_h2\alpha0$	/	100	2	2.95	0	0.007	0.013	0.5	Yes
$M_h200a_h2\alpha0$	/	200	2	2.1	0	0.003	0.0066	0.5	Yes
$M_h400a_h2\alpha0$	/	400	2	1.48	0	0.0016	0.003	0.5	Yes
$M_h2a_h5\alpha0$	/	2	5	15.75	0	0.252	0.403	0.5	No
$M_h4a_h5\alpha0$	4.4.1	4	5	14.58	0	0.153	0.338	0.5	No
$M_h4a_h5\alpha0.5$	4.4.2	4	5	14.58	1/2	0	0	0	No
$M_h10a_h5\alpha0$	4.4.3	10	5	12.18	0	0.063	0.228	0.5	No
$M_h10a_h5\alpha0.5$	/	10	5	12.18	1/2	0	0	0	No
$M_h20a_h5\alpha0$	/	20	5	9.94	0	0.03	0.148	0.5	No
$M_h20a_h5\alpha0.5$	/	20	5	9.94	1/2	0	0	0	No
$M_h50a_h5\alpha0$	/	50	5	7.02	0	0.011	0.072	0.5	No
$M_h50a_h5\alpha0.5$	/	50	5	7.02	1/2	0	0	0	No
$M_h100a_h5\alpha0$	/	100	5	5.18	0	0.005	0.039	0.5	No
$M_h200a_h5\alpha0$	/	200	5	3.75	0	0.003	0.02	0.5	Yes
$M_h400a_h5\alpha0$	4.4.4	400	5	2.68	0	0.001	0.01	0.5	Yes
$M_h400a_h5\alpha0.5$	/	400	5	2.68	1/2	0	0	0	Yes

Table 4.1: Summary table of our simulations named as indicated in the first column. All simulations have number of particles  $N = 102400$ , total disc mass  $M_d/M_u = 1$ , disc scale length  $R_d/l_u = 1$ , disc truncation radius  $R_{d,max}/R_d = 10$ , initial time step  $\Delta t_{in} = 10^{-3}t_{dyn}$ , softening length  $\epsilon = 0.013R_d$  and opening parameter  $\theta_{min} = 0.4$ .  $\alpha$  is the fraction of retrograde orbits (see Section 3.4.1).  $M_h$  is the total halo mass  $M_h$  and  $a_h$  is the halo scale length. The dynamical time  $t_{dyn}$  is defined by Equation (3.29). For the computation of  $t_{OP}$ ,  $t^*$  and  $t_W$  (Equations (2.7), (2.17) and (2.29)) at  $t = 0$ , see Section 4.1.7. The symbol '§' refers to the subsection in which the simulation is described (when applicable).

## 4.3 Simulations without dark halo

### 4.3.1 Simulation $M_h 0 a_h 0 \alpha 0$ ( $M_h = 0, \alpha = 0$ )

#### Initial conditions and parameters

Name	§	$\frac{M_h}{M_d}$	$\frac{a_h}{R_d}$	$t_{dyn}/t_u$	$\alpha$	$t_{OP}$	$t^*$	$t_W$	stable
$M_h 0 a_h 0 \alpha 0$	4.3.1	0	0	17.27	0	0.5	0.5	0.5	No

Table 4.2: Summary table of the simulation  $M_h 0 a_h 0 \alpha 0$ . All the input parameters are explained in the caption of Table 4.1.

For the initial mass distribution of the disc particles, see Figures 3.1, 3.2, 3.3, and 4.1. The initial speed curves are shown in Figure 3.5 (dashed line). The initial kinetic energy and angular momentum distributions are shown in Figures 4.2.

### Results

In case of a razor-thin exponential disc-only system, whose particles are moving around pure circular orbits with  $v_\varphi = v_c$  under the potential well of the disc itself, the system is not stable. In particular, the Toomre (1964) parameter  $Q = 0$  because there is no velocity dispersion ( $\sigma^2 = 0$ ). Since the first dynamical time, Figures 4.3 (top panels) show that substructures are forming through local instabilities (e.g., Jeans, 1902; Toomre, 1964). After  $10t_{dyn}$ , the two main dense regions are merging, orbiting around each other, with no hint of a bar formation. It is worth noticing that all the disc particles are free to move, with no constraints on the motion along a privileged plane. However, in every simulation run we have found that all the disc particles move only on the  $z = 0$  plane, developing no vertical motions along the  $z$  axis.

These results help us to the interpretation of Figure 4.3 (bottom left), which shows the ratio  $A_2/A_0$  (see Section 4.1.6), because there is a steep rise of the  $m = 2$  modes in less than  $1t_{dyn}$ . Even though there is a high  $A_2/A_0 > 0.1$  ratio, no bar is present in the system. Furthermore, the nature of the disc has changed during the time: there were more substructures colliding to each other, as a consequence of the disruption of the disc from its unstable equilibrium of the initial conditions. Although the system is not axisymmetric anymore, we compute its half-mass radius (Section 4.1.5), which we can see in Figure 4.3 (bottom right). One main information that we achieve from the  $R_h - t$  plot is the disc has been extending throughout the simulation period.

The surface density profiles also confirm this scenario: the nature of the system has changed so much that the initial exponential profile of the disc is no longer present.

The kinetic energy content (Figures 4.5) is made up of both ordered and random motions, where the latter are always prevailing the former. Central regions ( $R/R_d < 2$ ) give little contribution to the kinetic energy of the system because of the lower density there. The main part of  $K$  is concentrated between  $2 < R/R_d < 6$  at  $t = 1.5t_{dyn}$ . The interpretation of the two peaks at  $t = 10t_{dyn}$  can be related to the main substructures that are orbiting around each other, in a phase of merging. This physical aspect is also confirmed by the angular momentum plots (Figures 4.6), where two peaks are visible in the final snapshot at  $t = 10t_{dyn}$  as in Figure 4.6 (right).

We now turn our attention to the analysis of the main global quantities that are associated with the kinetic aspect of the system. Specifically, we focus on the ordered

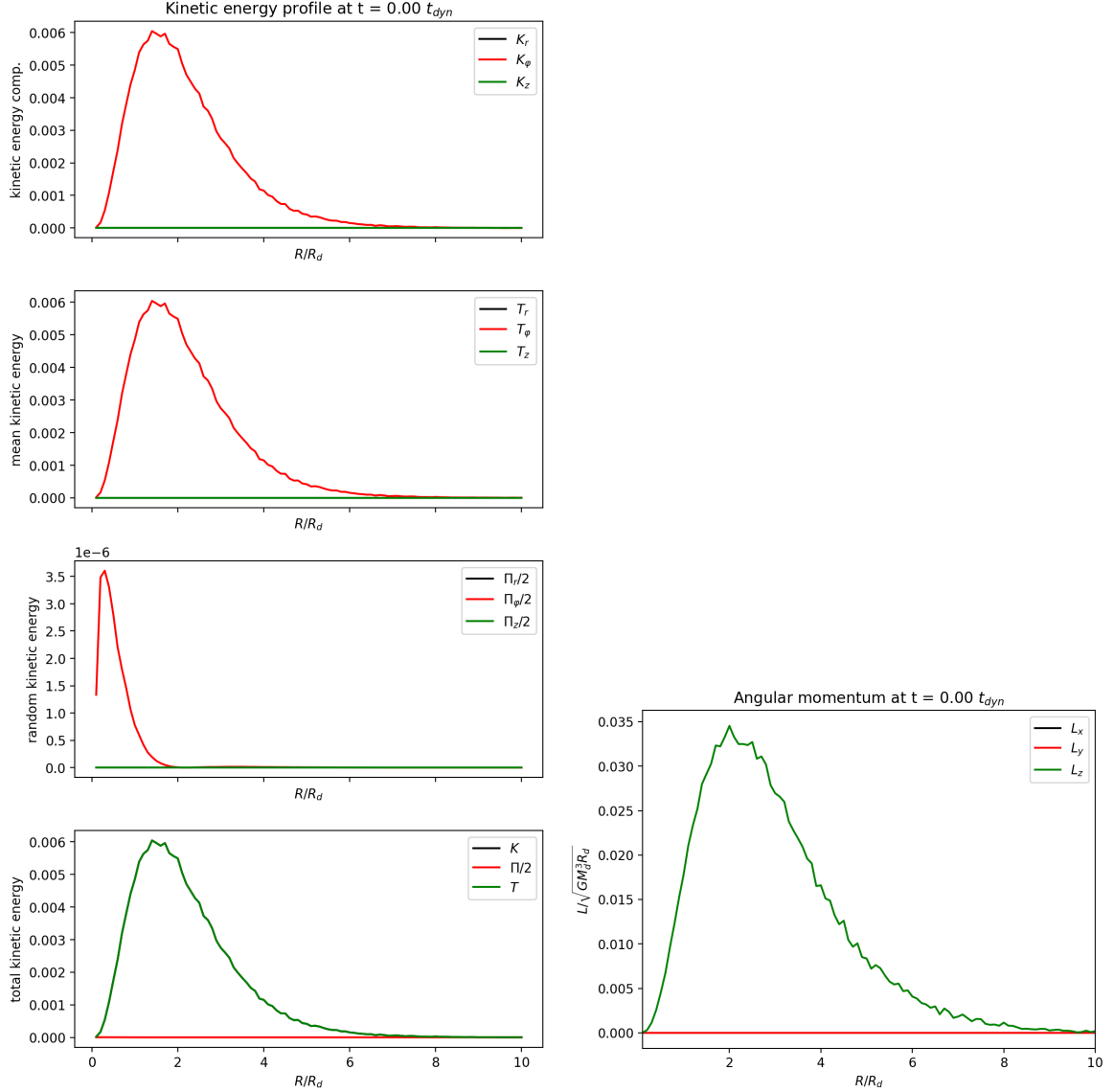


Figure 4.2: Simulation  $M_h0a_h0\alpha0$ . (Left) Initial profiles of the kinetic energy components. Radii and energies are normalized to  $R_d$  and  $GM_d^2/R_d$ , respectively. (Right) Initial profiles of the angular momentum components.  $R$  and all the  $\mathbf{L}$ -components are normalized to  $R_d$  and  $(GM_d^3 R_d)^{1/2}$ , respectively.

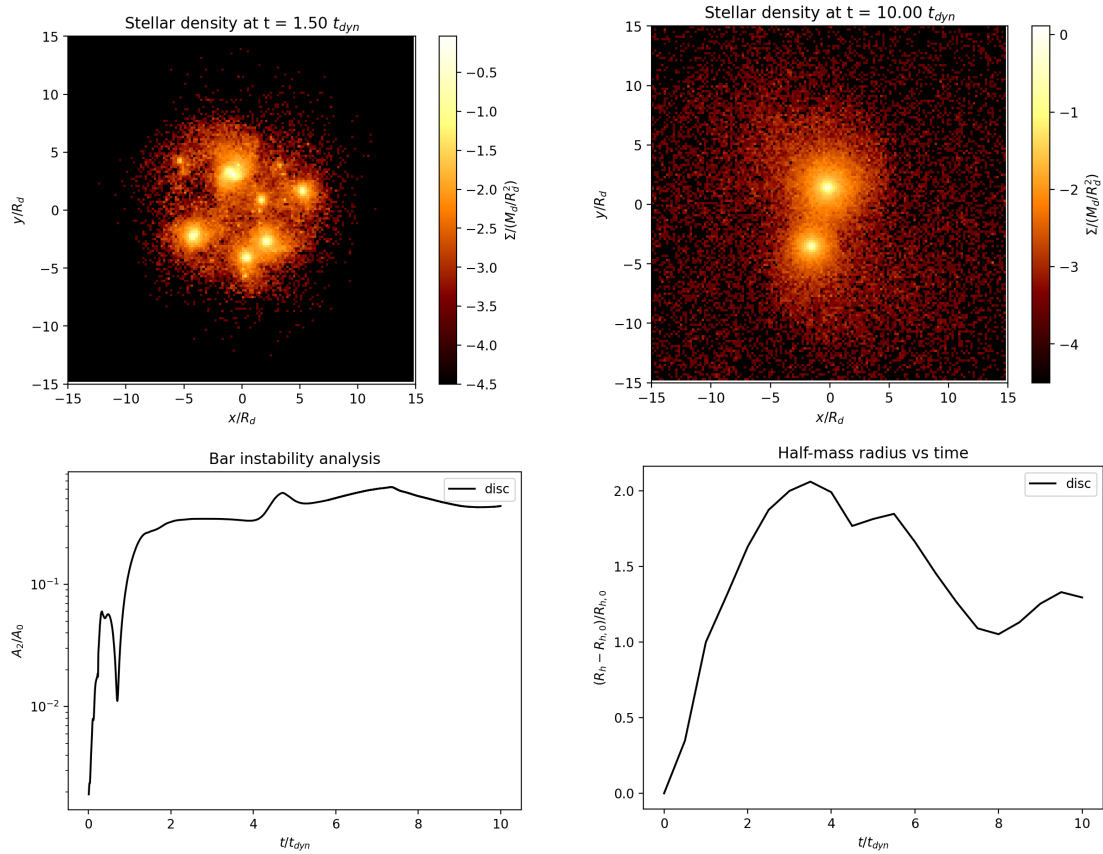


Figure 4.3: (*Top panels*) Simulation  $M_h0a_h0\alpha0$ . Evolution of the disc density map of the  $(x, y)$  plane with time.  $x$  and  $y$  axes are normalized to  $R_d$ , while  $\Sigma$  (colour bar) is normalized to  $M_d/R_d^2$ . (*Bottom left*) Evolution of the bar amplitude  $A_2/A_0$  with time. (*Bottom right*) Evolution of the fractional variation of the half-mass radius with time. Time is normalized to  $t_{dyn}$ .

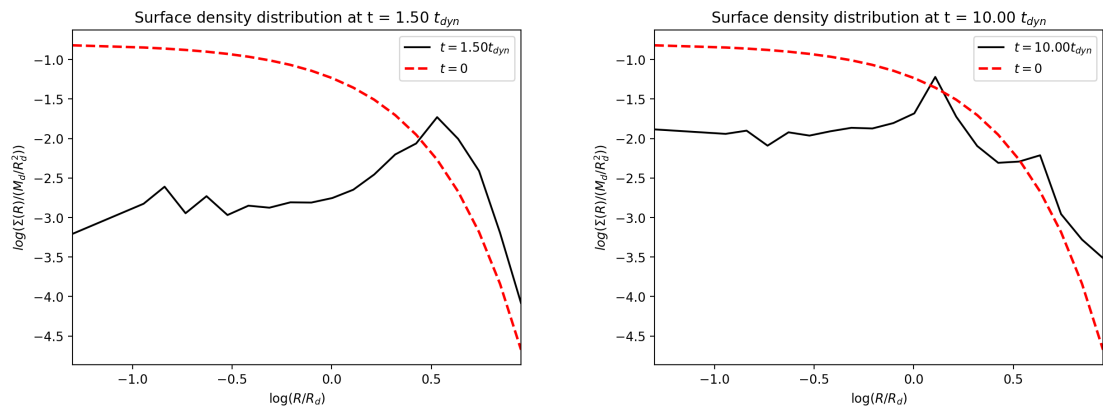


Figure 4.4: Simulation  $M_h0a_h0\alpha0$ . Disc surface density profiles (black) at  $t = 1.5t_{dyn}$  (left) and  $t = 10t_{dyn}$  (right) compared to the initial one (dashed red).  $R$  and  $\Sigma(R)$  are normalized to  $R_d$  and  $M_d/R_d^2$ , respectively.

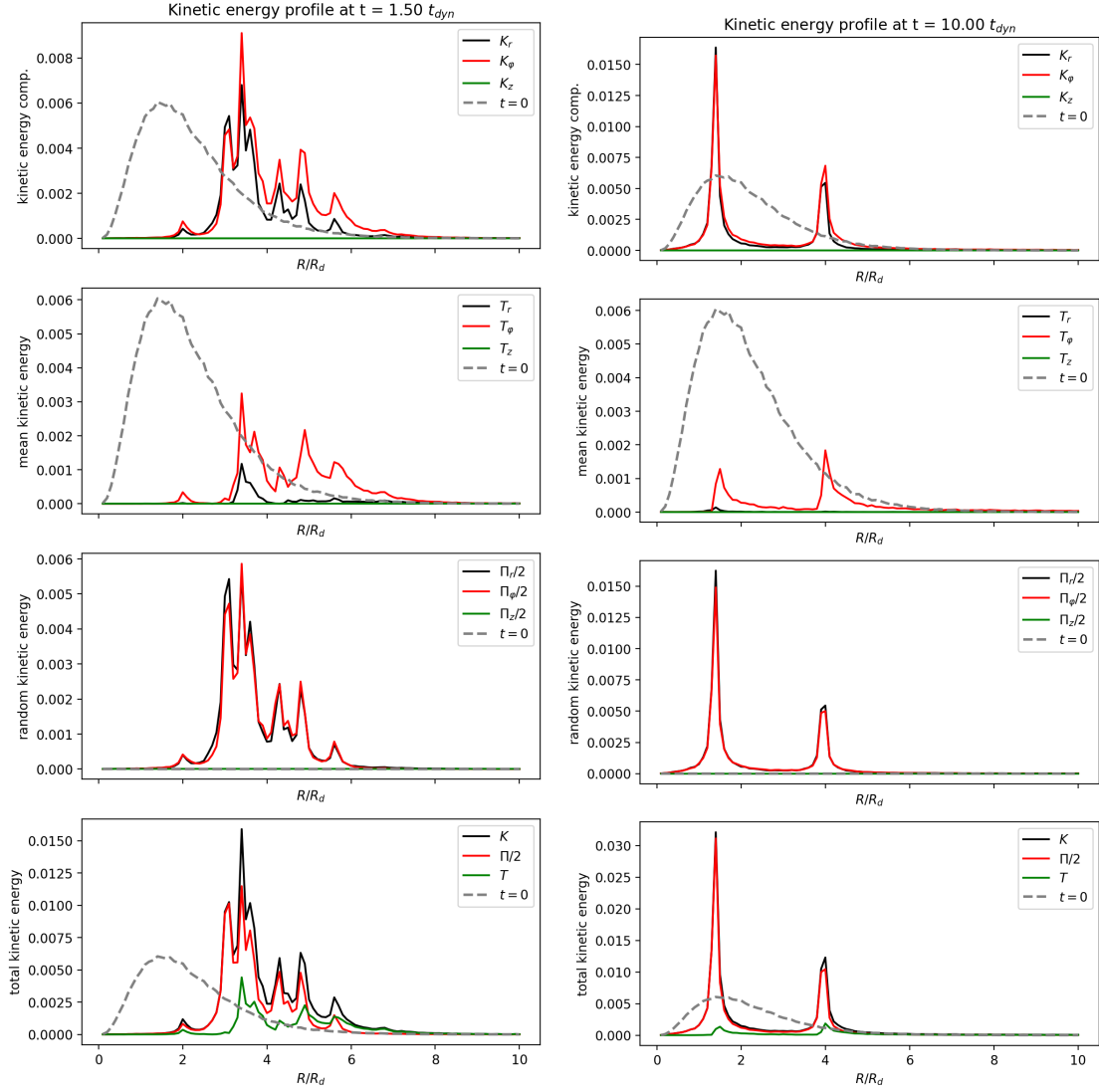


Figure 4.5: Simulation  $M_h0a_h0a0$ . Evolution of the kinetic energy components with time, compared to the initial profile (dashed gray line). Radii and energies are normalized to  $R_d$  and  $GM_d^2/R_d$ , respectively.

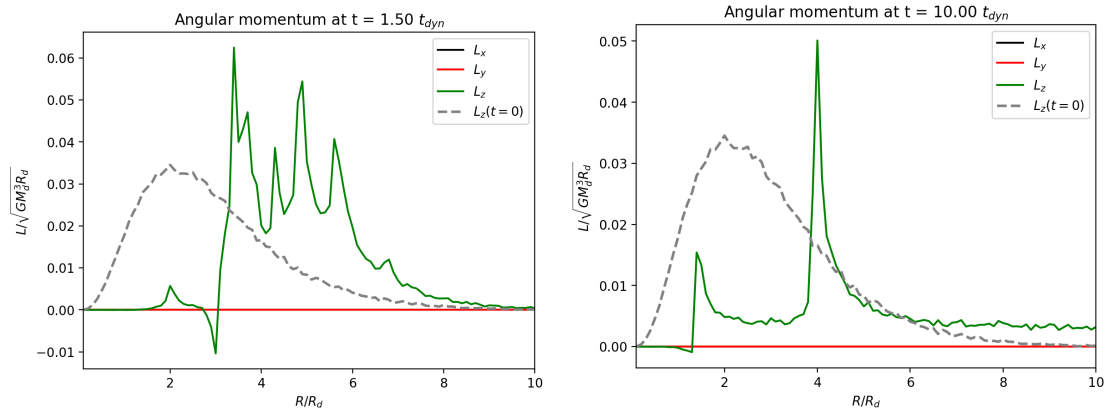


Figure 4.6: Simulation  $M_h0a_h0a0$ . Evolution of the angular momentum components with time, compared to the initial profile (dashed gray line).  $R$  and all the  $\mathbf{L}$ -components are normalized to  $R_d$  and  $(GM_d^3 R_d)^{1/2}$ , respectively.

kinetic energy of rotation  $T$ , the random kinetic energy of rotation  $\Pi$  and the total angular momentum in the z-axis  $L_{z,tot}$  of the disc. Both the ordered and random kinetic energies of the disc (Figure 4.7) change drastically in the subsequent times, giving an additional hint that the system is not stable. In particular, random motions become dominant, as we also see in Figure 4.5. We know from Hohl (1976) that an unstable disc has a time-decreasing ordered kinetic energy  $T$ . Even though the radial profile of the angular momentum changes with time, the total angular momentum is not. Since only  $L_z \neq 0$ , Figure 4.7 (right) shows only  $L_{z,tot}$ , which is not changing with time. This means that the total angular momentum of an isolated system is conserved.

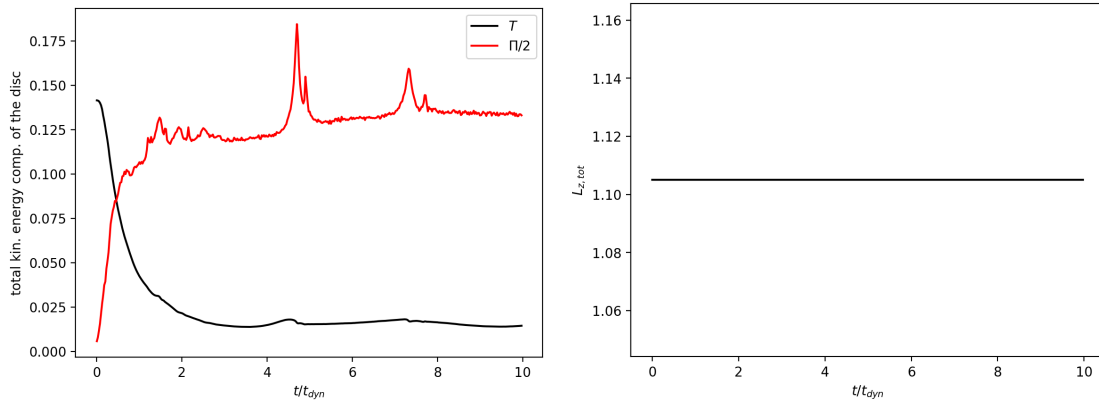


Figure 4.7: Simulation  $M_h 0 a_h 0 \alpha 0$ . (*Left*) Evolution of the total ordered and random kinetic energies  $T$  and  $\Pi$  with time. Radii and energies are normalized to  $R_d$  and  $GM_d^2/R_d$ , respectively. (*Right*) Evolution of the total angular momentum  $L_{z,tot}$  with time.  $R$  and  $L_{z,tot}$  are normalized to  $R_d$  and  $(GM_d^3 R_d)^{1/2}$ , respectively.

### 4.3.2 Simulation $M_h0a_h0\alpha0.5$ ( $M_h = 0, \alpha = 0.5$ )

#### Initial conditions and parameters

Name	§	$\frac{M_h}{M_d}$	$\frac{a_h}{R_d}$	$t_{dyn}/t_u$	$\alpha$	$t_{OP}$	$t^*$	$t_W$	stable
$M_h0a_h0\alpha0.5$	4.3.1	0	0	17.27	0.5	0	0	0	No

Table 4.3: Summary table of the simulation  $M_h0a_h0\alpha0.5$ . All the input parameters are explained in the caption of Table 4.1.

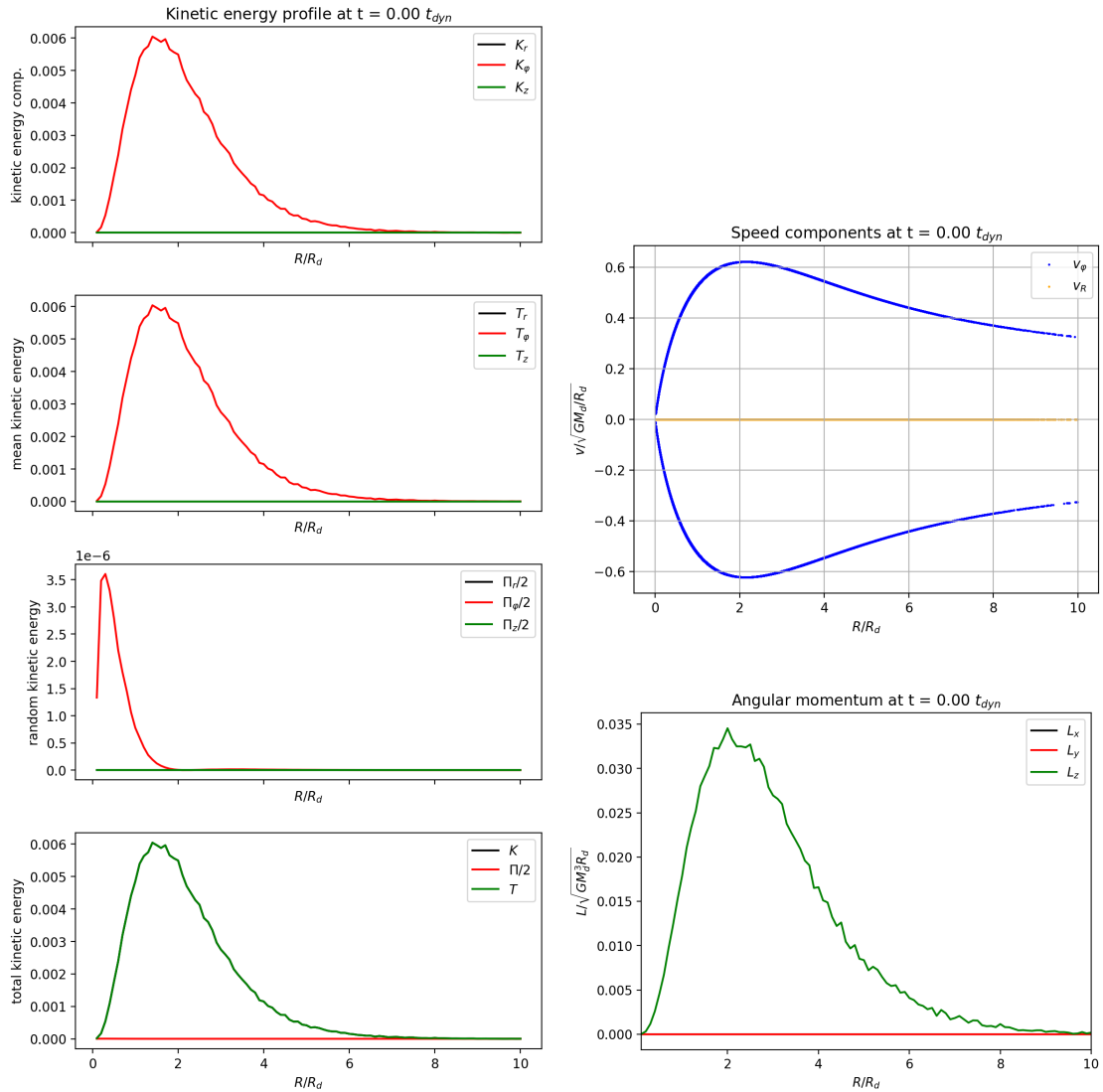


Figure 4.8: Simulation  $M_h0a_h0\alpha0.5$ . (Left) Initial profiles of the kinetic energy components. Radii and energies are normalized to  $R_d$  and  $GM_d^2/R_d$ , respectively. (Top right) Initial rotation velocity of particles.  $R$  is normalized to  $R_d$ , while the  $\mathbf{v}$ -components are normalized to  $(GM_d/R_d)^{1/2}$ . (Bottom right) Initial profiles of the angular momentum components.  $R$  and all the  $\mathbf{L}$ -components are normalized to  $R_d$  and  $(GM_d^3R_d)^{1/2}$ , respectively.

For the initial mass distribution of the disc particles, see Figures 3.1, 3.2, 3.3, and

4.1. The initial rotation curve of the particles, the initial kinetic energy and angular momentum distributions are shown in Figures 4.8.

## Results

By inverting half of the total number of orbits, in order to have 50% of retrograde stars (see Section 3.4.1) and vanishing total angular momentum  $\mathbf{L}_{tot} = 0$ , the disc behaves different from the case discussed in Section 4.3.1 (simulation  $M_h0a_h0\alpha0$ ). The azimuthal velocity dispersion  $\sigma_\varphi^2$  contributes to weaken the local instability, thus preventing the formation of substructures. In the first dynamical times, as we see from Figures 4.9, the disc is divided into a central area and a surrounding external ring ( $t = 2.5t_{dyn}$ ), without the formation of a bar. This ring feature disappears lately at  $t = 4t_{dyn}$ , leading to a barely axisymmetric denser region surrounded by a mantle of stars that are not distributed axisymmetrically.

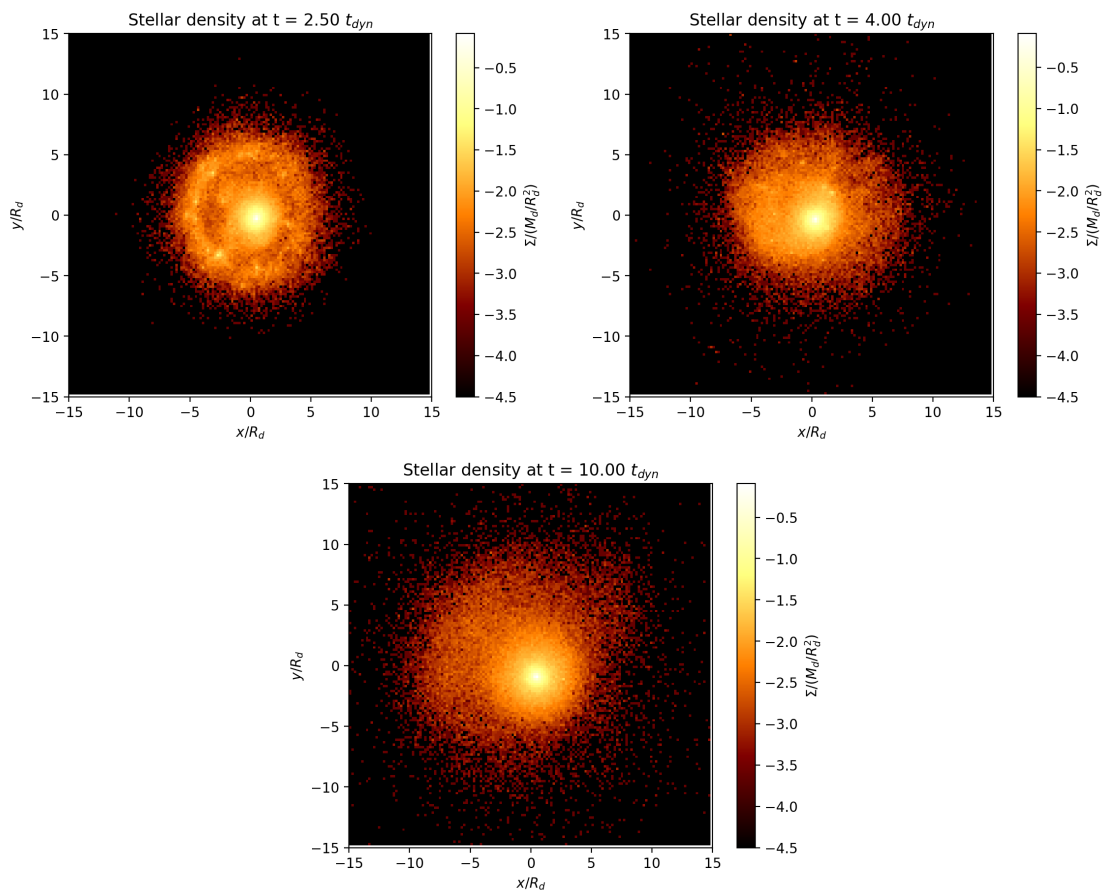


Figure 4.9: Simulation  $M_h0a_h0\alpha0.5$ . Evolution of the disc density map of the  $(x, y)$  plane with time.  $x$  and  $y$  axes are normalized to  $R_d$ , while  $\Sigma$  (colour bar) is normalized to  $M_d/R_d^2$ .

Also here, the absence of a bar cannot be seen through the  $A_2/A_0$  ratio, reported for this simulation in Figure 4.10 (left), has a steep rise up to  $A_2/A_0 \sim 10^{-1}$ . The growth of the half-mass radius is from 25% to 30%, but still shows the system has not been changed dramatically as in the  $\alpha = 0$  scenario (Section 4.3.1).

The evolution of the surface density profile shows that the disc is also changing its  $\Sigma(R)$ , comparing to the initial profile (Figures 4.11, red lines), which is lower in the

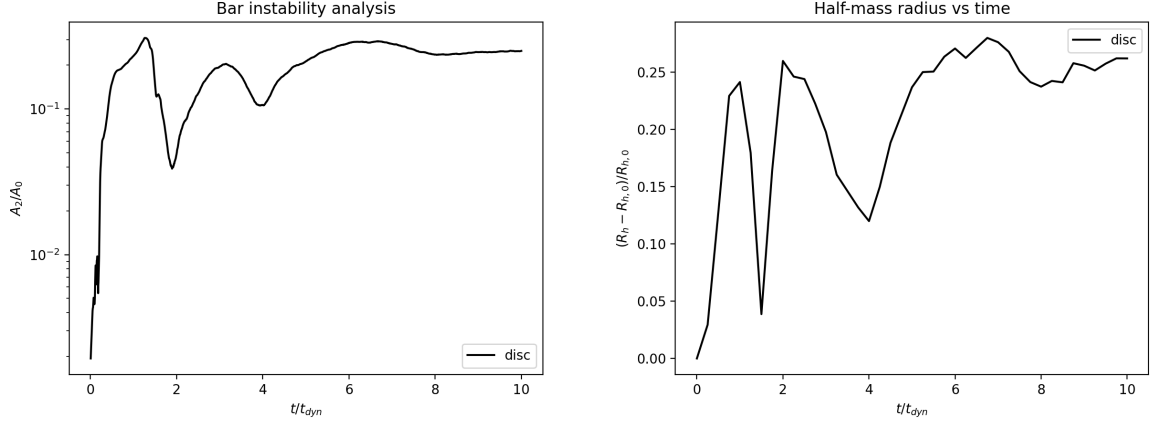


Figure 4.10: Simulation  $M_h0a_h0\alpha0.5$ . (Left) Evolution of the bar amplitude  $A_2/A_0$  with time. (Right) Evolution of the fractional variation of the half-mass radius with time. Time is normalized to  $t_{dyn}$ .

inner regions and less steep in the outermost regions.

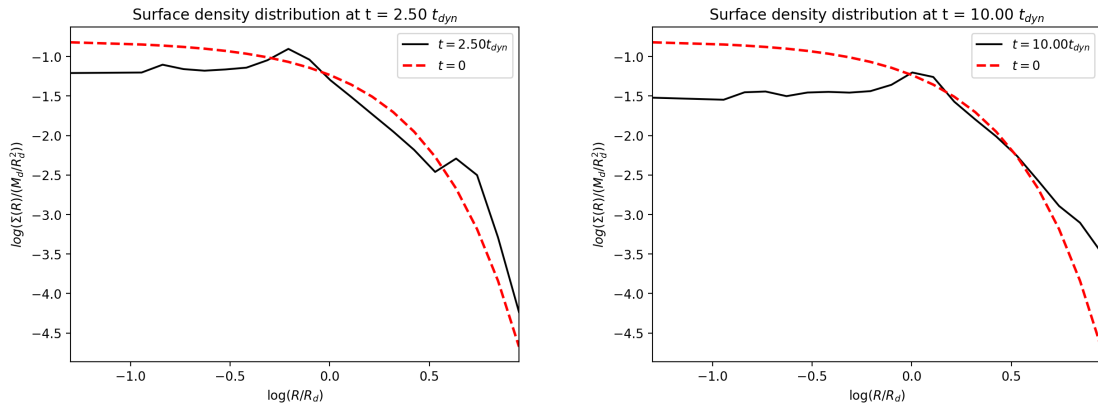


Figure 4.11: Simulation  $M_h0a_h0\alpha0.5$ . Disc surface density profile (black) at  $t = 2.5t_{dyn}$  (left) and  $t = 10t_{dyn}$  (right) compared to the initial one (dashed red).  $R$  and  $\Sigma(R)$  are normalized to  $R_d$  and  $M_d/R_d^2$ , respectively.

The plots of the kinetic energy components show the effect of the presence of the retrograde orbits. The ordered motions, both radial and azimuthal, are negligible with respect to the random components, which are the main contribution to the total kinetic energy at every radius. A kinetic energy peak in the innermost regions of the disc is detected in this simulation (Figures 4.12), which shifts from  $R/R_d < 1$  to  $1 < R/R_d < 2$  in the outside. At  $t = 2.5t_{dyn}$  (Figure 4.12, left) there is an external rise of the total kinetic energy at  $4 < R/R_d < 6$ , which is related to the presence of the ring surrounding the central structure. In fact, as the ring vanishes later on in the simulation, only the innermost peak survives (Figure 4.12, right).

The total angular momentum is initially null ( $\mathbf{L} = 0$ ), because half of the orbits, picked randomly from the whole set, have been inverted. The main consequence of this choice is that the range value of the local angular momentum is also  $1/10$  of the respective  $\alpha = 0$  case (Section 4.3.1) and  $L_z$  – the main and only contributor – oscillates in values close to zero. In particular, at  $t = 10t_{dyn}$ ,  $L_z$  is negligible ( $|L_z|/(GM_d^3 R_d)^{1/2} < 10^{-3}$ ) with respect to the  $\alpha = 0$  scenario.

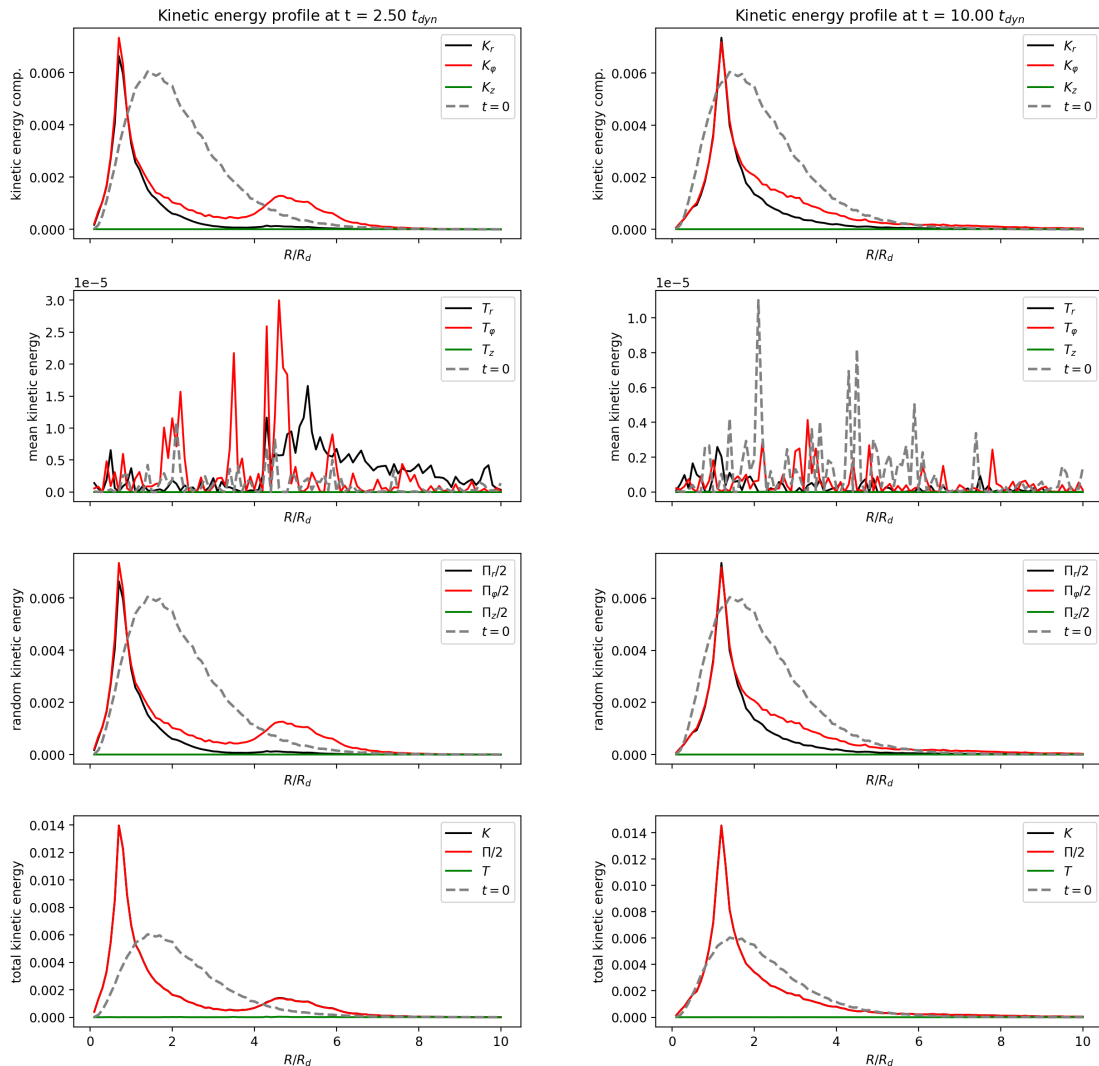


Figure 4.12: Simulation  $M_h0a_h0\alpha0.5$ . Evolution of the kinetic energy components with time, compared to the initial profile (dashed gray line). Radii and energies are normalized to  $R_d$  and  $GM_d^2/R_d$ , respectively.

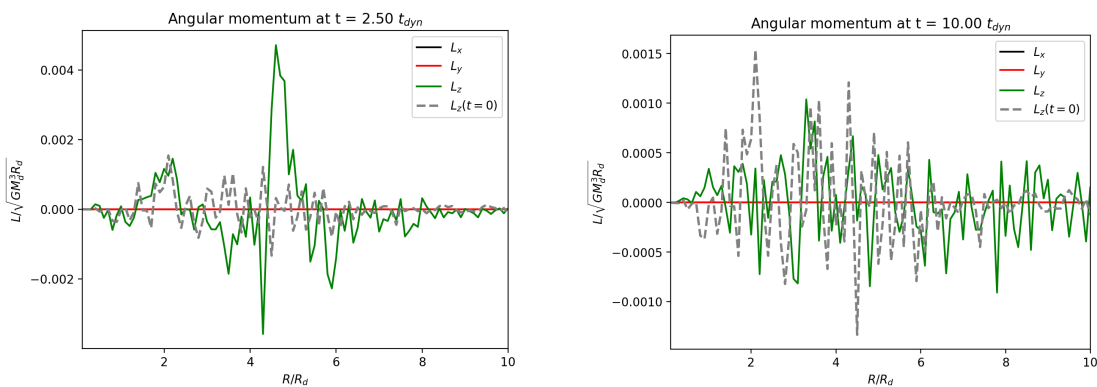


Figure 4.13: Simulation  $M_h0a_h0\alpha0.5$ . Evolution of the angular momentum components with time, compared to the initial profile (dashed gray line).  $R$  and all the  $\mathbf{L}$ -components are normalized to  $R_d$  and  $(GM_d^3 R_d)^{1/2}$ , respectively.

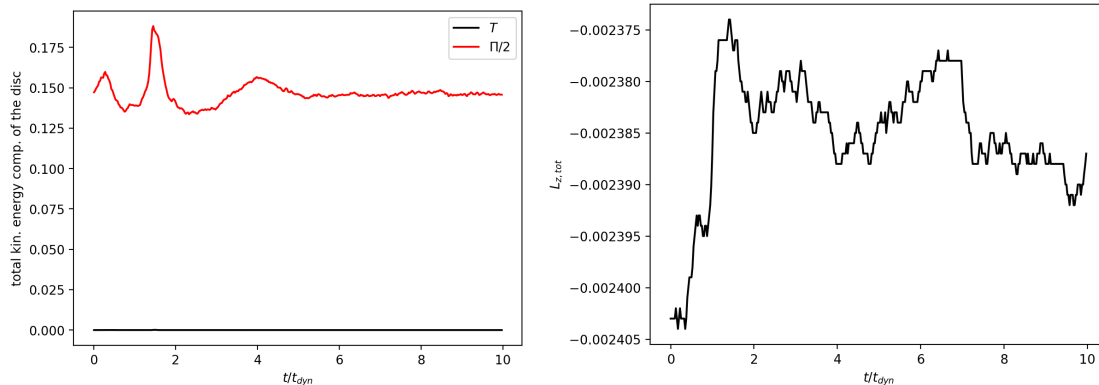


Figure 4.14: Simulation  $M_h 0 a_h 0 \alpha 0.5$ . (*Left*) Evolution of the total ordered and random kinetic energies  $T$  and  $\Pi$  with time. Radii and energies are normalized to  $R_d$  and  $GM_d^2/R_d$ , respectively. (*Right*) Evolution of the total angular momentum  $L_{z,tot}$  with time.  $R$  and  $L_{z,tot}$  are normalized to  $R_d$  and  $(GM_d^3 R_d)^{1/2}$ , respectively.

Concerning the global kinematic properties of the disc, in this case the total ordered kinetic energy of the disc  $T$  is always negligible – which is expected also from the radial profile of  $T$  (Figure 4.12), while the total random kinetic energy  $\Pi$  changes within  $t \simeq 5t_{dyn}$ , then its value is conserved (Figure 4.14, left). This means that also in this case  $\Pi$  changes in subsequent times, even when the disc is less unstable than in the simulation  $M_h 0 a_h 0 \alpha 0$ . Since only  $L_z \neq 0$ , Figure 4.14 (right) shows  $L_{z,tot}$  varying during time. However, these variations are small and close to zero, as in our models all the cases with  $\alpha = 1/2$  have vanishing total angular momentum – together with  $T$ .

## 4.4 Simulations with dark halo

### 4.4.1 Simulation $M_h 4 a_h 5 \alpha 0$ ( $M_h/M_d = 4$ , $a_h/R_d = 5$ , $\alpha = 0$ )

#### Initial conditions and parameters

Name	§	$\frac{M_h}{M_d}$	$\frac{a_h}{R_d}$	$t_{dyn}/t_u$	$\alpha$	$t_{OP}$	$t^*$	$t_W$	stable
$M_h 4 a_h 5 \alpha 0$	4.4.1	4	5	14.58	0	0.153	0.338	0.5	No

Table 4.4: Summary table of the simulation  $M_h 4 a_h 5 \alpha 0$ . All the input parameters are explained in the caption of Table 4.1.

For the initial mass distribution of the disc particles, see Figures 3.1, 3.2, 3.3, and 4.1. The initial rotation curve of the particles, the initial kinetic energy and angular momentum distributions are shown in Figures 4.15.

## Results

As we can immediately see from Figures 4.16, in this simulation the disc is evolving, which means the system is not stable. From the surface density maps shown in Figures 4.16, some parts of the disc develop local instabilities. We should notice that the initial conditions generate a cold disc with  $\sigma = 0$ , thus with an initial Toomre (1964) parameter  $Q = 0$ .

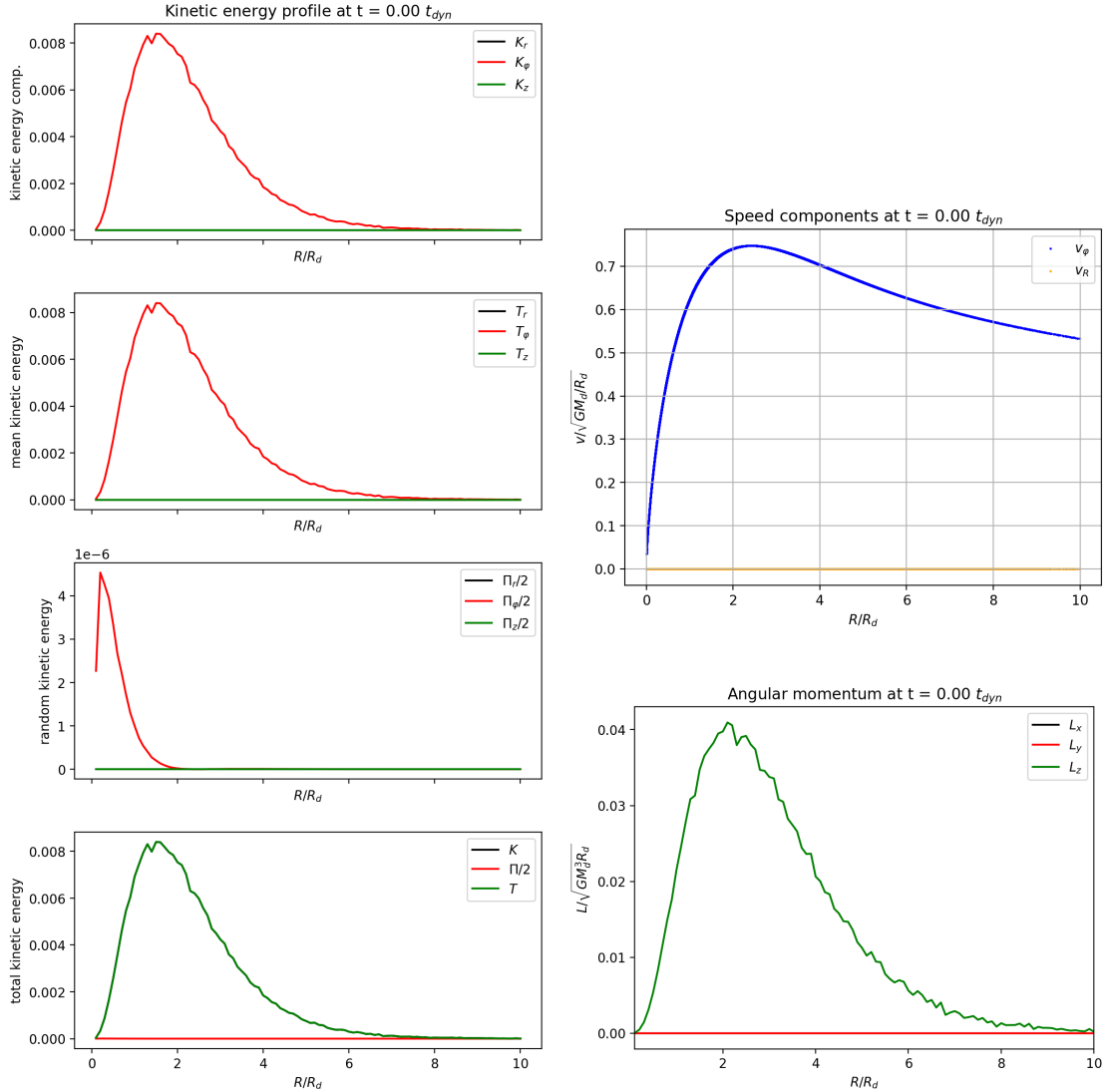


Figure 4.15: Simulation  $M_h4a_h5\alpha0$ . (Left) Initial profiles of the kinetic energy components. Radii and energies are normalized to  $R_d$  and  $GM_d^2/R_d$ , respectively. (Top right) Initial rotation velocity of particles.  $R$  is normalized to  $R_d$ , while the  $\mathbf{v}$ -components are normalized to  $(GM_d/R_d)^{1/2}$ . (Bottom right) Initial profiles of the angular momentum components.  $R$  and all the  $\mathbf{L}$ -components are normalized to  $R_d$  and  $(GM_d^3 R_d)^{1/2}$ , respectively.

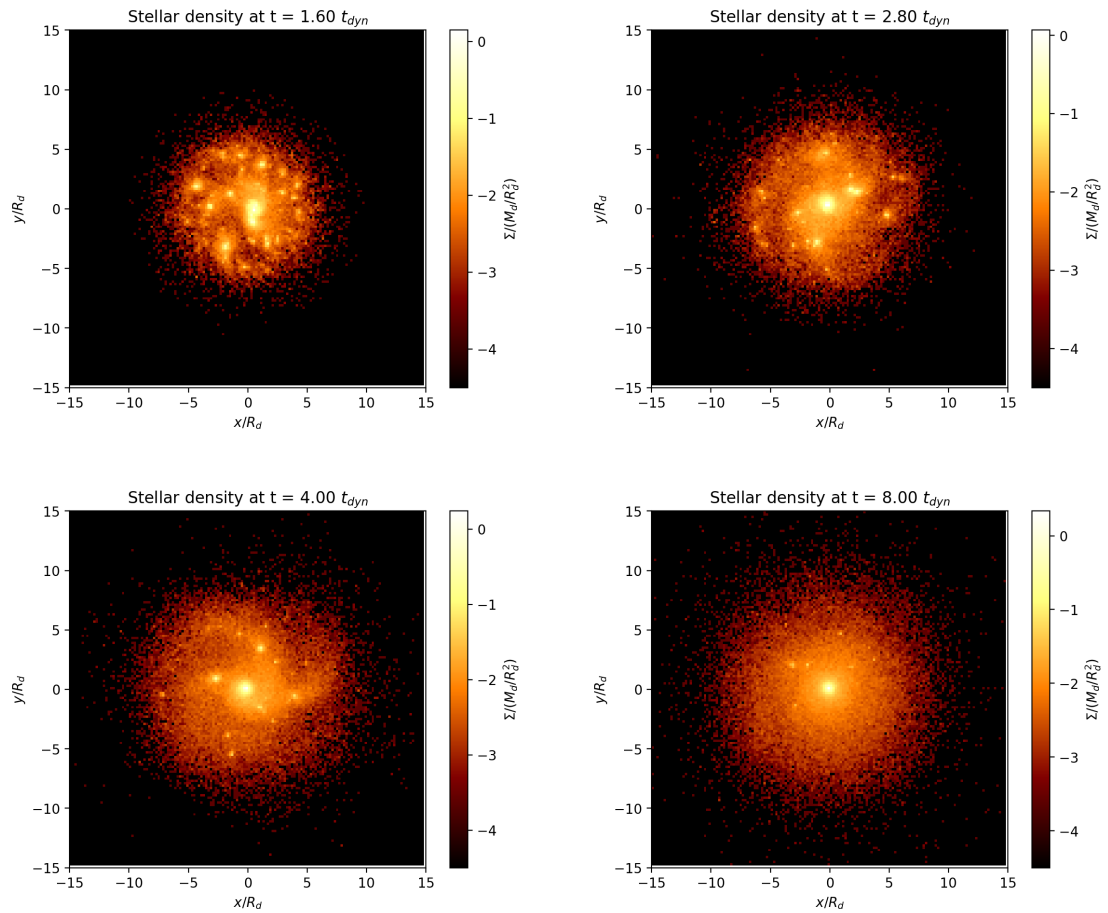


Figure 4.16: Simulation  $M_h 4 a_h 5 \alpha 0$ . Evolution of the disc density map of the  $(x, y)$  plane with time.  $x$  and  $y$  axes are normalized to  $R_d$ , while  $\Sigma$  (colour bar) is normalized to  $M_d/R_d^2$ .

After few dynamical times, the disc reveals denser region in the centre, which are more concentrated in an elongated shape, which we might call a weak bar. This behaviour is also confirmed by the evolution of the  $m = 2$  modes through the time – see Figure 4.17, left –, which are greater than  $A_2/A_0 = 0.1$  within  $5t_{dyn}$ .  $m = 2$  modes are a signal for the presence of a bar pattern, which is slightly present within  $8t_{dyn}$ . After that time, the bar pattern loses its coherence and eventually vanishes, leading to a more symmetrical structure whose size is bigger than the initial one. We stress that the rise of  $m = 2$  can be due to both the presence of spirals of a bar inside the disc. The half-mass radius, shown in Figure 4.17 (right), is also evolving in time, but it keep the same value after  $t \sim 7t_{dyn}$ .

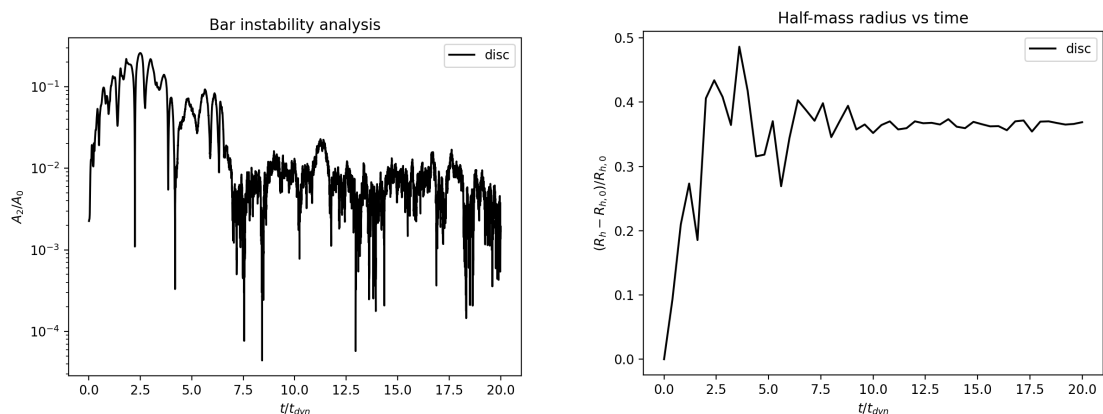


Figure 4.17: Simulation  $M_h4a_h5\alpha0$ . (Left) Evolution of the bar amplitude  $A_2/A_0$  with time. (Right) Evolution of the fractional variation of the half-mass radius with time. Time is normalized to  $t_{dyn}$ .

Another consequence of the evolution of the disc is that its surface density profile changes during the time: in fact, the growing of the disc size changes the spatial distribution of the stars. At the final stage of the simulation ( $t \sim 8t_{dyn}$ ), the new surface density profile shows a cusp in the centre of the disc and a cut-off at large radius – see Figures 4.18.

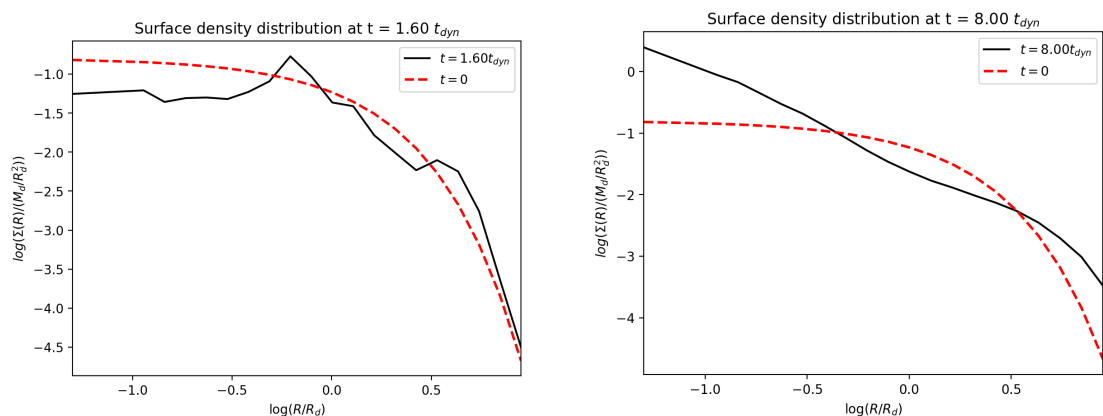


Figure 4.18: Simulation  $M_h4a_h5\alpha0$ . Disc surface density profile (black) at  $t = 1.6t_{dyn}$  (left) and  $t = 8t_{dyn}$  (right) compared to the initial one (dashed red).  $R$  and  $\Sigma(R)$  are normalized to  $R_d$  and  $M_d/R_d^2$ , respectively.

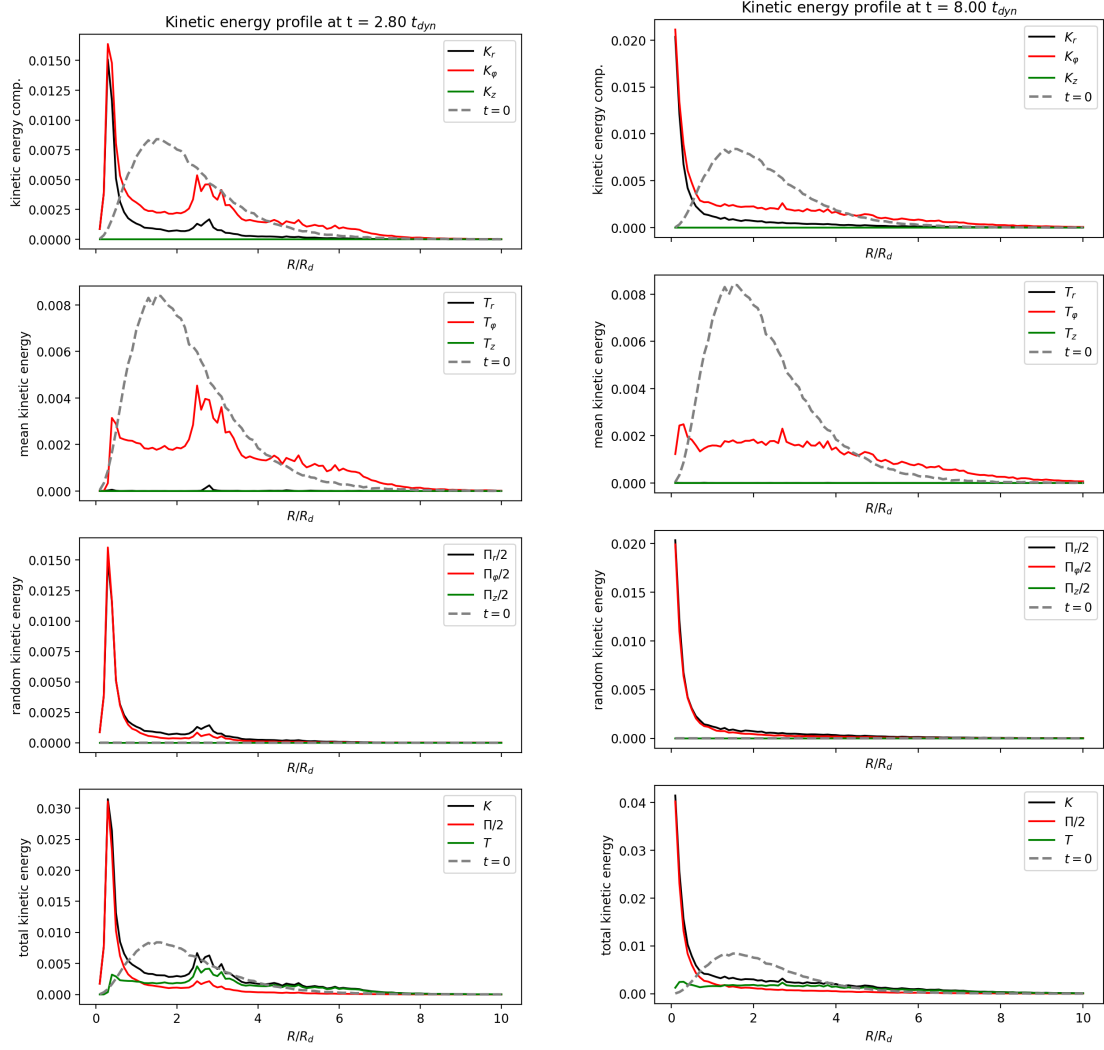


Figure 4.19: Simulation  $M_h4a_h5a0$ . Evolution of the kinetic energy components with time, compared to the initial profile (dashed gray line). Radii and energies are normalized to  $R_d$  and  $GM_d^2/R_d$ , respectively.

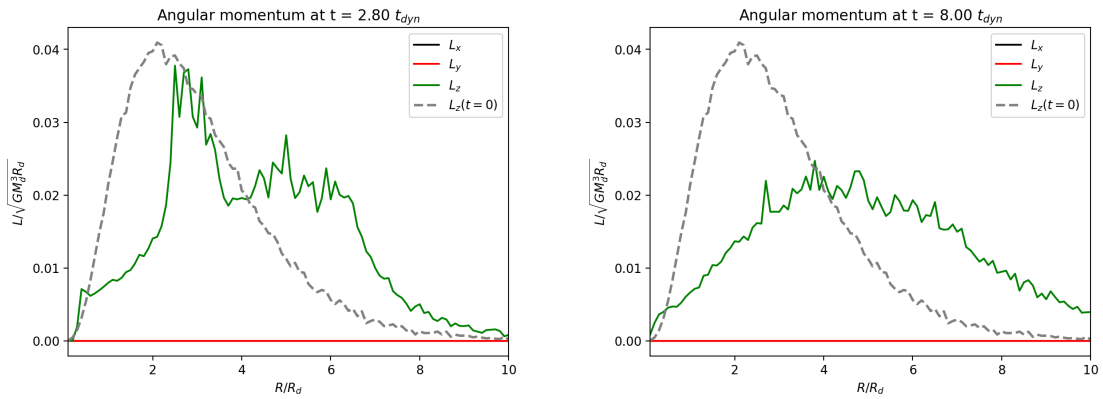


Figure 4.20: Simulation  $M_h4a_h5a0$ . Evolution of the angular momentum components with time, compared to the initial profile (dashed gray line).  $R$  and all the  $\mathbf{L}$ -components are normalized to  $R_d$  and  $(GM_d^3 R_d)^{1/2}$ , respectively.

The kinetic energy components also change during the simulation. The ordered motion  $T$  are totally given by the azimuthal component  $T_\varphi$ , while the random component has both radial and azimuthal contributions. After few dynamical times, the initial speed profile is no longer present and, during the slight formation of the bar at  $2.8t_{dyn}$  (Figure 4.19, left), we can see two peaks in ordered and random motions in the central regions of the disc. We notice that random motions are more significant in the innermost regions, while ordered motions are preponderant the peak between  $2 < R/R_d < 4$ . After the bar dissolution, at  $t = 8t_{dyn}$  (Figure 4.19, right) this latter peak vanishes, but the random motions in the innermost regions hold on. As in the  $2.8t_{dyn}$  snapshot, the ordered motions are prevalent starting from  $R/R_d = 2$ . In both these snapshots, azimuthal motions are the main component of the stellar kinetic energy.

The analysis of the angular momentum evolution with time gives more information about the kinetic energy peak at  $t = 2.8t_{dyn}$  in the region  $2 < R/R_d < 4$ . From Figure 4.20 (left) we can see that the above-mentioned peak is also represented by a peak in  $L_z$ , the only non-null component of the angular momentum of the disc. This peak is erased after the bar dissolution (Figure 4.20, right) and most of the  $L_z$  contribution, comparing to the initial profile, is translated outside of the disc.

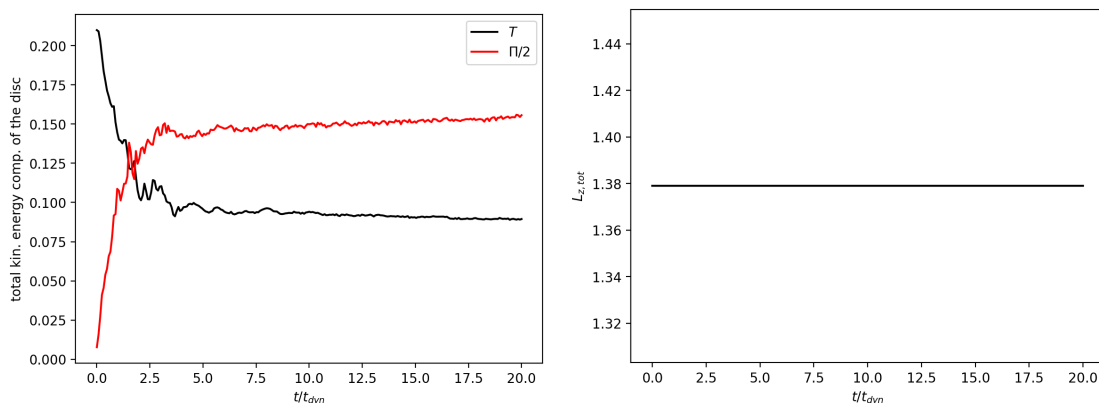


Figure 4.21: Simulation  $M_h4a_h5\alpha0$ . (Left) Evolution of the total ordered and random kinetic energies  $T$  and  $\Pi$  with time. Radii and energies are normalized to  $R_d$  and  $GM_d^2/R_d$ , respectively. (Right) Evolution of the total angular momentum  $L_{z,tot}$  with time.  $R$  and  $L_{z,tot}$  are normalized to  $R_d$  and  $(GM_d^3R_d)^{1/2}$ , respectively.

Focusing now on the the total ordered kinetic energy  $T$  and on the total random kinetic energy  $\Pi$  of the disc, they evolve in this scenario, but after  $t = 10t_{dyn}$  their change becomes less significant (see Figure 4.21, left).  $T$  is predominant in the first  $2.5t_{dyn}$ , but then random motions are the principal kinetic energy component of the systems, even though the ordered motions are still significant over time. Figure 4.21 (right) shows that  $L_{z,tot}$  is well conserved in the subsequent times.

#### 4.4.2 Simulation $M_h4a_h5\alpha0.5$ ( $M_h/M_d = 4$ , $a_h/R_d = 5$ , $\alpha = 0.5$ )

##### Initial conditions and parameters

For the initial mass distribution of the disc particles, see Figures 3.1, 3.2, 3.3, and 4.1. The initial rotation curve of the particles, the initial kinetic energy and angular momentum distributions are shown in Figures 4.22.

Name	§	$\frac{M_h}{M_d}$	$\frac{a_h}{R_d}$	$t_{dyn}/t_u$	$\alpha$	$t_{OP}$	$t^*$	$t_W$	stable
$M_h4a_h5\alpha0.5$	4.4.2	4	5	14.58	1/2	0	0	0	No

Table 4.5: Summary table of the simulation  $M_h4a_h5\alpha0.5$ . All the input parameters are explained in the caption of Table 4.1.

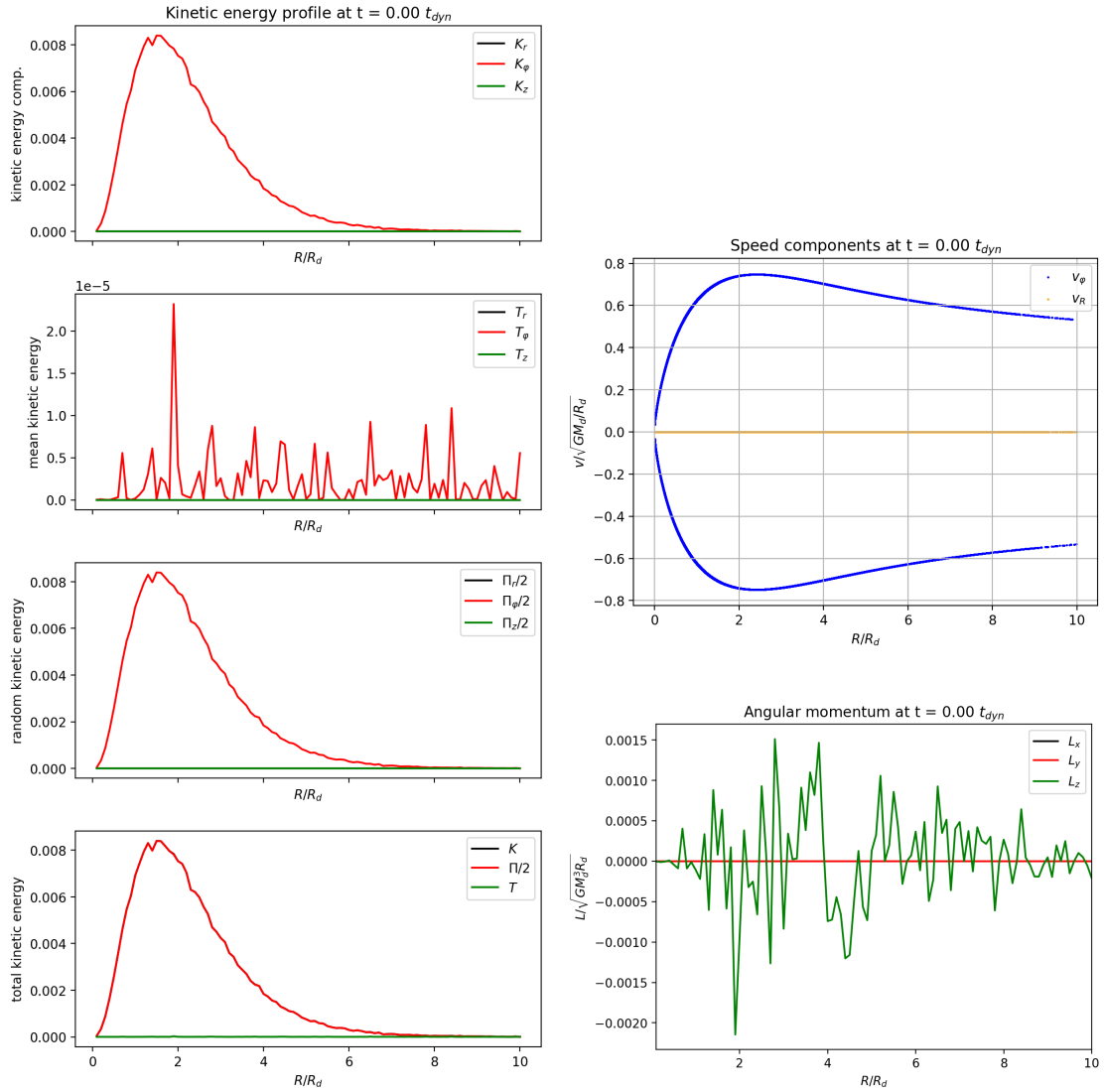


Figure 4.22: Simulation  $M_h4a_h5\alpha0.5$ . (Left) Initial profiles of the kinetic energy components. Radii and energies are normalized to  $R_d$  and  $GM_d^2/R_d$ , respectively. (Top right) Initial rotation velocity of particles.  $R$  is normalized to  $R_d$ , while the  $\mathbf{v}$ -components are normalized to  $(GM_d/R_d)^{1/2}$ . (Bottom right) Initial profiles of the angular momentum components.  $R$  and all the  $\mathbf{L}$ -components are normalized to  $R_d$  and  $(GM_d^3 R_d)^{1/2}$ , respectively.

## Results

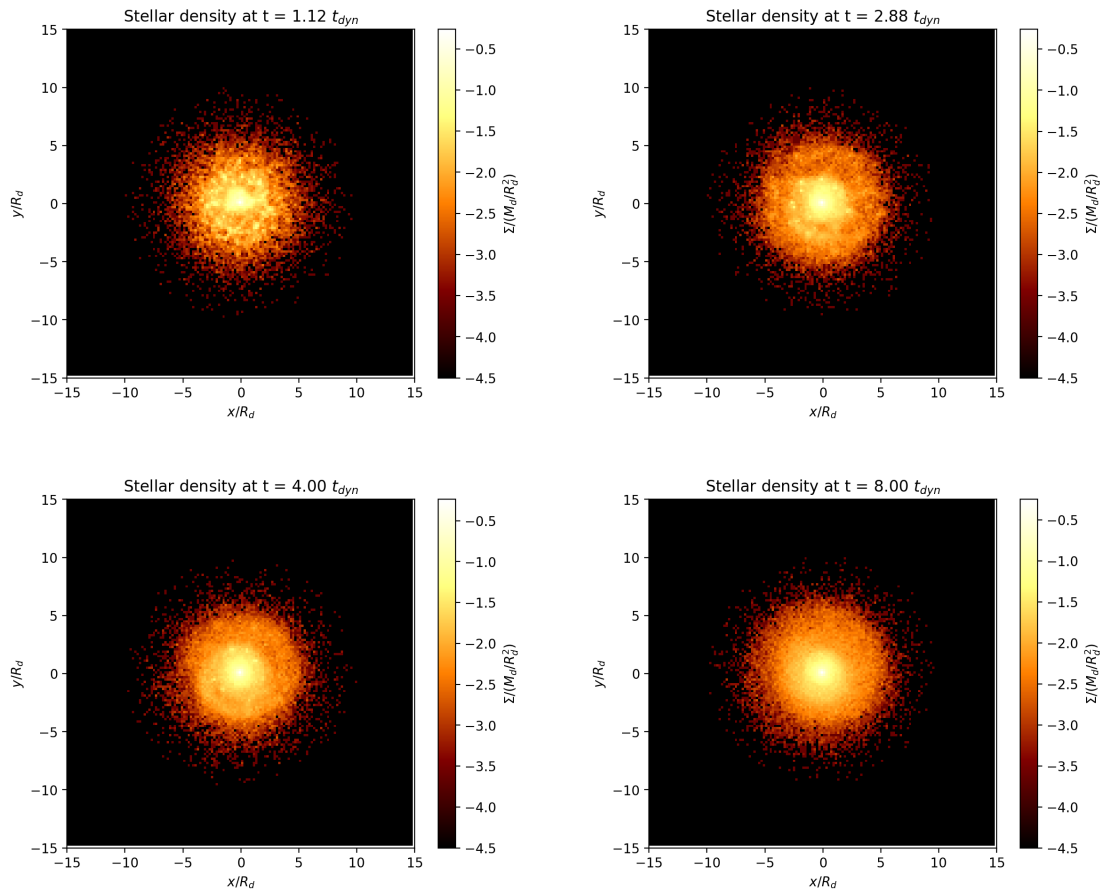


Figure 4.23: Simulation  $M_h 4a_h 5\alpha 0.5$ . Evolution of the disc density map of the  $(x, y)$  plane with time.  $x$  and  $y$  axes are normalized to  $R_d$ , while  $\Sigma$  (colour bar) is normalized to  $M_d/R_d^2$ .

In presence a fraction  $\alpha = 0.5$  of retrograde orbits – i.e., before starting the simulation, we invert half of the stellar orbits –, the results are totally different from that seen in Section 4.4.1. As we can notice from the density maps in Figures 4.23, no apparent bar is forming during the evolution of the disc, even though the  $A_2/A_0$  ratio (see Figure 4.24, left) has a peak at  $t \sim 1t_{dyn}$ , slightly lower than  $A_2/A_0 = 0.1$ . This is due to the fact that there is a phase of readjustment of the initial conditions, which are undergoing local instabilities. After  $t \sim 2t_{dyn}$ , the disc develops a more concentrated centre and a ring-like structure which is surrounding it. The  $m = 2$  modes are always of the order of  $A_2/A_0 \sim 10^{-2} \div 10^{-3}$ , which confirms the absence of a bar in this system. Not only the disc is stable to bar formation, but it also keeps roughly the same size from the initial conditions. In the final stage ( $t \sim 8t_{dyn}$ ), the disc has a size 5% more extended with respect to the initial one and the external ring structure is vanishing.

Considering that the disc, thanks to the azimuthal velocity dispersion, is deviating little from of its initial conditions, we expect quite the same in the surface density profile. In fact, the only departure from initial conditions is given by the central cusp that forms after few dynamical times, as we can see from Figures 4.25.

The kinetic energy components show no substantial change during the whole simulation. The azimuthal motions are always prevailing with respect to the radial motions.

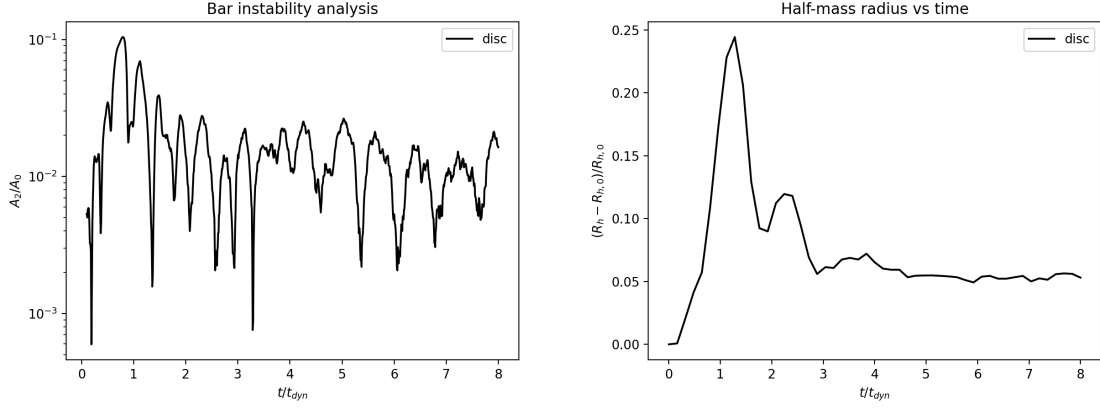


Figure 4.24: Simulation  $M_h 4a_h 5\alpha 0.5$ . (Left) Evolution of the bar amplitude  $A_2/A_0$  with time. (Right) Evolution of the fractional variation of the half-mass radius with time. Time is normalized to  $t_{dyn}$ .

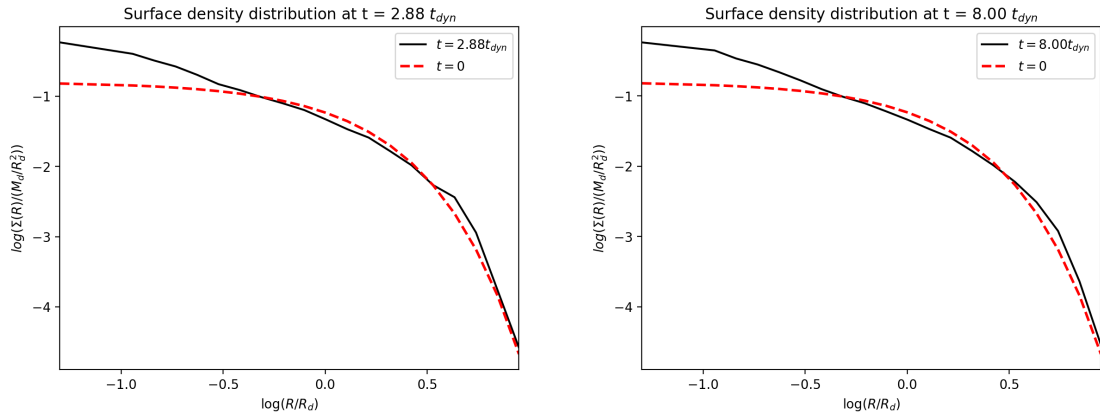


Figure 4.25: Simulation  $M_h 4a_h 5\alpha 0.5$ . Disc surface density profile (black) at  $t = 2.88t_{dyn}$  (left) and  $t = 8t_{dyn}$  (right) compared to the initial one (dashed red).  $R$  and  $\Sigma(R)$  are normalized to  $R_d$  and  $M_d/R_d^2$ , respectively.

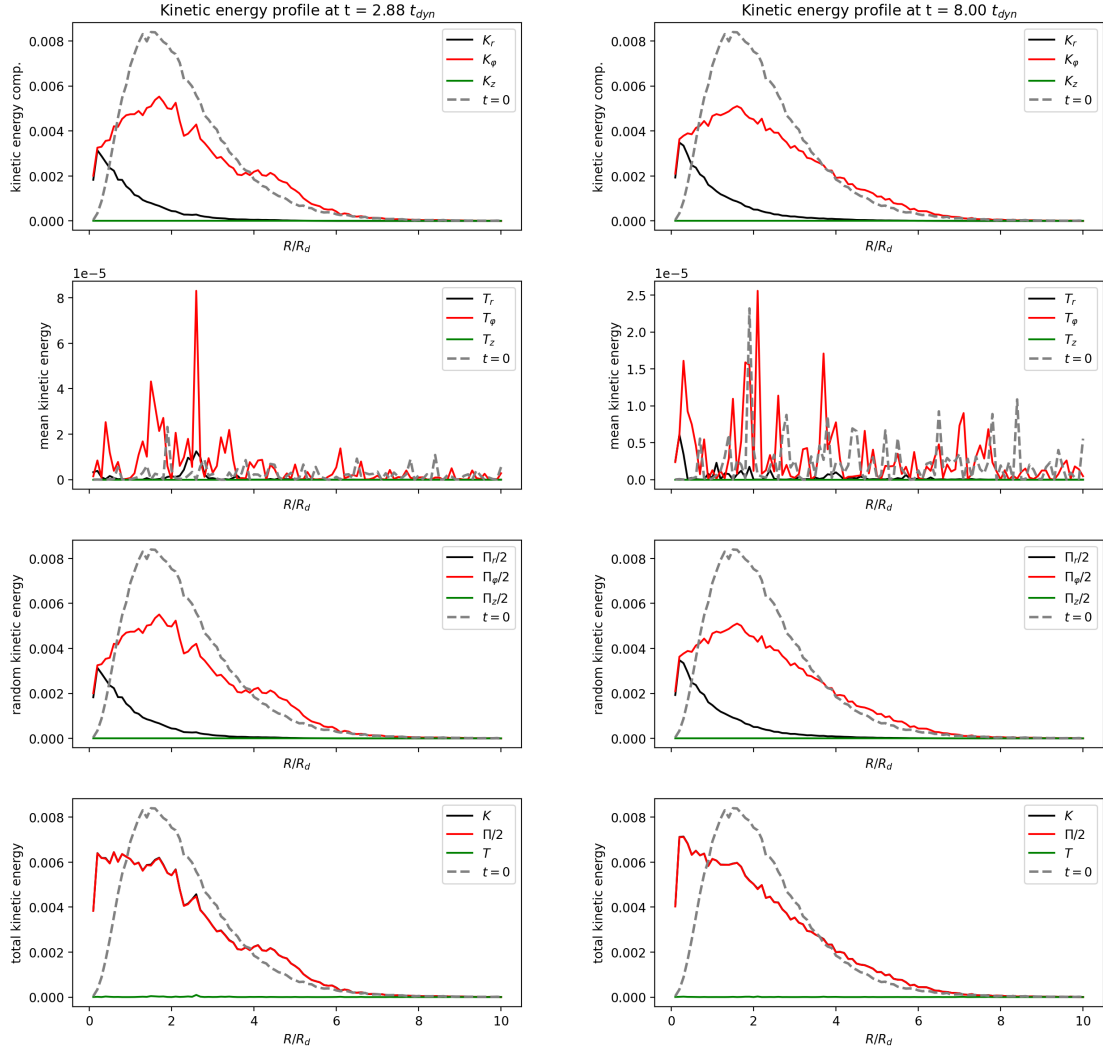


Figure 4.26: Simulation  $M_h4a_h5\alpha0.5$ . Evolution of the kinetic energy components with time, compared to the initial profile (dashed gray line). Radii and energies are normalized to  $R_d$  and  $GM_d^2/R_d$ , respectively.

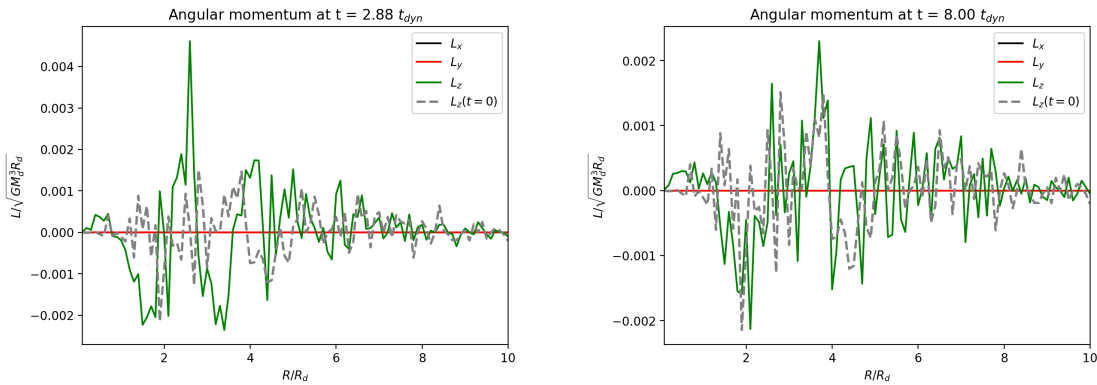


Figure 4.27: Simulation  $M_h4a_h5\alpha0.5$ . Evolution of the angular momentum components with time, compared to the initial profile (dashed gray line).  $R$  and all the  $\mathbf{L}$ -components are normalized to  $R_d$  and  $(GM_d^3 R_d)^{1/2}$ , respectively.

In particular, the latter have a peak in the innermost regions, where it has the same value of the azimuthal kinetic energy. The ordered motions  $T$  are negligible in the whole simulation, leading to totally prevalent random motions, which seem to prevent bar formation in the central regions. At the end of the simulation, even though the disc has different features with respect to the initial conditions, it keeps barely the the same features during within  $8t_{dyn}$  (Figure 4.26, left), forming a cusp at the centre.

As a consequence from the absence of negligible kinetic energy (Figures 4.26), the angular momentum (Figure 4.27), only represented by  $L_z$ , is approaching to a null value:  $|L_z| < 0.004$ , which has to be compared to the angular momentum of the same simulation with  $\alpha = 0$  (Section 4.4.1, Figures 4.20), where the peak was at least five times bigger than in this case.

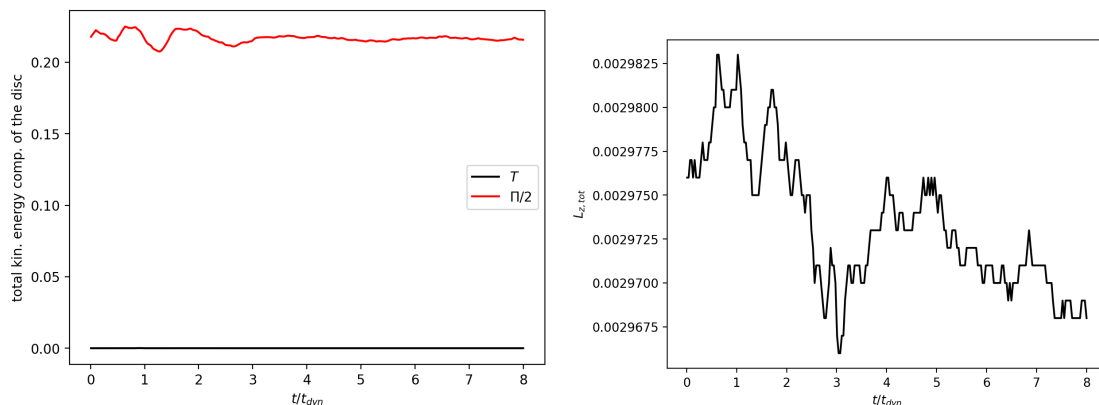


Figure 4.28: Simulation  $M_h 4a_h 5\alpha 0.5$ . (Left) Evolution of the total ordered and random kinetic energies  $T$  and  $\Pi$  with time. Radii and energies are normalized to  $R_d$  and  $GM_d^2/R_d$ , respectively. (Right) Evolution of the total angular momentum  $L_{z,tot}$  with time.  $R$  and  $L_{z,tot}$  are normalized to  $R_d$  and  $(GM_d^3 R_d)^{1/2}$ , respectively.

Similarly to the simulation  $M_h 0a_h 0\alpha 0.5$ , the total ordered kinetic energy of the disc  $T$  is keeping null for the simulation run, while the total random kinetic energy  $\Pi$  keeps barely constant with time after some initial fluctuations before  $t = 3t_{dyn}$  (see Figure 4.28, left). The behaviour of  $\Pi$  is different to the  $M_h 4a_h 5\alpha 0$  case and can be related to the less presence of instabilities (both local and global). Figure 4.28 (right) shows that  $L_{z,tot}$  is varying at small scales as in the simulation  $M_h 0a_h 0\alpha 0.5$ .

#### 4.4.3 Simulation $M_h 10a_h 5\alpha 0$ ( $M_h/M_d = 10$ , $a_h/R_d = 5$ , $\alpha = 0$ )

##### Initial conditions and parameters

Name	§	$\frac{M_h}{M_d}$	$\frac{a_h}{R_d}$	$t_{dyn}/t_u$	$\alpha$	$t_{OP}$	$t^*$	$t_W$	stable
$M_h 10a_h 5\alpha 0$	4.4.2	10	5	12.18	0	0.063	0.228	0.5	No

Table 4.6: Summary table of the simulation  $M_h 10a_h 5\alpha 0$ . All the input parameters are explained in the caption of Table 4.1.

For the initial mass distribution of the disc particles, see Figures 3.1, 3.2, 3.3, and 4.1. The initial rotation curve of the particles, the initial kinetic energy and angular momentum distributions are shown in Figures 4.29.

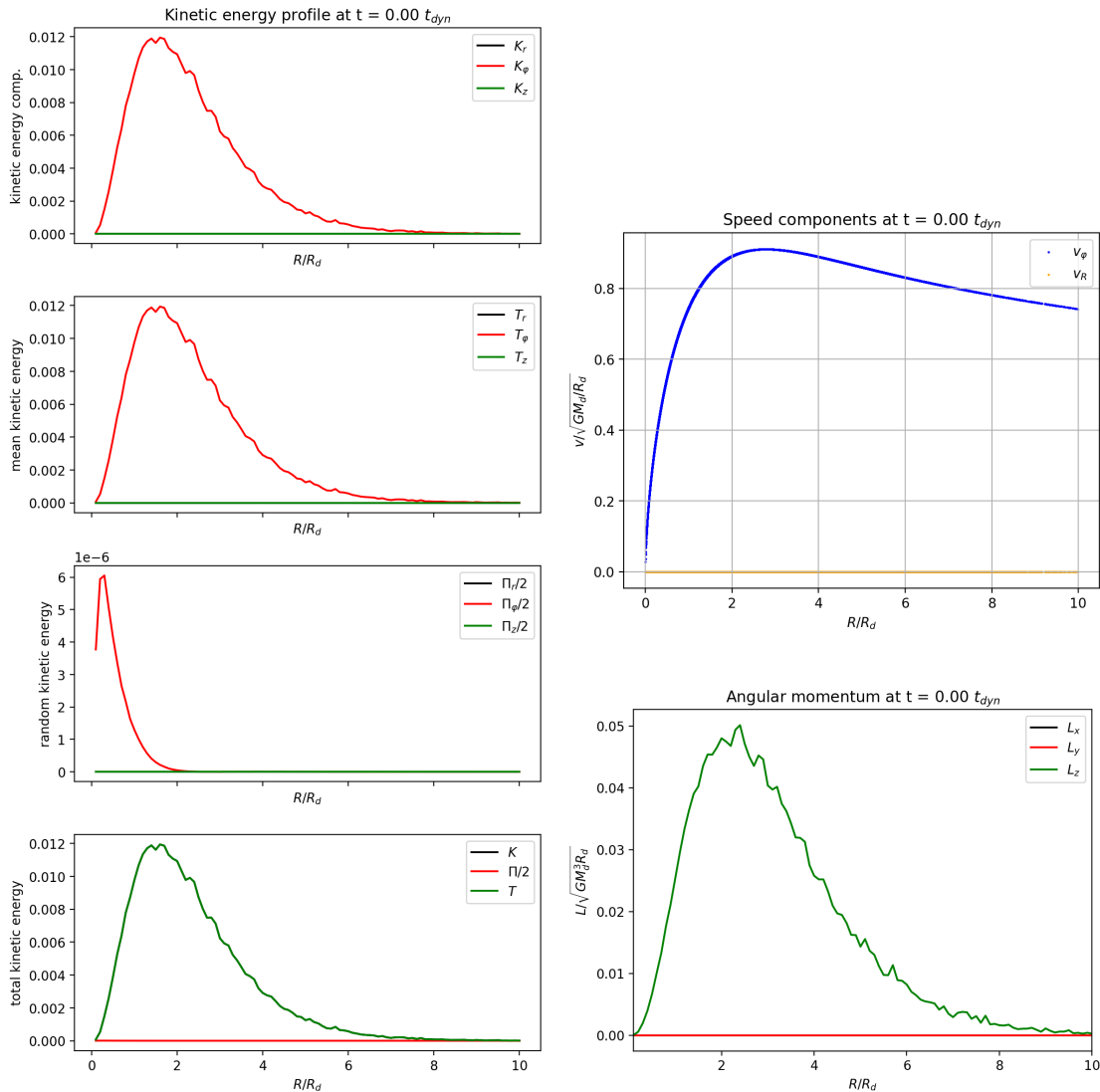


Figure 4.29: Simulation  $M_h 10 a_h 5 \alpha 0$ . (Left) Initial profiles of the kinetic energy components. Radii and energies are normalized to  $R_d$  and  $GM_d^2/R_d$ , respectively. (Top right) Initial rotation velocity of particles.  $R$  is normalized to  $R_d$ , while the  $\mathbf{v}$ -components are normalized to  $(GM_d/R_d)^{1/2}$ . (Bottom right) Initial profiles of the angular momentum components.  $R$  and all the  $\mathbf{L}$ -components are normalized to  $R_d$  and  $(GM_d^3 R_d)^{1/2}$ , respectively.

## Results

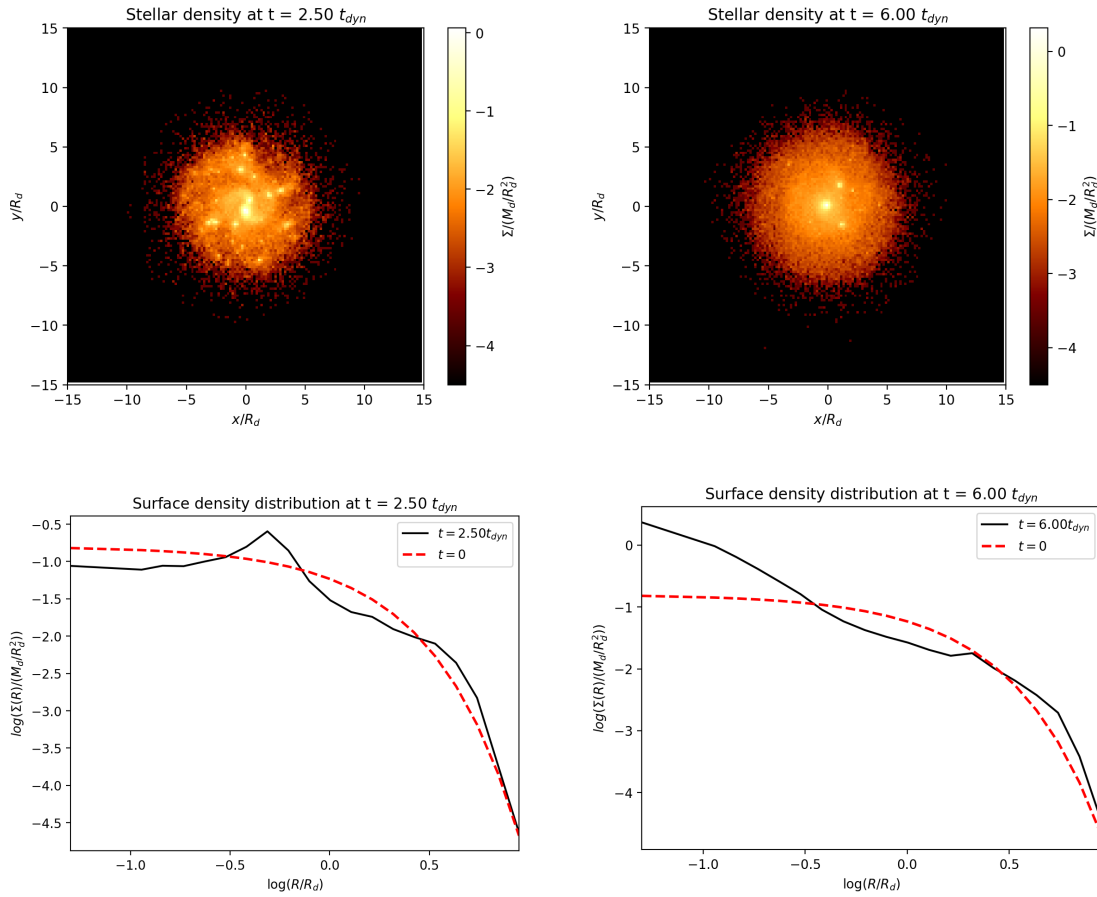


Figure 4.30: Simulation  $M_h 10 a_h 5 \alpha 0$ . (Top) Disc density map of the  $(x, y)$  plane at  $t = 10 t_{dyn}$ .  $x$  and  $y$  axes are normalized to  $R_d$ , while  $\Sigma$  (colour bar) is normalized to  $M_d/R_d^2$ . (Bottom) Disc surface density profile (black) at  $t = 2.5 t_{dyn}$  (left) and  $t = 6 t_{dyn}$  (right) compared to the initial one (dashed red).  $R$  and  $\Sigma(R)$  are normalized to  $R_d$  and  $M_d/R_d^2$ , respectively.

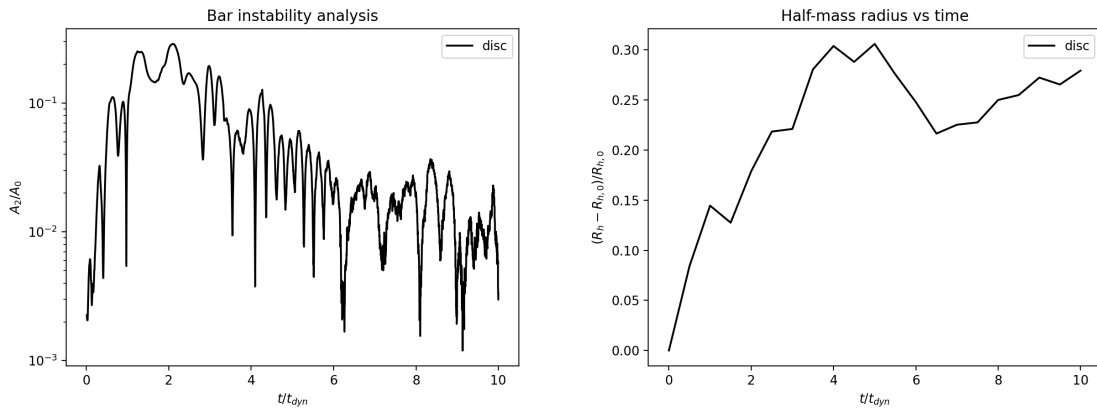


Figure 4.31: Simulation  $M_h 10 a_h 5 \alpha 0$ . (Left) Evolution of the bar amplitude  $A_2/A_0$  with time. (Right) Evolution of the fractional variation of the half-mass radius with time. Time is normalized to  $t_{dyn}$ .

By increasing the halo mass at  $M_h/M_d = 10$  (maintaining  $a_h/R_d = 5$ ), the prevention of a global instability in the disc is still far away: as we can see in Figures 4.30, both the density maps and the surface density distribution are changing with time, forming local instabilities (e.g., Jeans, 1902; Toomre, 1964). In particular, at  $t = 2.5t_{dyn}$  we can notice the formation of a weak bar at the centre of the disc, which disappears at  $t = 6t_{dyn}$ . The presence of a weak bar is confirmed also by the behaviour of the  $m = 2$  modes (Figure 4.31, left), which are  $A_2/A_0 > 10^{-1}$  for  $1 < t/t_{dyn} < 3$ . At the end of the simulation (Figure 4.30, top right), the local inhomogeneity is no longer present, leading to a smoother density distribution with an increased half-mass radius (Figure 4.31, right).

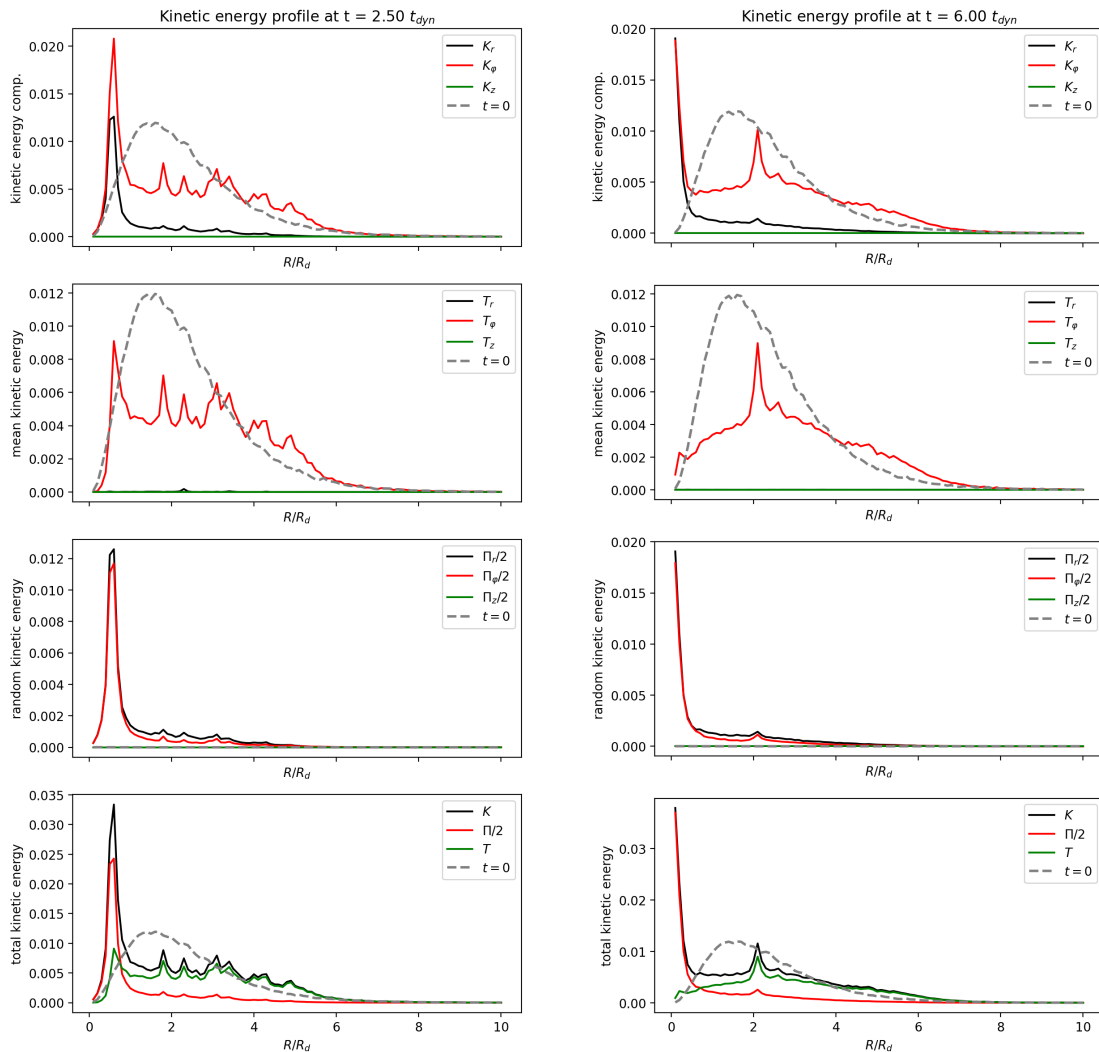


Figure 4.32: Simulation  $M_h 10 a_h 5 \alpha 0$ . Evolution of the kinetic energy components with time, compared to the initial profile (dashed gray line). Radii and energies are normalized to  $R_d$  and  $GM_d^2/R_d$ , respectively.

If we look at the kinetic energies (Figures 4.32), we see that the random motions (both radial and azimuthal) are mainly present in the innermost regions of the disc, while the ordered motions (only made by the azimuthal component) give a primary contribution in the regions  $R/R_d \gtrsim 1$ . The inner  $K$ -spike at  $t = 2.5t_{dyn}$  (Figure 4.32, left) is given by the presence of a denser region in the surrounding area, as also confirmed in Figure 4.32 (right) at  $t = 6t_{dyn}$ . At this latter time, a second spike at

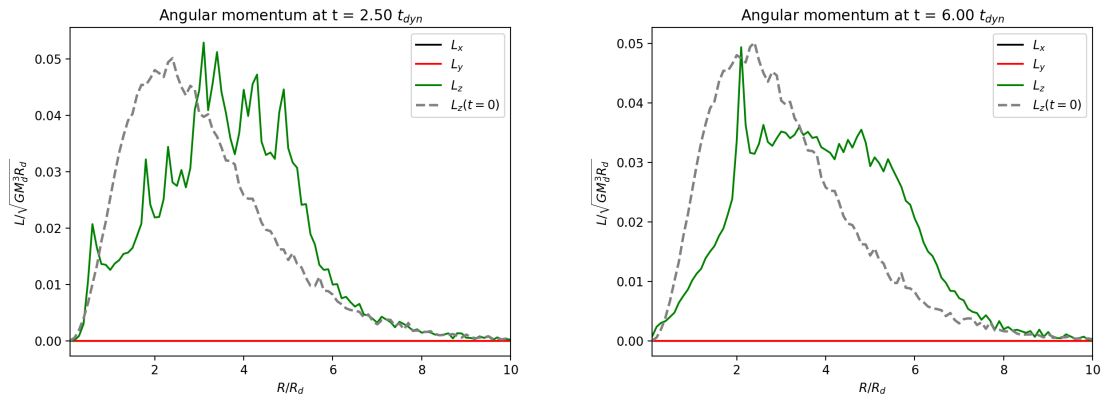


Figure 4.33: Simulation  $M_h10a_h5\alpha0$ . Evolution of the angular momentum components with time, compared to the initial profile (dashed gray line).  $R$  and all the  $L$ -components are normalized to  $R_d$  and  $(GM_d^3 R_d)^{1/2}$ , respectively.

$R/R_d \simeq 2$  is formed, probably related to the local overdensities at that distance from the centre.

The distribution of the angular momentum at  $t = 2.5t_{dyn}$  and at  $t = 6t_{dyn}$  is different from the initial one (Figure 4.29, bottom right). In particular, at  $t = 2.5t_{dyn}$  the region  $3 < R/R_d < 6$  has a higher angular momentum than in the innermost zones, but the latter show less angular momentum for increasing time. At  $t = 6t_{dyn}$  we can see the same spike at  $R/R_d \simeq 2$  we have noticed in Figure 4.32 (right).

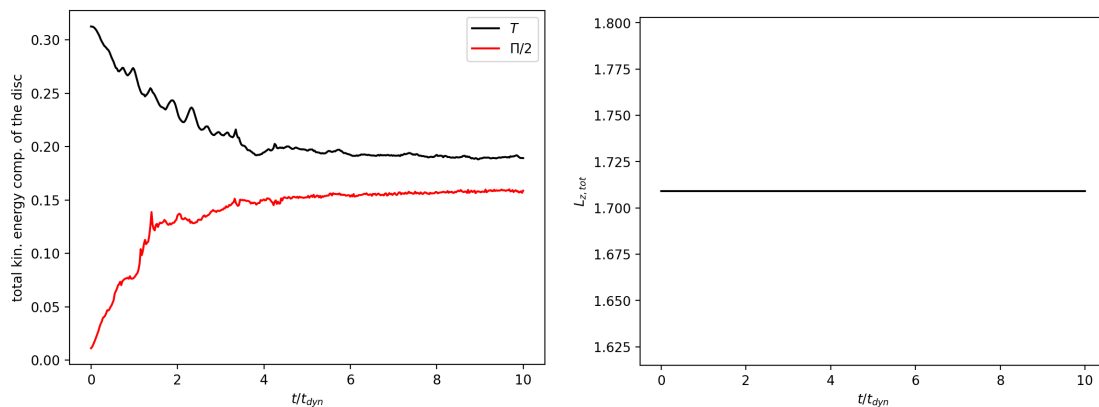


Figure 4.34: Simulation  $M_h10a_h5\alpha0$ . (Left) Evolution of the total ordered and random kinetic energies  $T$  and  $\Pi$  with time. Radii and energies are normalized to  $R_d$  and  $GM_d^2/R_d$ , respectively. (Right) Evolution of the total angular momentum  $L_{z,tot}$  with time.  $R$  and  $L_{z,tot}$  are normalized to  $R_d$  and  $(GM_d^3 R_d)^{1/2}$ , respectively.

For this simulation run, the total ordered kinetic energy of the disc  $T$  decreases but seems to approach an asymptotic value, as well as the random motions  $\Pi$  are increasing with time and are asymptotically reaching a constant value (see Figure 4.34, left). The change of both  $T$  and  $\Pi$  manifests the instability of this disc-halo system. Also in this case, Figure 4.34 (right) shows that  $L_{z,tot}$  is conserved during all the simulation run time.

#### 4.4.4 Simulation $M_h400a_h5\alpha0$ ( $M_h/M_d = 400$ , $a_h/R_d = 5$ , $\alpha = 0$ )

##### Initial conditions and parameters

Name	§	$\frac{M_h}{M_d}$	$\frac{a_h}{R_d}$	$t_{dyn}/t_u$	$\alpha$	$t_{OP}$	$t^*$	$t_W$	stable
$M_h400a_h5\alpha0$	4.4.2	400	5	2.68	0	0.001	0.01	0.5	Yes

Table 4.7: Summary table of the simulation  $M_h400a_h5\alpha0$ . All the input parameters are explained in the caption of Table 4.1.

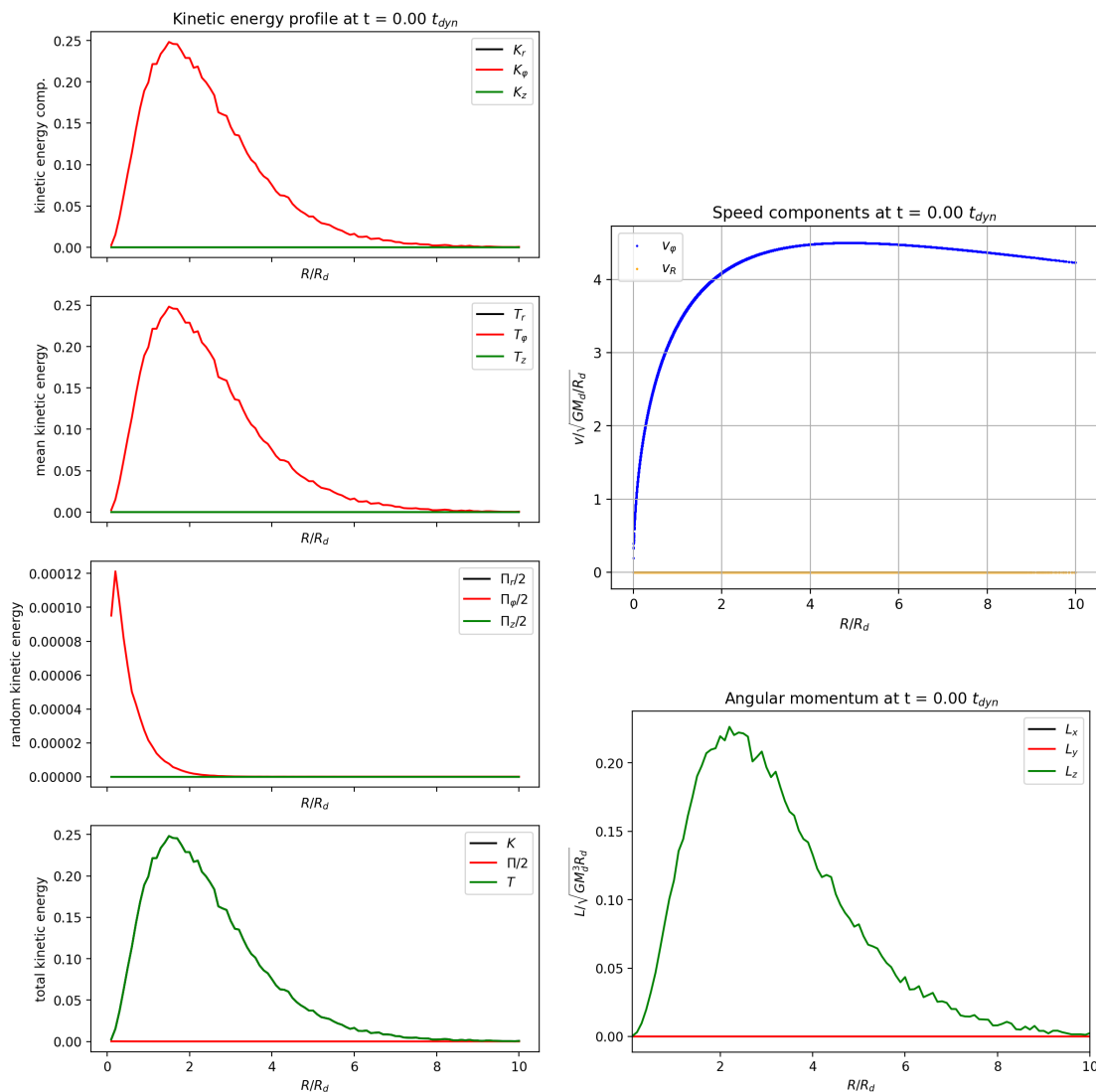


Figure 4.35: Simulation  $M_h400a_h5\alpha0$ . (Left) Initial profiles of the kinetic energy components. Radii and energies are normalized to  $R_d$  and  $GM_d^2/R_d$ , respectively. (Top right) Initial rotation velocity of particles.  $R$  is normalized to  $R_d$ , while the  $\mathbf{v}$ -components are normalized to  $(GM_d/R_d)^{1/2}$ . (Bottom right) Initial profiles of the angular momentum components.  $R$  and all the  $\mathbf{L}$ -components are normalized to  $R_d$  and  $(GM_d^3 R_d)^{1/2}$ , respectively.

For the initial mass distribution of the disc particles, see Figures 3.1, 3.2, 3.3, and

4.1. The initial rotation curve of the particles, the initial kinetic energy and angular momentum distributions are shown in Figures 4.35.

## Results

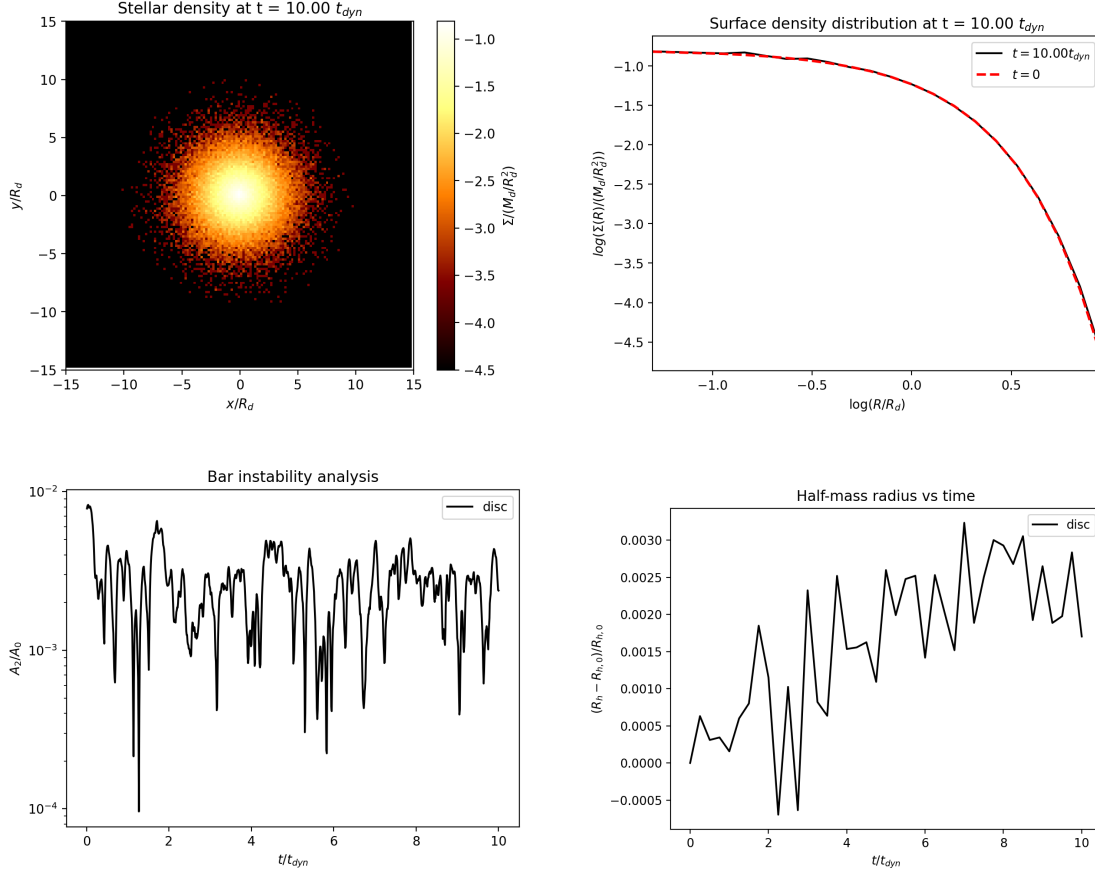


Figure 4.36: Simulation  $M_h 400 a_h 5 \alpha 0$ . (*Top left*) Disc density map of the  $(x, y)$  plane at  $t = 10 t_{dyn}$ .  $x$  and  $y$  axes are normalized to  $R_d$ , while  $\Sigma$  (colour bar) is normalized to  $M_d/R_d^2$ . (*Top right*) Disc surface density profile (black) at  $t = 10 t_{dyn}$  compared to the initial one (dashed red).  $R$  and  $\Sigma(R)$  are normalized to  $R_d$  and  $M_d/R_d^2$ , respectively. (*Bottom left*) Evolution of the bar amplitude  $A_2/A_0$  with time. (*Bottom right*) Evolution of the fractional variation of the half-mass radius with time. Time is normalized to  $t_{dyn}$ .

In the case of  $M_h/M_d = 400$ , the disc behaves essentially as a tracer with negligible self-gravity. In fact, all the particles are moving under the most prevalent potential field, which is, in this case, the halo one. The circular speed assigned to the disc particles follows Equation (3.25), but in the case of  $\Phi_h \gg \Phi_d$ , we have

$$v_c^2 \simeq R \frac{\partial \Phi_h}{\partial R}. \quad (4.26)$$

The disc particles are moving under the potential field of the halo and the disc, but the latter is negligible compared to the former, thus they behave almost as tracers of the halo potential. For this reason, at  $t = 10 t_{dyn}$  (Figure 4.36, top left) the system keeps its rotation with no signatures of instabilities and has the same initial surface density

profile (Figure 4.36, top right). The absence of a bar is confirmed by the  $m = 2$  modes plot (Figure 4.36, bottom left), where  $A_2/A_0 < 10^{-2}$  and the half-mass radius is quite unchanged (the relative variation computed using  $R_h(t)$  and  $R_h(t = 0)$  is of the order of  $10^{-3}$ ).

The angular momentum and the kinetic energy content conserve the initial properties (see Figures 4.37). Nevertheless, small random motions form in the innermost regions of the disc, even though the disc particles are moving under the main influence of the halo potential well. These random motions are negligible with respect to the ordered kinetic energy  $T$ , and can be ascribed to numerical noise.

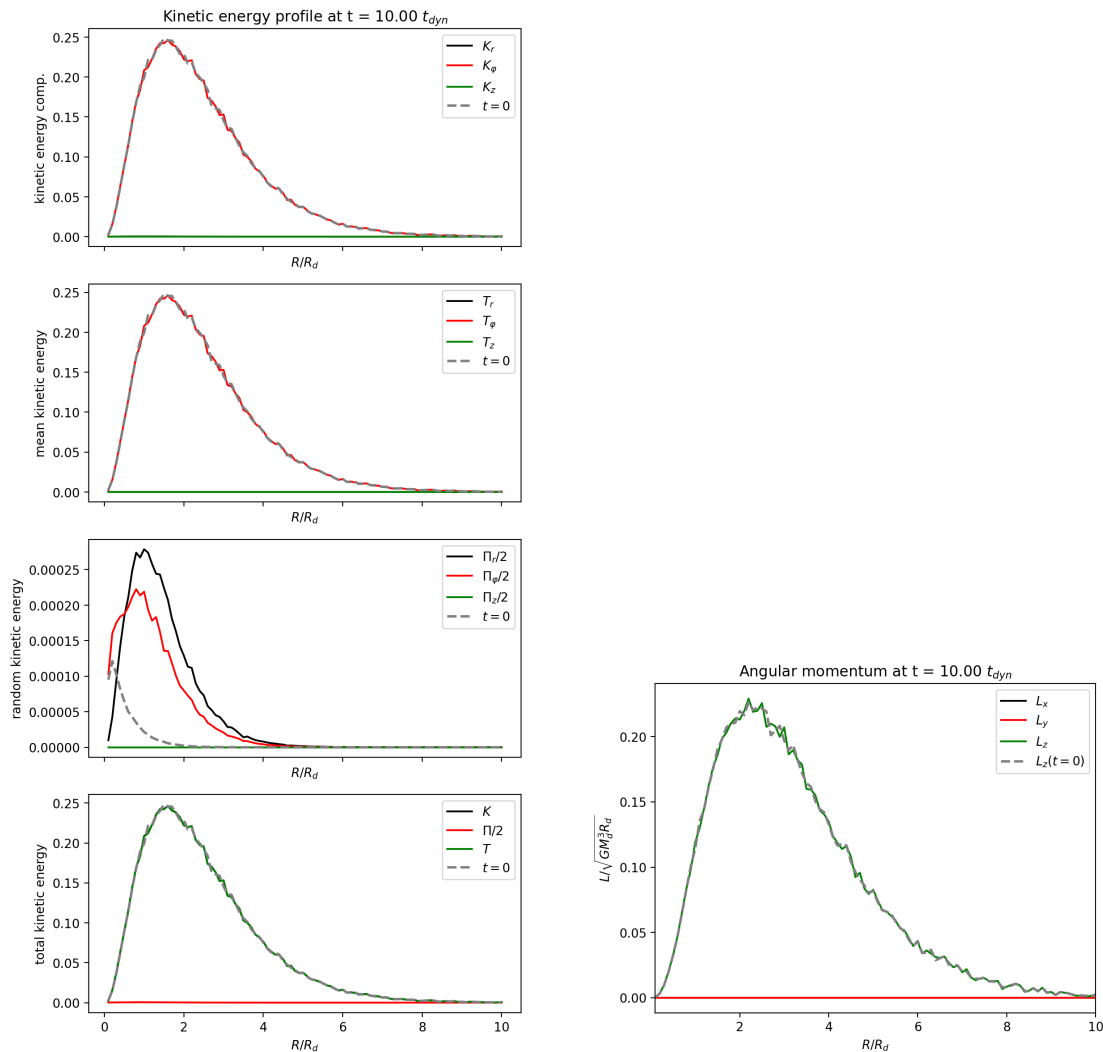


Figure 4.37: Simulation  $M_h 400 a_h 5 \alpha 0$ . (Left) Profiles of the kinetic energy components at  $t = 10 t_{dyn}$ . Radii and energies are normalized to  $R_d$  and  $GM_d^2/R_d$ , respectively. (Right) Profiles of the angular momentum components at  $t = 10 t_{dyn}$ .  $R$  and all the  $\mathbf{L}$ -components are normalized to  $R_d$  and  $(GM_d^3 R_d)^{1/2}$ , respectively.

As a confirm of our previous analysis, both the total ordered and random kinetic energies of the disc  $T$  and  $\Pi$  are not changing with time, in the absence of consistent fluctuations (see Figure 4.38, left). Figure 4.38 (right) displayed the same scenario with the total  $z$ -component of the angular momentum  $L_{z,tot}$ , which is conserved at a fixed value.

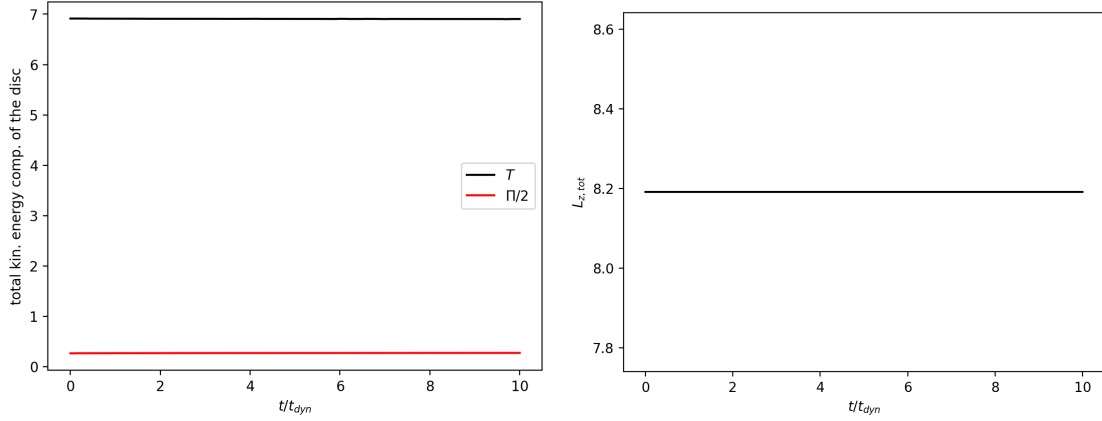


Figure 4.38: Simulation  $M_h400a_h5\alpha0$ . (Left) Evolution of the total ordered and random kinetic energies  $T$  and  $\Pi$  with time. Radii and energies are normalized to  $R_d$  and  $GM_d^2/R_d$ , respectively. (Right) Evolution of the total angular momentum  $L_{z,tot}$  with time.  $R$  and  $L_{z,tot}$  are normalized to  $R_d$  and  $(GM_d^3 R_d)^{1/2}$ , respectively.

## 4.5 Results on $t_{OP}$ , $t^*$ and $t_W$

After showing some of our simulations, we now focus on the behaviour of the stability indicators  $t_{OP}$ ,  $t^*$  and  $t_W$ , defined by Equations (2.7), (2.17) and (2.29), depending on the disc-halo initial configuration. In Figures 4.39, 4.40 and 4.41 we plot these parameters as functions of  $M_h/M_d$  and  $a_h/R_d$ , with  $\alpha = 0$ , for every simulation, highlighting stable and unstable systems.

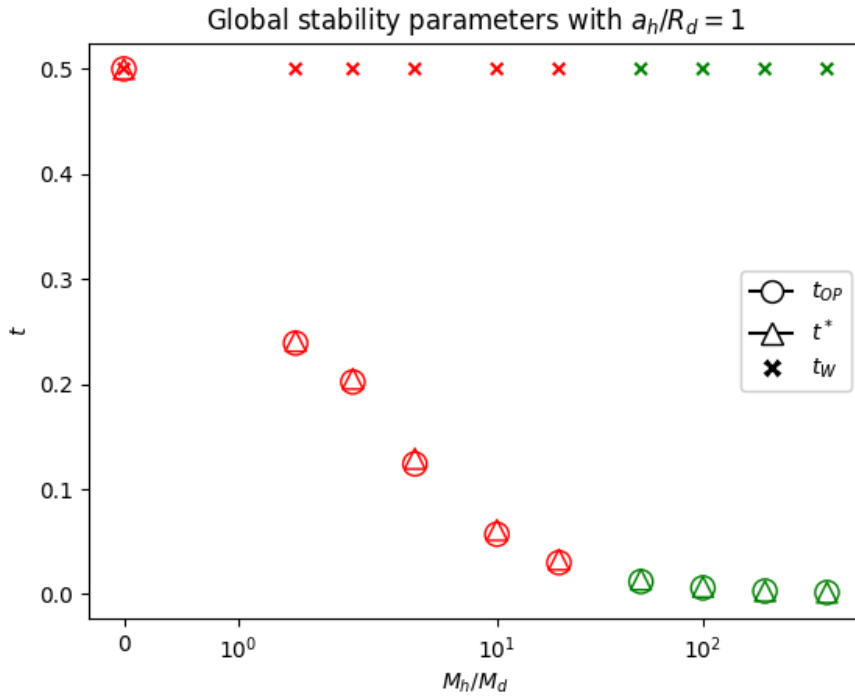


Figure 4.39: At  $t = 0$ ,  $t_{OP}$ ,  $t^*$  and  $t_W$  for all the simulations in Table 4.1 with  $a_h/R_d = 1$  and  $\alpha = 0$ . The colour green refers to stable discs, while the colour red to unstable discs.

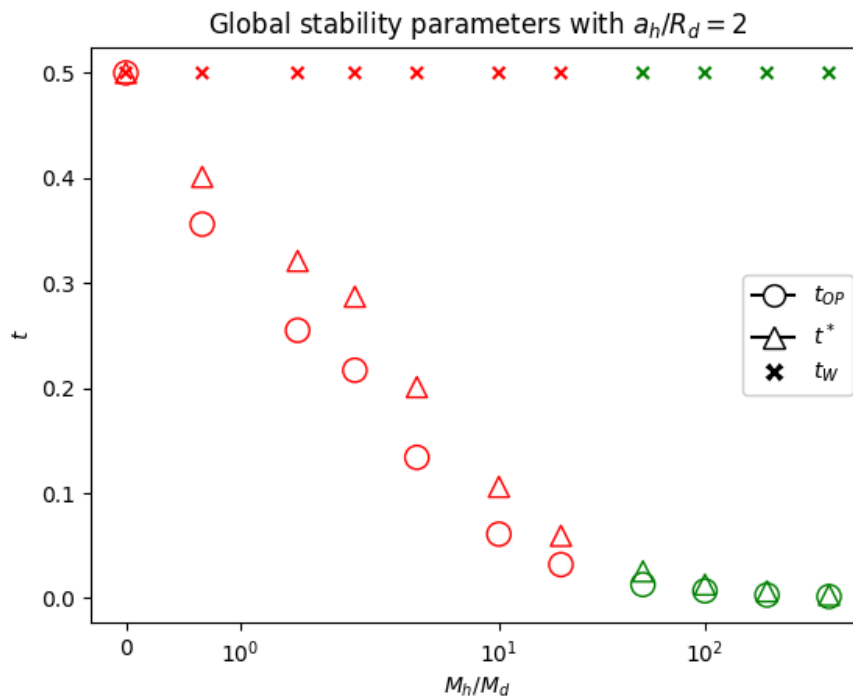


Figure 4.40: At  $t = 0$ ,  $t_{OP}$ ,  $t^*$  and  $t_W$  for all the simulations in Table 4.1 with  $a_h/R_d = 2$  and  $\alpha = 0$ . The colour green refers to stable discs, while the colour red to unstable discs.

During our simulation analysis, we have found that the stability of the disc depends not only on the halo-to-disc mass ratio  $M_h/M_d$ , but also on the halo-to-disc scale length ratio  $a_h/R_d$ . In fact, for  $a_h/R_d < 2$ , the disc is stable for  $M_h/M_d \geq 50$ , while for  $a_h/R_d = 5$  the stability is reached for  $M_h/M_d \geq 200$ .

From Figures 4.39 ( $a_h/R_d = 1$ ,  $\alpha = 0$ ), 4.40 ( $a_h/R_d = 2$ ,  $\alpha = 0$ ) and 4.41 ( $a_h/R_d = 5$ ,  $\alpha = 0$ ) we can find that, by definition,  $t_{OP} = t^* = t_W \equiv 0.5$  when there is no halo in the simulation (namely  $M_h/M_d = 0$ ; see Section 2.5). We can also see that we have found unstable systems even in simulations the Ostriker-Peebles criterion (based on  $t_{OP}$ ; Condition 2.11) states the system should be stable. We can say the same thing about the Efstathiou-Lake-Negroponte criterion (based on  $t^*$ ; Condition (2.23)). Nevertheless, the behaviour of both  $t_{OP}$  and  $t^*$  is described by curves that are monotonically decreasing as the halo-to-disc mass ratio increases and the halo-to-disc scale length is fixed. We can also state that the curves of  $t_{OP}$  and  $t^*$  tend to superpose when the halo-to-disc scale length ratio  $a_h/R_d$  is decreasing; we can see this difference by comparing Figures 4.39 and 4.41.

The behaviour of  $t_W$  in all simulation runs suggests it is insensitive to the choice of  $M_h/M_d$  and  $a_h/R_d$ , because its value is always  $t_W = 1/2$  (see Figure 4.44). Our explanation is related to both the construction of the parameter (Section 2.5), which is strictly connected to the virial theorem of the disc embedded in an external potential – the dark halo – and our initial conditions for the  $N$ -body runs. In fact, from the theoretical construction of  $t_W$  we already knew that  $0 \leq t_W \leq 1/2$  (Equation 2.32) and that, in case the disc has no random motions (namely  $\Pi_d = 0$ ), we always have  $t_W = 1/2$ . This is our case, because in the initial conditions described in Section 3.3 we set all the disc particles in motion on circular orbits such that they are in equilibrium

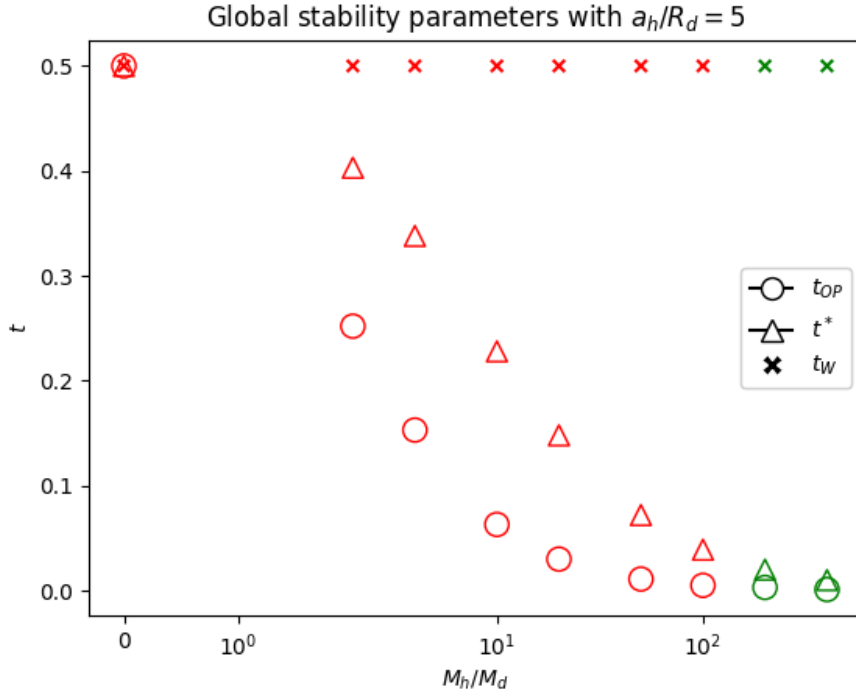


Figure 4.41: At  $t = 0$ ,  $t_{OP}$ ,  $t^*$  and  $t_W$  for all the simulations in Table 4.1 with  $a_h/R_d = 5$  and  $\alpha = 0$ . The colour green refers to stable discs, while the colour red to unstable discs.

with the total disc-halo potential. For this reason, in our simulations  $t_W$  has fixed value and is not sensitive to the change of the disc-halo configuration. In particular, if we introduce a fraction of retrograde orbits  $\alpha$ , we can explicit  $T$  as function of  $\alpha$  – see Appendix D, Equation D.20. In our specific case, this means that

$$t_W = \frac{1}{2}(1 - 2\alpha)^2 \quad (4.27)$$

for every choice of  $T$  and  $W_D$ . This result tells us that  $t_W$  is strictly dependent on  $\alpha$ , thus it appears insensitive to the other parameters  $T$  and  $W_D$  that described the whole system. Now, if we connect the construction of  $t_W$  with  $t^*$  (Equation 2.31), we can explain better why in  $t^*$  ELN82 introduced a  $(1 + f_{ext})^2$  factor, thus not following an accurate derivation from the virial theorem of the disc (Equation 2.13).

Another common point of  $t_{OP}$ ,  $t^*$  and  $t_W$  is that when we introduces a fraction  $\alpha = 1/2$  of retrograde orbits in our simulations, all the global stability parameters are forced to be always equal to 0 – see Figures 4.42, 4.43 and 4.44. The explanation is simple and is related to the construction of these parameters: since we use the ordered kinetic energy of the disc particles  $T$ , it vanishes when  $\alpha = 1/2$  because of the relation between  $T$  and  $\alpha$  (Equation D.20). For this reason, if  $T_d = 0$ , then  $t_{OP}$ ,  $t^*$  and  $t_W$  always vanish, no matter the disc is stable or not. This behaviour was expected analytically, but the null value is not a hint of stability: as we have seen in Sections 4.3 and 4.4, the presence of retrograde orbits (thus, of azimuthal velocity dispersion) gives little contribution to prevent local instabilities, but does not ensure the global stability of the disc.

We end with a few considerations regarding the different sensitivity of each of the



We can conclude that among our models we have found several counterexamples that, though idealized, violate both OP73 and ELN82 criteria.

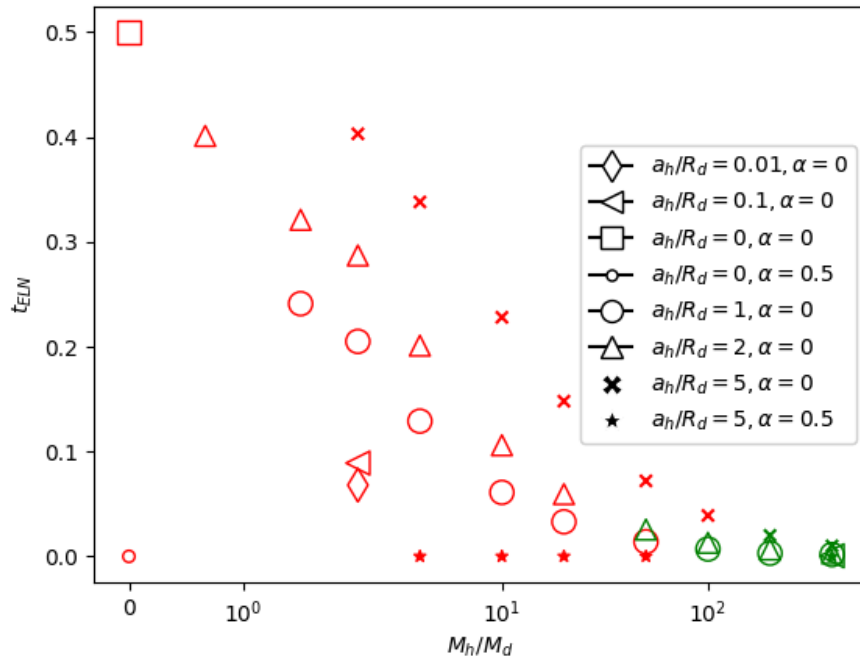


Figure 4.43: At  $t = 0$ ,  $t^*$  for all the simulations in Table 4.1. The colour green refers to stable discs, while the colour red to unstable discs.

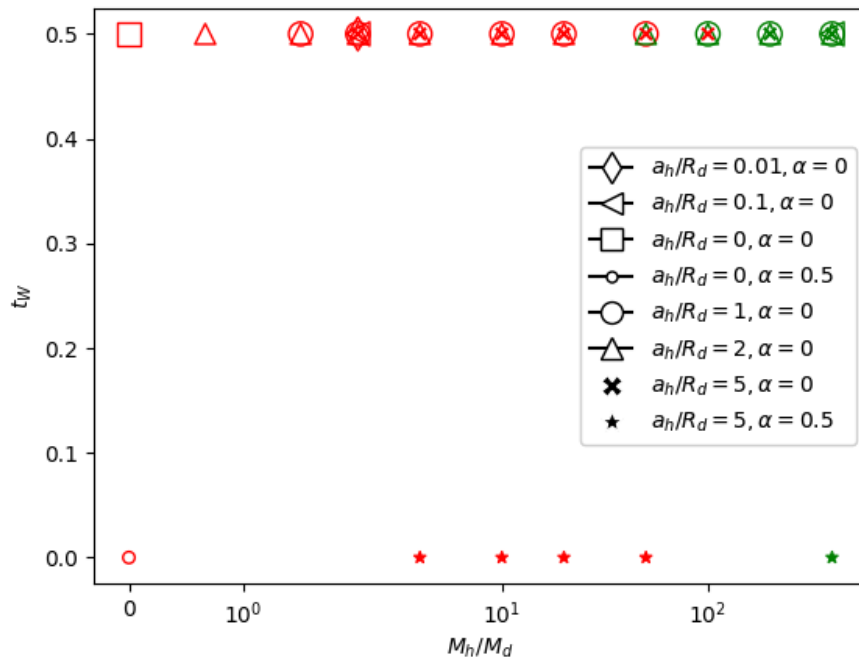


Figure 4.44: At  $t = 0$ ,  $t_W$  for all the simulations in Table 4.1. The colour green refers to stable discs, while the colour red to unstable discs.

# Chapter 5

## Conclusions and future perspectives

Together with a new parameter  $t_W$  (Section 2.5), in this thesis work we studied the behaviour of the OP73 ( $t_{OP}$ ) and ELN82 ( $t^*$ ) classical stability indicators through  $N$ -body simulations performed via the Fortran Version of a Fast Poisson Solver code (FVFPS, Londrillo et al., 2003), where we set a razor-thin exponential disc embedded in an external Hernquist (1990) halo, where the latter is treated as a fixed external potential. In Chapter 3 we set the initial conditions for our simulation suite such that every disc particle starts with a circular motion around the centre of the disc, with or without the presence of the halo. In Chapter 4 we reported the results of our simulation suite, which we summarize as follows:

- In case of disc-only simulations with no retrograde orbits ( $\alpha = 0$ ), starting from our initial conditions (Section 3.2.1), the system is always globally unstable and by construction  $t_{OP} = t^* = t_W = 1/2$ , thus the three parameters degenerate in only one, whose behaviour depends on the velocity distribution function of the particles. We note that the  $1/2$  value is due to the initial conditions of the system – all disc particles are moving in circular orbits in equilibrium with their own potential. In general, when we could have  $\Pi_d \neq 0$ , all the three parameters might have lower values than  $1/2$ , namely  $t_{OP} = t^* = t_W \leq 1/2$ . In disc-only simulations with  $\alpha = 1/2$ , although  $T_d = 0$  and thus  $t_{OP} = t^* = t_W = 0$ , the system is globally unstable; different from the  $M_h 0 a_h 0 \alpha 0$  case, the presence of the azimuthal velocity dispersion  $\sigma_\varphi^2$ , through the insertion of a fraction  $\alpha$  of retrograde orbits, gives a significant contribution to limit the disc disruption.
- In the disc-halo simulations with no retrograde orbits ( $\alpha = 0$ ), the presence of the halo removes the degeneration between  $t_{OP}$ ,  $t^*$  and  $t_W$ . The global stability of the disc now depends essentially on the halo-to-disc mass ratio  $M_h/M_d$  and scale length ratio  $a_h/R_d$ . From our simulation suite, we found that the discs are globally stable: for  $M_h/M_d \gtrsim 50$  if  $a_h/R_d \lesssim 2$ ; for  $M_h/M_d \gtrsim 200$  if  $a_h/R_d \simeq 5$ .
- $t_W = 1/2$  in all our simulations because of its definition (Equation 2.29) and our set-up for the initial conditions (Section 3.3). This result is actually expected: with the introduction of the retrograde orbits with  $\alpha$  in our simulation suite, the ordered and random kinetic energies has an explicit dependence with  $\alpha$  (see Appendix D). From Equation (D.20) and our initial conditions (Section 3.3), we have  $2T + |W_D| = 0$ , thus  $t_W \equiv T/|W_D| = (1 - 2\alpha)^2/2$ , and when  $\alpha = 0$  we always have  $t_W = 1/2$ . This could be the reason that led ELN82 to insert another  $1/(1 + f_{ext})$  factor in the  $t^*$  ratio.

- While  $t_W$  does not provide useful information for the construction of an alternative global stability criterion (at least for the idealized systems here considered),  $t_{OP}$  and  $t^*$  behave differently. In particular,  $t_{OP}$  seems to be more sensitive on the halo-to-disc mass ratio  $M_h/M_d$  and not to its scale length ratio  $a_h/R_d$ : if the former increases,  $t_{OP}$  lowers mainly because of the presence of  $W_h$  in  $W$  in the  $t_{OP}$  definition (Equation 2.7); if the latter has small values (namely,  $a_h/R_d = 0.1, 0.01$ ),  $t_{OP}$  appears to be very sensitive to this parameter choice and thus lowers significantly even though  $M_h/M_d \simeq 2$ , because the halo concentration reflects on the value of  $W_h$  (see Figure 4.42).
- Due to the absence of  $W_h$  in its definition,  $t^*$  is instead quite sensitive to the variation of both  $M_h/M_d$  and  $a_h/R_d$  (Figure 4.43), in particular when the  $a_h/R_d$  ratio increases with fixed  $M_h/M_d$ , but it is less sensitive in case of small but concentrated halos (e.g., simulations  $M_h2a_h0.1\alpha0$  and  $M_h2a_h0.01\alpha0$ ). Furthermore, concerning the global stability criteria related to  $t_{OP}$  and  $t^*$  (Equations 2.11 and 2.23), we note that several of our models are unstable even if they have  $t_{OP,crit}$  and  $t_{crit}^*$  lower than the critical values (Conditions 2.11 and 2.23).
- From our simulation runs, the global stability of a disc can be reached only if the dark matter halo is massive. If present, the azimuthal velocity dispersion  $\sigma_\varphi^2$ , obtained through the insertion of a fraction  $\alpha$  of retrograde orbits, gives a little contribution to prevent local instabilities, although they are still present. Given our initial conditions described in Section 3.3, when  $\alpha = 1/2$  we have  $T_d = 0$  and thus  $t_{OP} = t^* = t_W = 0$  independently of the disc-halo input parameters. Even though the three indicators have null value, it is not necessary a hint of stability: simulations  $M_h0a_h0\alpha0.5$  and  $M_h4a_h5\alpha0.5$  are two examples that support the last sentence. This result suggests that the explicit presence of random motions  $\Pi_d$  should be present in a new formulation of a global stability criterion.
- When a bar is forming at the centre of the disc, it is weak and dissolves after few dynamical times from its formation. We may explain this feature by considering our initial conditions for every  $N$ -body run, where radial motions are absent and  $\sigma_R = 0$ . However, it is well-known that random motions generally contribute to the disc stability and might prevent bar formation (see, e.g., Athanassoula and Sellwood, 1986; Sellwood, 2016).

Though the results of this work are limited, due to some simplifying assumptions in the simulation suite we performed, our conclusions could be the basis for future research on this topic. In particular, we did not adopt a 'live' halo capable of evolving during the simulation run, but we treated the halo as a fixed external potential, as OP73 and ELN82 do in their work (see also Kataria et al., 2020). In our case, we preferred to start with this simple scenario, also because the presence of a 'live' halo in a disc-halo system needs the introduction of proper distribution functions of the whole system, thus a deep study on this topic would be necessary. Furthermore, we could also adopt different (and more realistic) models for the disc, from other two-dimensional models (e.g., Kuzmin, 1956) to three-dimensional ones (e.g., Smith et al., 2015). We could also model the dark matter halo, especially when rigid, with a different spherical profile – (for instance, Navarro et al., 1997).

Taking the numerical implementation apart, the primary focus should always be on the construction of a new global stability criterion. As seen in Section 2.4, neither

$t_{OP}$  nor  $t^*$  are universally valid, so the search for a more efficient parameter for global stability of galactic discs is still open.

# Appendix A

## Mixed terms $W_{12}$ and $W_{21}$ in a two-component system

We can explicit the expressions of the interacting gravitational energies  $W_{12}$  and  $W_{21}$  using the definition of  $\Phi$  (Equation 1.2):

$$W_{12} = - \int d^3\mathbf{x} \rho_1(\mathbf{x}) \langle \mathbf{x}, \nabla \Phi_2(\mathbf{x}) \rangle = G \int d^3\mathbf{x} \int d^3\mathbf{x}' \rho_1(\mathbf{x}) \rho_2(\mathbf{x}') \left\langle \mathbf{x}, \frac{\mathbf{x}' - \mathbf{x}}{|\mathbf{x}' - \mathbf{x}|^3} \right\rangle; \quad (\text{A.1})$$

$$W_{21} = - \int d^3\mathbf{x} \rho_2(\mathbf{x}) \langle \mathbf{x}, \nabla \Phi_1(\mathbf{x}) \rangle = G \int d^3\mathbf{x} \int d^3\mathbf{x}' \rho_2(\mathbf{x}) \rho_1(\mathbf{x}') \left\langle \mathbf{x}, \frac{\mathbf{x}' - \mathbf{x}}{|\mathbf{x}' - \mathbf{x}|^3} \right\rangle. \quad (\text{A.2})$$

We can also rewrite Equations (A.1) and (A.2) by interchanging the dummy variables  $\mathbf{x}$  and  $\mathbf{x}'$ :

$$W_{12} = G \int d^3\mathbf{x}' \int d^3\mathbf{x} \rho_1(\mathbf{x}') \rho_2(\mathbf{x}) \left\langle \mathbf{x}', \frac{\mathbf{x} - \mathbf{x}'}{|\mathbf{x} - \mathbf{x}'|^3} \right\rangle; \quad (\text{A.3})$$

$$W_{21} = G \int d^3\mathbf{x}' \int d^3\mathbf{x} \rho_2(\mathbf{x}') \rho_1(\mathbf{x}) \left\langle \mathbf{x}', \frac{\mathbf{x} - \mathbf{x}'}{|\mathbf{x} - \mathbf{x}'|^3} \right\rangle. \quad (\text{A.4})$$

Now, summing Equation (A.1) with Equation (A.4) (or, similarly, Equation (A.2) with Equation (A.3)), we have

$$\begin{aligned} W_{12} + W_{21} &\equiv W_{1\leftrightarrow 2} = -G \int d^3\mathbf{x} \int d^3\mathbf{x}' \rho_1(\mathbf{x}) \rho_2(\mathbf{x}') \left\langle \mathbf{x}' - \mathbf{x}, \frac{\mathbf{x}' - \mathbf{x}}{|\mathbf{x}' - \mathbf{x}|^3} \right\rangle = \\ &= -G \int d^3\mathbf{x} \int d^3\mathbf{x}' \frac{\rho_1(\mathbf{x}) \rho_2(\mathbf{x}')}{|\mathbf{x}' - \mathbf{x}|}. \end{aligned} \quad (\text{A.5})$$

Recalling again the definition of  $\Phi$  (Equation 1.2), we can have two possible expressions of  $W_{1\leftrightarrow 2}$ :

$$W_{1\leftrightarrow 2} = \int d^3\mathbf{x} \rho_1(\mathbf{x}) \Phi_2(\mathbf{x}) = \int d^3\mathbf{x} \rho_2(\mathbf{x}) \Phi_1(\mathbf{x}). \quad (\text{A.6})$$

Equation (A.6) is also treated in Ciotti (2021) (Section 10.5.1), which adopts a different notation – see Ciotti (2021) and Section 1.2.5 for further details.

# Appendix B

## Details about OP73 and ELN82

### B.1 OP73

#### B.1.1 Acceleration computation

OP73 computed the acceleration of the  $i$ -th particle as

$$\mathbf{a}_i = -\frac{(1.1)^2 \mathbf{x}_i M_H}{R_{\max}(x_i + 0.1R_{\max})^2} + \sum_{j \neq i} \frac{(\mathbf{x}_j - \mathbf{x}_i)}{(x_{ij}^2 + c^2)^{3/2}}, \quad (\text{B.1})$$

where  $x_{ij} = |\mathbf{x}_i - \mathbf{x}_j|$  is the distance between the  $i$ -th and the  $j$ -th particle,  $R_{\max}$  is the disc (and halo) size,  $M_H$  is the halo mass,  $x_i = \|\mathbf{x}_i\|$  is the distance magnitude of the  $i$ -th particle from the centre of the reference system and  $c$  is the softening length. The first term of Equation (B.1) is the contribution by the spherically symmetric halo mass  $M_H$ . Equation (B.1) holds for  $R < R_{\max}$ . At  $R > R_{\max}$  the contribution of the halo is  $-\mathbf{x}_i M_H/x_i^3$ . The second term is an approximation of the Newtonian gravitational potential, which holds true when  $x_{ij} \gg c$ . Because of this approximation, the virial theorem was not exactly satisfied in OP73, but their numerical models show a departure of the order of 10 percent with respect to the virial theorem, with the consequence that the uncertainty of  $t$  is of the same order. In OP73, the gravitational constant  $G = 1$ . The softening  $c$  avoids divergent accelerations in the close encounters situation during the  $N$ -body simulation.

#### B.1.2 Initial conditions

The initial surface density distribution of the axisymmetric disc is  $\Sigma(R) \propto R^{-1}$ , so that the distribution of the points is uniform in the radius interval  $0 < R < R_{\max}$ . At the beginning of the simulations, all the disc particles lie on the disc plane and also have a velocity component that is perpendicular to the disc plane. The disc thickness is determined by this vertical velocity.

The first step is assigning the initial velocities in order to hold each particle in circular orbit. The initial velocity of each particle is directed in the plane perpendicular to the radial vector, with a magnitude of  $\langle -\mathbf{x}_i \cdot \mathbf{a}_i \rangle^{1/2}$ . Through  $N$ -body simulations, OP73 noted that the rotation curve of the disc is essentially unchanged when the halo with the same surface density distribution of the disc is added. In order to have a Toomre (1964) stability with Toomre parameter  $Q > 1$ , OP73 added a velocity dispersion to the disc particles, so to avoid the development of small-scale irregularities.

Assuming cylindrical coordinates  $(R, \varphi, z)$ , OP73 used random normal distributions with standard deviations  $\sigma_R$ ,  $\sigma_\varphi$  and  $\sigma_z$ . They chose a value of  $\sigma$  such that the Toomre parameter is  $Q \simeq 1.2$ . OP73 also obtained  $\sigma_\varphi$  from  $\sigma_R$  using the equilibrium expression required for steady epicyclic motions and put  $\sigma_z = \sigma_\varphi$ . Finally, OP73 modified the initial velocity  $v_i$  of each particle in order to have the same total kinetic energy of the former equilibrium state, before adding the velocity dispersion.

OP73's simulations have the following parameters in common: number of particles  $N \simeq 10^2$ ; disc radius  $R_{max}/R_s = 1$ ; softening  $c/R_s = 0.05$ ; time step  $\Delta t/\tau = 0.001$ , where  $R_s$  is a scale radius and  $\tau$  is the orbital period at the half-mass radius of the disc.

### B.1.3 Energies computation

OP73 numerically computed the ordered kinetic energy of the system  $T$  (Equation 2.2) by dividing the axisymmetric disc into rings:

$$T = \frac{1}{2} \sum_k n_k \langle v_k \rangle^2 \quad (\text{B.2})$$

where  $n_k$  and  $\langle v_k \rangle$  is the number density of stars and their mean velocity  $v_\phi$  within the  $k$ -th ring, respectively. To obtain  $\langle v_k \rangle$ , OP73 sum each velocity assuming  $v_\phi > 0$  for forward-moving particles and  $v_\phi < 0$  for backward-moving ones.

## B.2 ELN82

### B.2.1 Numerical computation

ELN82 performed two-dimensional simulations using a Fourier transform potential solver (Hohl and Hockney, 1969) and the cloud-in-cell (CIC) technique for the mass assignment and force interpolation. They also used a time-centred leap-frog scheme in order to advance the particle coordinates, which were  $N = 20000$  in all the simulations. The unresponsive halo component was included through the addition of a fixed axisymmetric force (ELN82), which changes the velocity of the disc particles. In all ELN82's simulations, the halo extends out to one half the active mesh length. They used from 150 to 500 time steps per rotation period  $\tau$ . (Note that  $\tau$  also depends on the potential of the external halo component.) ELN82's studies are insensitive to the specific choice of the time step, as also shown in (OP73).

### B.2.2 Galaxy models

#### Main model

After generating the initial density distribution (2.21), ELN82 assigned the velocity to the disc particles using a Gaussian distribution. Stellar hydrodynamics equations were solved to determine the angular velocity of the disc. The radial velocity dispersion was set to be the minimum value to stabilize all the local axisymmetric instabilities (from Toomre, 1964):

$$\sigma_r(r) = Q(R)\sigma_{\min}(R) \quad (\text{B.3})$$

$$\sigma_{\min}(R) = 3.36G\Sigma_d(R)/\kappa(R) \quad (\text{B.4})$$

where  $Q(R)$  is the Toomre parameter and  $\kappa(R)$  the epicyclic frequency at distance  $R$  from the disc centre. Observations of stellar motion in our Galaxy showed that the disc is cold ( $\sigma_R \ll v_{max}$ ) with  $Q \simeq 1$  (Toomre, 1964, 1974). For this reason, ELN82 modelled initially cold discs with a uniform constant value  $Q = 1.05$  or a position-dependent Toomre parameter  $Q(R) = 1 + \exp(-\alpha_d^2 R^2)$ .

All these assignment were performed using the analytic expressions for density, force and rotational velocity. Particles were divided amongst radial bins and the mean radial force  $\mathbf{F}_i$  in the  $i$ -th ring was calculated and compared to the expected radial force  $\mathbf{F}_i^G$ , which adopts  $1/r^2$  gravity. So the velocity of each particle within the  $i$ -th ring was multiplied by a factor  $(\|\mathbf{F}_i\|/\|\mathbf{F}_i^G\|)^{1/2}$ . ELN82 set up disc-halo models in the parameter ranges  $0.1 \leq \hat{R}_{max} \leq 1.3$  and  $0.7 \leq \hat{v}_{max} \leq 1.3$ . In all these models the exponential disc was truncated at  $R_{d,max} = 5/\alpha_d$ . ELN82 stated that the gravitational softening did not affect the results of their simulations.

### Other models

ELN82 added two other sets of models, which now used a fixed potential given by the mass distribution

$$\rho_{ext}(R) = \frac{\rho_h}{1 + \frac{R^2}{R_{h,max}^2}} \quad (\text{B.5})$$

together with an exponential disc with  $\alpha_d R_{h,max} = 0.2$  or a disc with a Hunter surface density (see Hohl, 1970)

$$\Sigma_d(R) = \frac{11}{2\pi R_{d,max}^2} M_d (1 - R^2/R_{d,max}^2)^{9/2} \quad (\text{B.6})$$

with  $R_{d,max}/R_{h,max} = 0.1$ .

### B.2.3 $m = 2$ modes, bar strength $\delta_2$ and bar length $l_b$

In order to determine the formation of bar-like modes, ELN82 divided the spatial domain in radial rings, each one contained about  $600 \div 1300$  particles. Then they computed the amplitude and phase of the  $m = 2$  modes and they computed the  $A_2/A_0$  ratio in each ring in order to measure the bar strength, where

$$A_m(t) = \left| \sum_{j=1}^N \mu_j e^{im\phi_j} \right|, \quad (\text{B.7})$$

and  $\mu_j$  is the mass of the  $j$ -th particle and  $\phi_j(t)$  is the cylindrical polar angle of the  $j$ -th particle at the time  $t$  (see, e.g., Sellwood, 2016).

In particular, ELN82 took the maximum value of Equation (B.7) in each ring as a measure of the bar strength, defining:

$$\delta_2 = \left( \frac{\rho_{m=2}}{\rho_{m=0}} \right)_{max} \quad (\text{B.8})$$

Since  $t^*$  and  $\delta_2$  show the stabilizing effect of a rigid halo component, but do not distinguish a bar from a spiral, ELN82 also defined a bar length  $l_b$  as the region over which the phases are coherent to  $\pm 10^\circ$ .

Some of ELN82's models included Kalnajs's (1972) distribution functions, whose system have been included in a rigid spherical halo.

## B.2.4 Results from other models

Models with surface density profile (B.6) and  $R_{d,\max}/R_{d,\max} = 0.1$  have a constant value of the  $m = 2$  amplitude during the evolution, giving no evidence of a dissolution of a bar.

ELN82's attempts to stabilize models with halo density profile (B.5) and  $\alpha_d R_{h,\max} = 0.2$  using high velocity dispersion at the centre were not successful; for this reason, ELN82 suggested to investigate in detail the initial conditions generated from a self-consistent solution to the collisionless Boltzmann equation, in order to examine this problem.

ELN82 found out that in models with halo density profile by Equation (B.5) with  $0.1 \leq \hat{R}_{max} \leq 1.3$  and  $0.7 \leq \hat{v}_{max} \leq 1.3$ ,  $t^*$  does not determine by itself the stability of the initial configuration to bar formation, because  $t^*$  depends on  $\hat{R}_{max}$ . However, ELN82 found that such models will be stable against the growth of large-scale bar-like modes if

$$\hat{v}_{max} \geq 1.1 \quad \text{for} \quad 0.1 \leq \hat{R}_{max} \leq 1.3 \quad \Rightarrow \quad t^* \leq 0.2 \quad (\text{B.9})$$

In one Kalnajs's model there is a development of a bar, but the final density profile differs from an exponential distribution.

## B.2.5 Comparison with observations

ELN82 made a comparison of their work with observations. The values of  $R_{max}$ ,  $v_{max}$  and  $\alpha_d^{-1}$  may be estimated from the observation of the rotation curve and photometry. The morphology of the galaxy may be used to set a constraint to the mass-to-light ratio of the cool disc component. ELN82 stated their numerical models may be applied on Sc and late type galaxies as they have rotation curves for which  $\hat{R}_{max}$  lies within the range where the criterion (2.23) has been tested in their work.

ELN82 found out that the stability criterion of cool discs in Sc galaxies is related to a low mass-to-light ratio:

$$\frac{M_d}{L_d} \leq 1.5h \quad (\text{B.10})$$

where  $h$  is the Hubble parameter normalized to  $100 \text{ km s}^{-1} \text{ Mpc}^{-1}$  and  $M_d/L_d$  is in units of  $(M/L)_\odot$ . In case of real disc galaxies, the HI mass has to be considered and the bar instability analysis has found to be difficult to understand in terms of global stability criteria discussed in ELN82's work.

# Appendix C

## Equations of motion in polar coordinates

### C.1 General motion

Assuming a point mass moving in a 2-dimensional plane, its Cartesian coordinates  $(x, y)$  can be expressed in terms of polar coordinates  $(R, \varphi)$ :

$$\begin{cases} x = R \cos \varphi \\ y = R \sin \varphi \end{cases} . \quad (\text{C.1})$$

From System (C.1) it is straightforward to obtain

$$\cos \varphi = \frac{x}{R}; \quad \sin \varphi = \frac{y}{R}. \quad (\text{C.2})$$

The time derivative of System (C.1) is:

$$\begin{cases} \dot{x} = v_x = \dot{R} \cos \varphi - R \dot{\varphi} \sin \varphi \\ \dot{y} = v_y = \dot{R} \sin \varphi + R \dot{\varphi} \cos \varphi \end{cases} , \quad (\text{C.3})$$

where  $\dot{r} = v_R$  is the radial velocity, while  $R\dot{\varphi} = v_\varphi$  is the tangential velocity. System (C.3) can be also expressed as

$$\begin{pmatrix} v_x \\ v_y \end{pmatrix} = \begin{pmatrix} \cos \varphi & -\sin \varphi \\ \sin \varphi & \cos \varphi \end{pmatrix} \begin{pmatrix} \dot{R} \\ R\dot{\varphi} \end{pmatrix} = \mathbf{R} \begin{pmatrix} v_R \\ v_\varphi \end{pmatrix}, \quad (\text{C.4})$$

where  $\mathbf{R}$  is the 2D rotation matrix.

The squared magnitude of the total velocity is

$$v^2 = v_x^2 + v_y^2 = \dot{R}^2 + R^2 \dot{\varphi}^2 = v_R^2 + v_\varphi^2. \quad (\text{C.5})$$

From Equation (C.4) (or System (C.3)) we can also obtain

$$\begin{cases} v_R = v_x \cos \varphi + v_y \sin \varphi \\ v_\varphi = -v_x \sin \varphi + v_y \cos \varphi, \end{cases} \quad (\text{C.6})$$

or, equivalently,

$$\begin{pmatrix} v_R \\ v_\varphi \end{pmatrix} = \begin{pmatrix} \cos \varphi & \sin \varphi \\ -\sin \varphi & \cos \varphi \end{pmatrix} \begin{pmatrix} v_x \\ v_y \end{pmatrix} = \mathbf{R}^{-1} \begin{pmatrix} v_x \\ v_y \end{pmatrix}. \quad (\text{C.7})$$

## C.2 Pure circular motion ( $v_R = 0$ , $v_\varphi \neq 0$ )

System (C.3) reduces to

$$\begin{cases} v_x = -R\omega \sin \varphi \\ v_y = R\omega \cos \varphi, \end{cases} \quad (\text{C.8})$$

where we define  $\dot{\varphi} = \omega$  as the angular velocity of the point mass. From Equation (C.5) the squared magnitude of the total velocity is now:

$$v^2 = v_x^2 + v_y^2 = (-v_\varphi \sin \varphi)^2 + (v_\varphi \cos \varphi)^2 = v_\varphi^2. \quad (\text{C.9})$$

Taking a step back to System (C.8), substituting  $\cos \varphi = x/R$  and  $\sin \varphi = y/R$  from System (C.1) gives:

$$\begin{cases} v_x = -\omega y \\ v_y = \omega x \end{cases}. \quad (\text{C.10})$$

Isolating  $\omega$  from System (C.10) gives a way to compute its magnitude:

$$\omega = -\frac{v_x}{y} = \frac{v_y}{x}. \quad (\text{C.11})$$

It follows that

$$\frac{v_x}{y} + \frac{v_y}{x} = 0. \quad (\text{C.12})$$

# Appendix D

## $T$ and $\Pi$ computation in presence of retrograde orbits

Suppose an axisymmetric system whose particles are moving in pure circular motion under its own potential on the  $(R, \varphi)$  plane, where  $R$  and  $\varphi$  are the polar coordinates. Then

$$\mathbf{v}_R(R, z) = 0 \quad (\text{D.1})$$

$$\text{and } \mathbf{v}_\varphi(R, z) = R \frac{\partial \Phi(R, z)}{\partial R} \hat{\mathbf{e}}_\varphi = v_c \hat{\mathbf{e}}_\varphi \quad (\text{D.2})$$

for every  $(R, z)$  pair, where  $v_c$  is the circular speed and  $\hat{\mathbf{e}}_\varphi$  is the unit vector in the azimuthal direction. The consequence is that every disc particle has an angular momentum  $\mathbf{J}$  directed along  $z$ :

$$|\mathbf{J}| = |\mathbf{J}_z| = J_z. \quad (\text{D.3})$$

Now, assume a fraction  $\alpha$  of particles which are moving in the opposite direction with respect to the other ones, with opposite angular momentum  $-\mathbf{J}_z$ . The distribution function (DF) of the disc can be split into two parts:

$$f_+ = f_+(J_z) \quad (\text{D.4})$$

$$\text{and } f_- = f_+(-J_z). \quad (\text{D.5})$$

The whole DF can be written as a combination of both  $f_+$  and  $f_-$ :

$$f(J_z) = (1 - \alpha)f_+ + \alpha f_-. \quad (\text{D.6})$$

If all the system particles are moving on circular orbits, then two possible expressions of both  $f_+$  and  $f_-$  as functions of the phase-space coordinates  $(\mathbf{v}, \mathbf{r})$  are:

$$f_+(\mathbf{v}, \mathbf{r}) = \delta(\mathbf{v}(\mathbf{r}) - \mathbf{v}_c(\mathbf{r}))\rho(\mathbf{r}) \quad (\text{D.7})$$

$$\text{and } f_-(\mathbf{v}, \mathbf{r}) = \delta(\mathbf{v}(\mathbf{r}) + \mathbf{v}_c(\mathbf{r}))\rho(\mathbf{r}), \quad (\text{D.8})$$

where  $\mathbf{v}_c = v_c \hat{\mathbf{e}}_\varphi$ ,  $\delta$  is the Dirac delta and  $\rho(\mathbf{r})$  is the local density. Hereafter we will omit in the expression of the dependence of  $\mathbf{v}$  and  $\mathbf{v}_c$  on  $\mathbf{r}$ , in order to lighten the notation.

Combining Equations (D.7) and (D.8), the DF becomes

$$f(\mathbf{v}, \mathbf{r}) = [(1 - \alpha)\delta(\mathbf{v} - \mathbf{v}_c) + \alpha\delta(\mathbf{v} + \mathbf{v}_c)]\rho(\mathbf{r}). \quad (\text{D.9})$$

We now insert Equation (D.9) in the kinetic energy components  $T$  and  $\Pi$ , which are, recalling their traces from Equations (1.29a) and (1.29b),

$$T = \frac{1}{2} \int \langle \mathbf{v}(\mathbf{r}) \rangle^2 f(\mathbf{v}, \mathbf{r}) d^3\mathbf{v} d^3\mathbf{r} \quad (\text{D.10})$$

$$\text{and } \Pi = \int (\mathbf{v} - \langle \mathbf{v}(\mathbf{r}) \rangle)^2 f(\mathbf{v}, \mathbf{r}) d^3\mathbf{v} d^3\mathbf{r}, \quad (\text{D.11})$$

where  $\langle \mathbf{v}(\mathbf{r}) \rangle$  is the streaming velocity of the particles (Equation 2.4) and we make explicit  $\rho(\mathbf{x}) = \int d^3\mathbf{v} f(\mathbf{x}, \mathbf{v})$ . If we compute  $\langle \mathbf{v}(\mathbf{r}) \rangle$  (see Equation 2.4) with the DF seen in Equation (D.9), we get

$$\langle \mathbf{v}(\mathbf{r}) \rangle = \frac{\int \mathbf{v} f(\mathbf{v}, \mathbf{r}) d^3\mathbf{v}}{\int f(\mathbf{v}, \mathbf{r}) d^3\mathbf{v}} = \frac{\int \mathbf{v} [(1 - \alpha)\delta(\mathbf{v} - \mathbf{v}_c) + \alpha\delta(\mathbf{v} + \mathbf{v}_c)] \rho(\mathbf{r}) d^3\mathbf{v}}{\int [(1 - \alpha)\delta(\mathbf{v} - \mathbf{v}_c) + \alpha\delta(\mathbf{v} + \mathbf{v}_c)] \rho(\mathbf{r}) d^3\mathbf{v}}. \quad (\text{D.12})$$

We recall two useful Dirac delta properties:

$$\int f(\mathbf{x}) \delta(\mathbf{x} - \mathbf{x}') d^3\mathbf{x} = f(\mathbf{x}') \quad (\text{D.13})$$

$$\text{and } \int \delta(\mathbf{x} - \mathbf{x}') d^3\mathbf{x} = 1, \quad (\text{D.14})$$

where the integration is over all the  $\mathbb{R}^3$  domain. We apply Equations (D.13) and (D.14) on Equation (D.12), we take out  $\rho(\mathbf{r})$  from the integrals and decompose the latter, obtaining:

$$\begin{aligned} \langle \mathbf{v}(\mathbf{r}) \rangle &= \frac{\rho(\mathbf{r}) [(1 - \alpha) \int \mathbf{v} \delta(\mathbf{v} - \mathbf{v}_c) d^3\mathbf{v} + \alpha \int \mathbf{v} \delta(\mathbf{v} + \mathbf{v}_c) d^3\mathbf{v}]}{\rho(\mathbf{r}) [(1 - \alpha) \int \delta(\mathbf{v} - \mathbf{v}_c) d^3\mathbf{v} + \alpha \int \delta(\mathbf{v} + \mathbf{v}_c) d^3\mathbf{v}]} = \\ &= \frac{(1 - \alpha)\mathbf{v}_c - \alpha\mathbf{v}_c}{(1 - \alpha) + \alpha} = \\ &= (1 - 2\alpha)\mathbf{v}_c(\mathbf{r}). \end{aligned} \quad (\text{D.15})$$

Remembering that the velocity dispersion is

$$\sigma_v^2 = (\mathbf{v} - \langle \mathbf{v} \rangle)^2 = \langle \mathbf{v}^2 \rangle - \langle \mathbf{v} \rangle^2, \quad (\text{D.16})$$

we can also apply Dirac delta properties (Equations D.13 and D.14) on the  $\langle \mathbf{v}^2 \rangle$  term, which becomes

$$\begin{aligned} \langle \mathbf{v}^2(\mathbf{r}) \rangle &= \frac{\int \mathbf{v}^2 f(\mathbf{v}, \mathbf{r}) d^3\mathbf{v}}{\int f(\mathbf{v}, \mathbf{r}) d^3\mathbf{v}} = (1 - \alpha)\mathbf{v}_c^2 + \alpha\mathbf{v}_c^2 = \\ &= \mathbf{v}_c^2(\mathbf{r}). \end{aligned} \quad (\text{D.17})$$

Now we combine Equations (D.15) and (D.17) into Equation (D.16), which gives

$$\sigma_v^2 = \mathbf{v}_c^2 - (1 - 2\alpha)^2 \mathbf{v}_c^2 = 4\alpha(1 - \alpha)\mathbf{v}_c^2(\mathbf{r}). \quad (\text{D.18})$$

Reminding that:

$$\int f(\mathbf{v}, \mathbf{r}) d^3\mathbf{v} = \rho(\mathbf{r}), \quad (\text{D.19})$$

we can simplify both  $T$  (Equations D.10) and  $\Pi$  (Equation D.11) as

$$T = (1 - 2\alpha)^2 \frac{1}{2} \int \mathbf{v}_c^2(\mathbf{r}) \rho(\mathbf{r}) d^3\mathbf{r} = (1 - 2\alpha)^2 K \quad (\text{D.20})$$

$$\text{and } \Pi = 4\alpha(1 - \alpha) \int \mathbf{v}_c^2(\mathbf{r}) \rho(\mathbf{r}) d^3\mathbf{r} = 8\alpha(1 - \alpha)K, \quad (\text{D.21})$$

where

$$K = \frac{1}{2} \int \mathbf{v}_c^2(\mathbf{r}) \rho(\mathbf{r}) d^3\mathbf{r} \quad (\text{D.22})$$

is the total kinetic energy  $K$  and has this form because each particle moves in a circular orbit.

From Equations (D.20) and (D.21), it is straightforward to verify that for every  $\alpha$  the following condition holds:

$$T + \frac{1}{2}\Pi = K. \quad (\text{D.23})$$

# Bibliography

- Aarseth, S. J. (2003). *Gravitational N-Body Simulations*.
- Athanassoula, E. (2008). Disc instabilities and semi-analytic modelling of galaxy formation. *Monthly Notices of the Royal Astronomical Society*, 390(1):L69–L72.
- Athanassoula, E., Lambert, J. C., and Dehnen, W. (2005). Can bars be destroyed by a central mass concentration?– I. Simulations. *Monthly Notices of the Royal Astronomical Society*, 363(2):496–508.
- Athanassoula, E. and Sellwood, J. A. (1986). Bi-symmetric instabilities of the Kuzmin/Toomre disc. *Monthly Notices of the Royal Astronomical Society*, 221:213–232.
- Barazza, F. D., Jogee, S., and Marinova, I. (2008). Bars in Disk-dominated and Bulge-dominated Galaxies at  $z \sim 0$ : New Insights from  $\sim 3600$  SDSS Galaxies. *The Astrophysical Journal*, 675(2):1194–1212.
- Barnes, J. and Hut, P. (1986). A hierarchical  $O(N \log N)$  force-calculation algorithm. *Nature*, 324(6096):446–449.
- Berman, R. H. and Mark, J. W. K. (1979). Are massive galactic haloes necessary to prevent rapid, global bar formation? *Astronomy and Astrophysics*, 77(1-2):31–36.
- Binney, J. and Tremaine, S. (2008). *Galactic Dynamics: Second Edition*. Cambridge University Press, Cambridge.
- Bland-Hawthorn, J., Tepper-Garcia, T., Agertz, O., and Freeman, K. (2023). The Rapid Onset of Stellar Bars in the Baryon-dominated Centers of Disk Galaxies. *The Astrophysical Journal*, 947(2):80.
- Bodenheimer, Peter, L. G. P. R. M. Y. H. W. (2007). *Numerical Methods in Astrophysics: An Introduction*.
- Bodenheimer, P. and Ostriker, J. P. (1973). Rapidly Rotating Stars. VIII. Zero-Viscosity Polytropic Sequences. *The Astrophysical Journal*, 180:159–170.
- Bovy, J. (2023). *Dynamics and Astrophysics of Galaxies*. Princeton University Press. in prep.
- Christodoulou, D. M., Shlosman, I., and Tohline, J. E. (1995). A New Criterion for Bar-forming Instability in Rapidly Rotating Gaseous and Stellar Systems. I. Axisymmetric Form. *The Astrophysical Journal*, 443:551.

- Cimatti, A., Fraternali, F., and Nipoti, C. (2019). *Introduction to Galaxy Formation and Evolution: From Primordial Gas to Present-Day Galaxies*. Cambridge University Press.
- Ciotti, L. (2021). *Introduction to Stellar Dynamics*. Cambridge University Press.
- Collier, A., Shlosman, I., and Heller, C. (2019). Dark matter bars in spinning haloes. *Monthly Notices of the Royal Astronomical Society*, 488(4):5788–5801.
- de Vaucouleurs, G. (1959). General Physical Properties of External Galaxies. *Handbuch der Physik*, 53:311.
- Dehnen, W. (1993). A Family of Potential-Density Pairs for Spherical Galaxies and Bulges. *Monthly Notices of the Royal Astronomical Society*, 265:250.
- Dehnen, W. (2002). A Hierarchical O(N) Force Calculation Algorithm. *Journal of Computational Physics*, 179(1):27–42.
- Efstathiou, G., Lake, G., and Negroponte, J. (1982). The stability and masses of disc galaxies. *Monthly Notices of the Royal Astronomical Society*, 199:1069–1088.
- Eskridge, P. B., Frogel, J. A., Pogge, R. W., Quillen, A. C., Davies, R. L., DePoy, D. L., Houdashelt, M. L., Kuchinski, L. E., Ramírez, S. V., Sellgren, K., Terndrup, D. M., and Tiede, G. P. (2000). The Frequency of Barred Spiral Galaxies in the Near-Infrared. *Astronomical Journal*, 119(2):536–544.
- Evans, N. W. and Read, J. C. A. (1998). Stability of power-law discs - II. The global spiral modes. *Monthly Notices of the Royal Astronomical Society*, 300(1):106–130.
- Fall, S. M. and Efstathiou, G. (1980). Formation and rotation of disc galaxies with haloes. *Monthly Notices of the Royal Astronomical Society*, 193:189–206.
- Freeman, K. C. (1970). On the Disks of Spiral and S0 Galaxies. *The Astrophysical Journal*, 160:811.
- Ghosh, S., Fragkoudi, F., Di Matteo, P., and Saha, K. (2023). Bars and boxy/peanut bulges in thin and thick discs III. Boxy/peanut bulge formation and evolution in presence of thick discs. *arXiv e-prints*, page arXiv:2308.16239.
- Grosbøl, P., Patsis, P. A., and Pompei, E. (2004). Spiral galaxies observed in the near-infrared K band. I. Data analysis and structural parameters. *Astronomy and Astrophysics*, 423:849–859.
- Hernquist, L. (1990). An Analytical Model for Spherical Galaxies and Bulges. *The Astrophysical Journal*, 356:359.
- Hockney, R. W. and Eastwood, J. W. (1988). *Computer simulation using particles*.
- Hoffman, J. and Frankel, S. (2018). *Numerical Methods for Engineers and Scientists*. CRC Press.
- Hohl, F. (1970). Dynamical evolution of disk galaxies. *NASA Special Publication*, 343(343).

- Hohl, F. (1971). Numerical Experiments with a Disk of Stars. *The Astrophysical Journal*, 168:343.
- Hohl, F. (1976). Suppression of bar instability by a massive halo. *Astronomical Journal*, 81:30–36.
- Hohl, F. and Hockney, R. W. (1969). A Computer Model of Disks of Stars. *Journal of Computational Physics*, 4:306.
- Hunter, C. (1977). On Secular Stability, Secular Instability, and Points of Bifurcation of Rotating Gaseous Masses. *The Astrophysical Journal*, 213:497–517.
- Izquierdo-Villalba, D., Bonoli, S., Rosas-Guevara, Y., Springel, V., White, S. D. M., Zana, T., Dotti, M., Spinoso, D., Bonetti, M., and Lupi, A. (2022). Disc instability and bar formation: view from the IllustrisTNG simulations. *Monthly Notices of the Royal Astronomical Society*, 514(1):1006–1020.
- Jeans, J. H. (1902). The Stability of a Spherical Nebula. *Philosophical Transactions of the Royal Society of London Series A*, 199:1–53.
- Kalnajs, A. J. (1972). The Equilibria and Oscillations of a Family of Uniformly Rotating Stellar Disks. *The Astrophysical Journal*, 175:63.
- Kalnajs, A. J. (1977). Dynamics of flat galaxies. IV. The integral equation for normal modes in matrix form. *The Astrophysical Journal*, 212:637–644.
- Kataria, S. K., Das, M., and Barway, S. (2020). Testing a theoretical prediction for bar formation in galaxies with bulges. *Astronomy and Astrophysics*, 640:A14.
- Kuzmin, G. (1956). Model of the steady galaxy allowing of the triaxial distribution of velocities. *Astronomicheskii Zhurnal*, 33:27.
- Lebovitz, N. R. (1961). The Virial Tensor and its Application to Self-Gravitating Fluids. *The Astrophysical Journal*, 134:500.
- Londrillo, P., Nipoti, C., and Ciotti, L. (2003). A parallel implementation of a new fast algorithm for N-body simulations. *Memorie della Società Astronomica Italiana Supplementi*, 1:18.
- Menéndez-Delmestre, K., Sheth, K., Schinnerer, E., Jarrett, T. H., and Scoville, N. Z. (2007). A Near-Infrared Study of 2MASS Bars in Local Galaxies: An Anchor for High-Redshift Studies. *The Astrophysical Journal*, 657(2):790–804.
- Miller, R. H. (1971). Numerical Experiments in Collisionless Systems (Papers appear in the Proceedings of IAU Colloquium No. 10 Gravitational N-Body Problem (ed. by Myron Lecar), R. Reidel Publ. Co., Dordrecht-Holland.). *Astrophysics and Space Science*, 14(1):73–90.
- Miller, R. H. (1978). Numerical experiments on the stability of disklike galaxies. *The Astrophysical Journal*, 223:811–823.
- Miller, R. H., Prendergast, K. H., and Quirk, W. J. (1970). Numerical Experiments on Spiral Structure. *The Astrophysical Journal*, 161:903.

- Mo, H. J., Mao, S., and White, S. D. M. (1998). The formation of galactic discs. *Monthly Notices of the Royal Astronomical Society*, 295(2):319–336.
- Navarro, J. F., Frenk, C. S., and White, S. D. M. (1997). A Universal Density Profile from Hierarchical Clustering. *The Astrophysical Journal*, 490(2):493–508.
- Ostriker, J. P. and Peebles, P. J. E. (1973). A Numerical Study of the Stability of Flattened Galaxies: or, can Cold Galaxies Survive? *The Astrophysical Journal*, 186:467–480.
- Parente, M., Ragone-Figueroa, C., Granato, G. L., and Lapi, A. (2023). The  $z \lesssim 1$  drop of cosmic dust abundance in a semi-analytic framework. *Monthly Notices of the Royal Astronomical Society*, 521(4):6105–6123.
- Pawlowski, M. S., Kroupa, P., and de Boer, K. S. (2011). Making counter-orbiting tidal debris. The origin of the Milky Way disc of satellites? *Astronomy and Astrophysics*, 532:A118.
- Romeo, A. B., Agertz, O., and Renaud, F. (2023). The specific angular momentum of disc galaxies and its connection with galaxy morphology, bar structure, and disc gravitational instability. *Monthly Notices of the Royal Astronomical Society*, 518(1):1002–1021.
- Rosas-Guevara, Y., Bonoli, S., Dotti, M., Izquierdo-Villalba, D., Lupi, A., Zana, T., Bonetti, M., Nelson, D., Springel, V., Hernquist, L., and Vogelsberger, M. (2022). The evolution of the barred galaxy population in the TNG50 simulation. *Monthly Notices of the Royal Astronomical Society*, 512(4):5339–5357.
- Rosas-Guevara, Y., Bonoli, S., Dotti, M., Zana, T., Nelson, D., Pillepich, A., Ho, L. C., Izquierdo-Villalba, D., Hernquist, L., and Pakmor, R. (2020). The buildup of strongly barred galaxies in the TNG100 simulation. *Monthly Notices of the Royal Astronomical Society*, 491(2):2547–2564.
- Saha, K. and Elmegreen, B. (2018). Why Are Some Galaxies Not Barred? *The Astrophysical Journal*, 858(1):24.
- Sellwood, J. A. (1989). Meta-stability in galactic discs. *Monthly Notices of the Royal Astronomical Society*, 238:115–131.
- Sellwood, J. A. (2016). Bar Instability in Disk-Halo Systems. *The Astrophysical Journal*, 819(2):92.
- Sellwood, J. A. and Moore, E. M. (1999). On the Formation of Disk Galaxies and Massive Central Objects. *The Astrophysical Journal*, 510(1):125–135.
- Smith, R., Flynn, C., Candlish, G. N., Fellhauer, M., and Gibson, B. K. (2015). Simple and accurate modelling of the gravitational potential produced by thick and thin exponential discs. *Monthly Notices of the Royal Astronomical Society*, 448(3):2934–2940.
- Springel, V. (2005). The cosmological simulation code GADGET-2. *Monthly Notices of the Royal Astronomical Society*, 364(4):1105–1134.

- Toomre, A. (1964). On the gravitational stability of a disk of stars. *The Astrophysical Journal*, 139:1217–1238.
- Toomre, A. (1974). How Can It All Be Stable? *Highlights of Astronomy*, 3:457–464.
- Toomre, A. (1981). What amplifies the spirals. In Fall, S. M. and Lynden-Bell, D., editors, *Structure and Evolution of Normal Galaxies*, pages 111–136.
- Tremaine, S., Richstone, D. O., Byun, Y.-I., Dressler, A., Faber, S. M., Grillmair, C., Kormendy, J., and Lauer, T. R. (1994). A Family of Models for Spherical Stellar Systems. *Astronomical Journal*, 107:634.
- van de Ven, G., Mandelbaum, R., and Keeton, C. R. (2009). Galaxy density profiles and shapes - I. Simulation pipeline for lensing by realistic galaxy models. *Monthly Notices of the Royal Astronomical Society*, 398(2):607–634.
- Zang, T. A. (1976). *The Stability of a Model Galaxy*. PhD thesis.
- Zang, T. A. and Hohl, F. (1978). Computer experiments on the effect of retrograde stars in disk galaxies. *The Astrophysical Journal*, 226:521–539.